# Innovation in Brine Management: State-of-the-Art Insights on Challenges, their Mitigation, and Outlooks Toward the Future

By

Thomas Andrew Horseman

Dissertation

Submitted to the Faculty of the

Graduate School of Vanderbilt University

in partial fulfillment of the requirements

for the degree of

DOCTOR OF PHILOSOPHY

in

Chemical Engineering

May 31st, 2022

Nashville, Tennessee

Approved:

Shihong Lin, Ph.D.

Kane Jennings, Ph.D.

Paul Laibinis, Ph.D.

Alan Bowers, Ph.D.

*For my sister, Bailey, and my father, Tom,*

*who have supported and kept me motivated me on this journey*

# ACKNOWLEDGEMENTS

I would like to express my gratitude for my advisor, Dr. Shihong Lin, who has been an excellent mentor the past five years. He taught me what it means to develop fundamental understanding of the real world, and furthermore, how to convey that in a way that allows the field to progress. I would also like to thank my committee Dr. Kane Jennings, Dr. Paul Laibinis, and Dr. Alan Bowers, as well as my other mentor, Dr. Tiezheng Tong, for their support and advice.

I have worked with numerous colleagues within Dr. Lin's Group: Dr. Yu-Xi Huang, Dr. Zhangxin Wang, Dr. Li Wang, Dr. Yuanzhe Liang, Dr. Kofi Christie, Dr. Chunlei Su, Fei Gao, Yujiao Li, Dr. Huixia Lu, and Dr. Fei Shen; and outside of Dr. Lin's group: Yiming Yin, Yongjie Liu, and Zhigao Zhu. To each of these individuals, I thank you for everything I have learned from you and hope we can continue to collaborate in the future. To Rossane Delapp, Deela McGill, Lesa Brown, Rich Teising, Dalesha Blackwell, and current and past ViNSE staff, thanks for all your help with experiments, data collection, and laboratory techniques.

To the current students, Ruoyu Wang, Rui Chen, Joshua Livingston, Weifan Liu, Siyuan Feng, Xudong Zhang, Sizhuo Zhang, Sk Md Ali Zaker Shawon, Abigail Cafferty, and Juhyeon Roh, I wish you the best of the luck and am excited to cross paths in the future. To the undergraduate and high school students I have mentored: Nicholas Lowe, Molly Friedman, Adrian Florea, David Ware, and Syndey Juda, best of luck in your careers, I know you will do great things.

To my friends from home, the COG, from my undergraduate institution, Rose-Hulman, and to the friends I was fortunate to meet while at Vanderbilt, thank you all for your support through the good times and the bad. You all gave me an outlet outside of the lab to have fun and blow off steam. I can't thank you all enough.

Finally, I want to express my deepest gratitude to my family. My mother, Shirley, my grandmother, Ruth, and my great aunt, Leota, have continuously motivated me in my journey. To my loving girlfriend, Kaylee, thank you for your love and support during this time. Last but not least, to my little sister, Bailey, and my father, Tom, thank you all for always being there for me and pushing me to be the best that I can be. I love you all and would not have made it this far without you.

## TABLE OF CONTENTS

LIST OF FIGURES

LIST OF TABLES

NOMENCLATURE

| Abbreviations | Description |
|---|---|
| ZLD | Zero liquid discharge |
| TDS | Total dissolved solids |
| RO | Reverse osmosis |
| MSF | Multi-stage flash |
| MED | Multi-effect distillation |
| MVC | Mechanical Vapor Compression |
| MD | Membrane Distillation |
| ED | Electrodialysis |
| AFM | Atomic Force Spectroscopy |
| EDC | Electrodialytic-Crystallizer |
| QCM | Quartz Crystal Microbalance |
| QCM-D | Quartz Crystal Microbalance with Dissipation Monitoring |
| SEM | Scanning Electron Microscope |
| SEM-EDX | Scanning Electron Microscope with Energy Dispersive X-ray Detector |
| DI | Deionized |
| FAS | Fluoroalkylsilane |
| CA | Contact Angle |
| SA | Sliding Angle |
| RMS | Root-Mean-Square |
| NOMs | Natural Organic Matters |
| NF | Nanofiltration |
| PEG | Polyethyleneglycol |
| C-PS | Carboxylated Polystyrene |
| PE | Polyethylene |
| EDL | Electric Double Layer |
| SiNPs | Silica Nanoparticles |
| vdW | Van der Waals |
| PVDF | Polyvinylidene Fluoride |
| APTES | (3-Aminopropyl)triethoxysilane |
| TSS | Total Suspended Solids |
| MF | Microfiltration |

**Symbols**

| | |
|---|---|
| $\Delta f_n$ | Change in resonant frequency of the quartz crystal oscillator upon adsorption of mass (in $Hz$) |
| $n$ | Overtone order relative to the first harmonic resonant frequency (dimensionless) |
| $C$ | Mass sensitivity constant (-17.7 ng $Hz^{-1}$ $cm^{-2}$ for the 5 MHz crystals used in this work) |
| $\Delta m$ | Areal mass density (in $ng\ cm^{-2}$) |
| $\Delta D_n$ | Change in energy dissipation (dimensionless) |
| $\rho_l$ | Bulk liquid density |
| $\eta_l$ | Bulk liquid viscosity |
| $\omega_F$ | Angular fundamental resonance frequency |
| $\theta_A$ | Apparent contact angle |
| $f$ | Fraction of contact between the solid surface and the liquid |
| $\theta_0$ | Intrinsic contact angle (i.e., the contact angle on a molecularly smooth surface made of the same material as the rough surface that yields $\theta_A$) |
| $R_a$ | Average roughness |
| $R_q$ | Root mean square roughness |
| $r$ | Roughness ratio of the surface, defined as the ratio of actual surface area over the projected surface area |
| $W_{PS}$ | Net adhesion energy between the probe and substrate |
| $\gamma_{ij}$ | Interfacial energies between media $i$ and $j$ |
| $A_{PS}$ | Contact-area between the probe and substrate |
| $F_{Max}$ | Max adhesion force |
| $D_{Rupture}$ | Rupture distances |
| $V_{mem}$ | Ideal membrane voltage drop |
| $J_s$ | Salt flux in electrodialysis (in $\frac{mol}{m^2 s}$) |
| $J_w$ | Water flux in electrodialysis (in $\frac{mol}{m^2 s}$) |
| $n_h^{-1}$ | Salt hydration number |

**Subscripts**

| | |
|---|---|
| $P$ | probe |
| $S$ | substrate |
| $L$ | water |
| C-PS | carboxylated polystyrene colloidal probe |
| PE | polyethylene colloidal probe |

# CHAPTER 1: INTRODUCTION

## 1.1. Brine Management and the Urgent Need for a More Practical Solution

Currently, over 2 billion people globally lack access to drinking water [1], and conflict over water access has resulted in stricter environmental regulations on industrial water use [2]. In the most severe cases, regulators have even called for cease of operations in industries like agriculture to conserve water [3]. Considering global population is expected to increase by over 20%, and industrialization is expected to follow in its footsteps, we need to adopt more efficient water management strategies to proceed sustainably into the future [4]. While current water treatment technologies can recover around 50% of freshwater from incoming wastewater streams, that final 50% of wastewater, often referred to as brine, is typically wasted when it could otherwise be reused. Recovering 100% of freshwater from these wastewater streams, a process called zero-liquid discharge (ZLD), will soon be the norm.

ZLD offers several solutions to the emerging water scarcity issue. For example, 100% recovery of freshwater eliminates the need to supplement freshwater supply from increasingly scarce freshwater sources. Likewise, eliminating wastewater disposal protects the environment and reduces risk for hefty environmental fines and/or wastewater disposal costs. Complete separation of freshwater from solid waste also offers potential for resource recovery and generation of a secondary revenue streams [5–8]. However, ZLD and more generally, brine management, are technically challenging due to the high level of salinity, or total dissolved salts (TDS), present in wastewater stream. While the state-of-the-art, reverse osmosis (RO), is approaching the theoretical minimum in terms of energy efficiency, it is practically limited to a maximum level of TDS due to the dependence on osmotic pressure in the driving force for desalination [9]. As such, downstream brine concentration and crystallization methods in ZLD treatment trains are limited to evaporative techniques.

Evaporative brine management techniques are inherently energy intensive. Because the latent heat of water is relatively high (> 650 kWh $m^{-3}$), evaporative processes consume five to ten times more energy than the theoretical minimum energy required to concentrate and crystallize brine (typically < 10 kWh $m^{-3}$). While state-of-the-art evaporative brine management techniques such as multi-stage flash (MSF), multi-effect distillation (MED), and mechanical vapor compression (MVC) employ latent heat recovery to reduce energy consumption down to 30-60 kWh $m^{-3}$ [5,10],

there is still room for improvement with respect to energy consumption in brine management. Furthermore, these state-of-the-art evaporative brine management techniques are extremely capitally expensive, difficult to operate and maintain, and lack the modularity and scalability to operate in small-to-mid-scale ZLD treatment trains [11].

Promising solutions that may extend the practical applicability of ZLD would utilize readily available, low-cost energy sources, such as low-grade heat from the sun or waste heat from an industrial process, rather than high-grade steam generated via electricity. Alternatively, emerging brine management technologies that could avoid an evaporative separation altogether would theoretically reduce energy consumption and promote the applicability of ZLD in industry. Likewise, a more modular and scalable brine management process would extend the practicality of ZLD for any water treatment capacity in remote regions where water is scarce, but freshwater demand is relatively low.

### 1.2. Membrane Distillation

Membrane distillation (MD) is a membrane-based thermal desalination process that has received extensive and growing research and development interests in the past few decades. While MD has multiple configurations, each case involves the use of a nonwetted (typically hydrophobic), microporous membrane to serve as an airgap that separates the feed and distillate solutions from mixing. The transport of water vapor from the hot, salty feed solution to the cold distillate is driven by a partial vapor pressure gradient. This partial pressure gradient is typically induced by the temperature gradient and, in certain cases, enhanced by a partial vacuum [12–14].

The interest in MD has grown substantially in recent years due to the increasing demand for modular systems capable of treating hypersaline water and ZLD [5,15–17]. MD is the most promising modular (down-scalable) technology capable of treating high salinity feedwater using low-grade thermal energy and, thus, has several unique advantages for treating hypersaline brine, as compared to the state-the-of-art desalination process, reverse osmosis [12,18,19], or conventional thermal distillation processes [12,20–23].

In both MD, the microporous membranes serve as not only a medium for vapor transport but also a barrier to direct liquid permeation and, thus, must be maintained free from pore blocking and wetting. However, the feedwater in many promising applications of MD often contains constituents that promote fouling and wetting of conventional hydrophobic membranes. For

example, organic matter, such as proteins from the food and beverage industry or oil particles that exist in oil- and gas-produced water, are potent foulants, especially for hydrophobic membranes [15,24]. For MD used in treating hypersaline brine, an additional challenge is mineral scaling, that is, the formation and/or accumulation of salt precipitates on the membrane surface that results in significant flux reduction and, in some cases, even pore wetting [25–27].

These technical challenges, namely, scaling and fouling, constrain the practical adoption of MD. In particular, these limitations pose a paradox for MD as an effective technology for desalinating and concentrating hypersaline brines: on the one hand, MD is very promising for such applications due to its (theoretical) capability of handling hypersaline brine using low-grade thermal energy; on the other hand, concentrating brine inevitably increases the concentrations of salts and foulants - whatever constituents that originally exist in the feedwater - and thus intensifies the propensity of scaling and fouling and limits the (practical) applicability of MD for ZLD [12,19,28–30]. It is therefore of paramount importance for the community to gain fundamental understanding of these challenges facing MD to develop effective brine management and ZLD solutions.

### 1.3. Electrodialysis

Electrodialysis (ED) is a well-established membrane-based desalination technique that has been used to treat a wide range of wastewaters via electrical potential driving force [31]. In ED, a series of anion and cation exchange membranes are arranged in an alternating pattern and sandwiched between an anode and a cathode [32]. Typically, a saline feed stream flows into the ED cell and is split into several channels flowing between the alternating ion exchange membranes. Once an electrical potential is applied between the anode and cathode, cations transport through the cation exchange membrane toward the cathode, and anions transport through the anode along the electrical potential gradient [32]. Due to the alternating configuration of the ion exchange membranes, one compartment will be diluted as the cations pass through the cation exchange membrane toward the cathode and anions pass through the anion exchange membrane toward the anode. However, in the adjacent compartments, cations are retained because they cannot pass through the anion exchange membrane, and anions are retained as they cannot pass through the cation exchange membrane [32]. Subsequently, typical ED operation splits an incoming feed stream into two streams, a diluate and concentrated brine stream.

Traditionally, ED has been most widely used to convert brackish water into drinking water [33,34]. However, treating high salinity water with ED has gained recent interest due to EDs inherent advantages over other desalination processes. For example, ED is less prone to fouling and thus requires less pretreatment to maintain robust operation [35]. While ion exchange membranes represent the highest capital cost associated with ED, their fouling resistance and wide-range of chemical compatibility prolongs their lifetime and reduces replacement and maintenance costs relative to other membrane-based technologies [36]. Likewise, the capital cost for ED has been shown to be lower than the state of the art evaporative technology, MVC [5,10]. When concentrating high salinity brine, ED consumes only 7-15 kWh $m^{-3}$ while the state-of-the-art evaporation technology, MVC, consumes around 20-40 kWh $m^{-3}$ [5,10]. While ED has been used for making table salts and has been investigated as a unit process in a ZLD treatment train for further concentrating RO brine before MVC-based concentration and crystallization [37–44], ED alone has not been used as the final step in a ZLD process to concentrate and crystalize a high salinity brine. Herein, we discuss a novel application of ED to completely replace evaporative brine concentration and crystallization steps in ZLD treatment trains.

### 1.4. Objectives and Hypotheses

The overall objective of this dissertation is to elucidate failure mechanisms and evaluate the performance of novel brine management and ZLD technologies. With respect to MD, the main objective is to elucidate fouling mechanisms as to develop novel and effective fouling mitigation strategies. In the context of ED, the main objective is to develop and evaluate the practical applicability of ED in a novel application for ZLD and mineral crystal recovery.

The first objective is to demonstrate the influence of surface wetting properties and the interfacial gas layer charging on scaling kinetics. We produce interfacial gas bubbles on surfaces with hydrophilic, hydrophobic, and superhydrophobic wetting properties to evaluate the degree of interfacial gas layer charging for each surface and compare the effect of surface wetting property and interfacial gas layer charging on the mineral scaling process. Our hypothesis is that the entrained gas layer on superhydrophobic surfaces is essential to maintain the scaling resistance observed with superhydrophobic surfaces. Without the entrained gas layer, we expect scaling kinetics to increase with increasing surface energy and roughness.

The second objective is to systematically study the effect of surface wetting properties, i.e., surface texture and surface energy, on organic fouling. We constructed smooth and textured surfaces that mimic surface properties of membranes used in desalination, then performed atomic force microscopy (AFM) force spectroscopy measurements with model organic foulants to extract insights for developing a framework for fabricating robust fouling resistant surfaces. Our hypothesis is that the hydrophobic-hydrophobic interaction will dominate the fouling process with organic foulants and hydrophobic surfaces and that surface texture will enhance fouling, or antifouling, properties similar to the effect of roughness on hydrophobicity and hydrophilicity, respectively.

The third objective is to test the first hypothesis described above by comparing the effectiveness of purging in maintaining the performance of hydrophobic and superhydrophobic membranes subject to mineral scaling. We perform comparative MD experiments using a hydrophobic and superhydrophobic membrane subject to a saline feed solution and compare the scaling kinetics with and without periodic purging. Our hypothesis is that intermittent gas purging will not only dislodge crystals that may precipitate on the surface of the superhydrophobic membrane from the bulk, but also promote the long-term stability of the entrained gas layer on the superhydrophobic surface, ultimately, promoting long term scaling resistance that is not attainable with purging or superhydrophobic membrane alone.

The fourth objective is to demonstrate the novel ZLD and mineral crystal recovery process termed electrodialytic-crystallizer (EDC). We concentrate single salt solutions with EDC utilizing a small temperature swing crystallizer to produce and collect crystals and elucidate the role of system operating parameters on crystallization kinetics and crystal size distribution. Our hypothesis is that EDC will be capable of crystallizing salts without evaporation, but may be limited to specific salts due to the undesired transport mechanisms inherent to electrodialysis.

### 1.5. Structure of Dissertation

This dissertation is organized into six chapters. Chapter 2 discusses the effect of surface wetting properties and on the effectiveness of surface gas layer charging and their combined effect on inorganic fouling, or mineral scaling kinetics. Chapter 3 discusses the effect of surface wetting properties, i.e., surface energy and surface texture, on organic fouling adhesion properties. Chapter 4 employs the fundamental insights gleaned from Chapter 2 to demonstrate a novel mineral scaling

strategy for MD. Chapter 5 presents a novel, non-evaporative approach for achieving simultaneous zero-liquid discharge and mineral crystal recovery. Finally, Chapter 6 summarizes the main conclusions gleaned from the work in this dissertation and presents avenues for future work.

# CHAPTER 2: MEMBRANE WETTING PROPERTIES AND THEIR ROLE IN INORGANIC FOULING OF MEMBRANE DISTILLATION MEMBRANES

This chapter has been accepted for publication with minor revision in the journal ACS Environmental Au as the following peer-reviewed manuscript: **Horseman, T.**, Lin, S., Exceptional Mineral Scaling Resistance from Surface Gas Layer: Impacts of Surface Wetting Properties and Gas Layer Charging Mechanism. Accepted Environmental Au (2022).

## 2.1. Introduction

Mineral scaling, or inorganic fouling, is a phenomenon where mineral crystals precipitate out of solution and accumulate on a surface. Mineral crystals can nucleate in the bulk solution and deposit on the surface or nucleate directly on the surface. In either case, the formation and growth of a mineral crystal layer on a surface can be detrimental in different applications, including membrane separations, heat exchangers, and marine structures. For desalination membranes, mineral scaling on membranes reduces water permeability as the crystal layer blocks the membrane pores. In membrane distillation, specifically, mineral scaling can even lead to reduced salt rejection as mineral crystal growth can damage and penetrate membrane pore structure [27,45]. Mineral scaling on heat exchangers reduces the efficiency of heat exchange between the two process streams as the crystal layer adds heat transfer resistance [46–49]. On marine surfaces such as ship vessels, formation of a mineral crystal layer adds hydrodynamic resistance, which reduces fuel efficiency [50–52]. In addition to negatively affecting process efficiency, and ultimately increasing operating costs, mineral scaling can also accelerate material corrosion or degradation [53,54]. As scaling can compromise or even cause these processes to fail, the mechanism of mineral scaling and its mitigation strategies have been extensively studied [20,55–63].

Common industrially relevant scalants such as gypsum ($CaSO_4$-$2H_2O$), calcite ($CaCO_3$), and silicates have been extensively studied due to their low solubility and thus high propensity to precipitate and form a mineral scaling layer [45]. In the context of membrane distillation, it has been shown that superhydrophobic membranes can significantly reduce mineral scaling via decreasing the propensity for heterogenous crystal nucleation on the surface, reducing the residence time for crystal nucleation, deposition, or growth in the boundary layer near the surface due to slip boundary condition, and decreasing solid-liquid contact available for crystal nucleation and/or deposition and growth on the surface [45,64,65]. More generally, the excellent scaling resistance of superhydrophobic surfaces in the context of membranes [12,66–69], heat exchangers

[70–73], and marine surfaces [74] is associated with the Cassie-Baxter wetting state. However, it has also been shown that the Cassie-Baxter states of many systems are metastable, i.e., these system eventually transitioned to Wenzel state as the entrapped gas layer vanished via gradual gas dissolution or mechanical perturbation [75–78]. Therefore, process optimization to maintain the gas layer and prolong the stability of this Cassie-Baxter wetting state is critical to sustain long-term scaling resistance.

In addition to superhydrophobic surfaces, which are not necessarily deployable in all contexts, strategies for mitigating mineral scaling on smooth or even hydrophilic surfaces are also of great practical interest. While the intrinsic effects of surface roughness and surface energy on mineral scaling has been elucidated in previous studies [79–85], the impacts of the presence of surface nanobubbles on scaling resistance has not been fully understood. It has been shown that surface nanobubbles exist on submerged hydrophilic and hydrophobic surfaces, and that these bubbles are stable there for days [86–95]. Can we leverage these stable nanobubbles to enhance the scaling resistance of smooth hydrophilic and hydrophobic surfaces that do not intrinsically entrap a gas layer?

In this study, we demonstrate the influence of surface wetting properties and the interfacial gas layer charging on calcium carbonate ($CaCO_3$) scaling kinetics. We employ a well-established solvent exchange process to produce interfacial gas bubbles [87,90,96–99] on quartz crystal microbalance (QCM) sensor surfaces with hydrophilic, hydrophobic, and superhydrophobic wetting properties. We evaluate the degree of interfacial gas layer charging for each surface and compare the effect of surface wetting property on the effectiveness of interfacial gas layer charging. After generating interfacial gas bubbles using solvent exchange, we expose the gas-charged surfaces to $CaCO_3$ scaling solution to evaluate how the interfacial gas layer influences the mineral scaling process. We characterize the scaling kinetics in long-term scaling experiments via quartz crystal microbalance with dissipation monitoring (QCM-D) and characterize surface scale morphology with scanning electron microscopy equipped with energy dispersive X-ray analysis (SEM-EDX). Based on data obtained the QCM-D experiments and SEM-EDX characterizations, we compare the effectiveness of $CaCO_3$ scaling mitigation between surfaces with different wetting properties and gas-charging mechanisms.

## 2.2. Materials and Methods

### *2.2.1. Chemicals*

Sulfuric acid ($H_2SO_4$, 96% aqueous solution) and hydrochloric acid (HCl, ACS grade, 12M) were purchased from Fisher Scientific (MA, USA) and ethanol (200 proof) was purchased from Decon Labs, Inc. (PA, USA). Acetone (ACS reagent-grade, ≥ 99.5%), hydrogen peroxide ($H_2O_2$, 30 wt%), 1H, 1H, 2H, 2H perfluorodecyltriethoxysilane (FAS, 97%), methyltrichlorosilane (MTS, 99%), and toluene (anhydrous, 99.8%) were all purchased from Millipore Sigma (MA, USA). Calcium chloride ($CaCl_2$, anhydrous, > 95%) and sodium carbonate ($Na_2CO_3$, anhydrous, ACS Grade) were purchased from Research Products International (IL, USA).

### *2.2.2. Surface Fabrication and Characterization*

All surfaces were created by modifying polished silicon dioxide ($SiO_2$) coated substrates. Specifically, quartz crystal sensors (QSense QSX 303 from Biolin Scientific, SE) were used for QCM-D experiments, and 5 × 5 mm diced $SiO_2$ substrates (Ted Pella, Inc., CA, USA) were used for SEM imaging. To obtain the hydrophilic surface, the $SiO_2$ surface was rinsed with ethanol, acetone, and deionized (DI) MilliQ water then placed in a UV/Ozone cleaner (M42, Jelight) for 10 minutes. The plasma cleaned surface was then transferred to a piranha solution (3:1 mixture of $H_2SO_4$ and $H_2O_2$) for 20 seconds. The surface was rinsed with DI water and blown dry with compressed nitrogen gas and immersed in DI MilliQ water before experiments. This process was repeated every time the hydrophilic surface was used.

To obtain the hydrophobic surface, the $SiO_2$ surface was first hydroxylated with the hydrophilic treatment stated above. The hydroxylated surface was blown dry with nitrogen gas, heated at 100°C for 10 minutes, then immediately placed in a closed petri dish with multiple drops (10 µL) of 1H, 1H, 2H, 2H-perfluorodecyltriethoxysilane (FAS). The dish was held at 70°C overnight at negative 0.8 megapascal for coating the hydroxylated $SiO_2$ surface with FAS via chemical vapor deposition.

To obtain the rough and superhydrophobic surface, a three-dimensionally rough hydrophobic film was created by polymerization on the polished $SiO_2$ surface. First, the $SiO_2$ surface was hydroxylated with the hydrophilic surface treatment detailed earlier. The surface was blown dry with nitrogen gas and heated at 100°C for 10 minutes then immediately placed in toluene with 55 mM methyl trichlorosilane. The reaction vessel was tightly sealed and gently mixed for 3-4 hours

at room temperature. The surface was then rinsed sequentially with ~25 mL of toluene, ethanol, and DI water, blown dry with compressed nitrogen, and annealed at 100°C for 5 minutes.

We compared the wetting properties of the surfaces by measuring the static water contact angle (CA) with an optical tensiometer (T114, Attension). The CA hysteresis was quantified by measuring the sliding angle (SA), i.e., the critical tilting angle at which the water droplet de-pins from its original location and slides down the substrate surface.

*2.2.3. Solvent Exchange and Scaling Experiments.*

A well-established solvent exchange method was applied on the three surfaces where a sudden decrease in gas solubility was used to induce bubble nucleation (**Figure 2.1A**) [87,90,96–99]. First, solution 1, held at 20°C and with dissolved gas solubility $S_{gas,1}$, was injected at 50 µL min$^{-1}$ into the flow cell that was held at 50°C. This solution injection is considered the start of the experiment (i.e., t = 0). The sudden temperature change in the solution near the surface induces initial gas bubble nucleation due to the gas solubility decrease associated with temperature [100]. After 10 minutes, solution 2 with bulk gas solubility $S_{gas,2}$, was injected also at 50 µL min$^{-1}$ into the flow cell at 50°C. Solution 2 has a lower gas solubility than solution 1 ($S_{gas,1}/\ S_{gas,2} \sim 10^1 - 10^3$) due to the reduction in solubility by temperature and salinity, so the sudden change in gas solubility at the mixing frontier resulted in more nanobubble nucleation on or near the sensor surface [97].

In the control experiment, both solution 1 and solution 2 were degassed (**Figure 2.1B**), so no dissolved gas was present to nucleate on the surfaces, and thus, any frequency or dissipation response during the solvent exchange were caused by changes in bulk solution properties (discussed in more detail later). These values were subtracted from the surface bubble and bulk bubble experiments to isolate the response due to nanobubble nucleation and/or adsorption. In the reference experiment, solution 1 was ethanol while solution 2 was water. The ethanol/water solvent exchange has been utilized extensively in literature to induce nanobubble nucleation including fundamental studies using QCM-D [96,101]. The reference experiment served to validate the protocol and observations in this study.

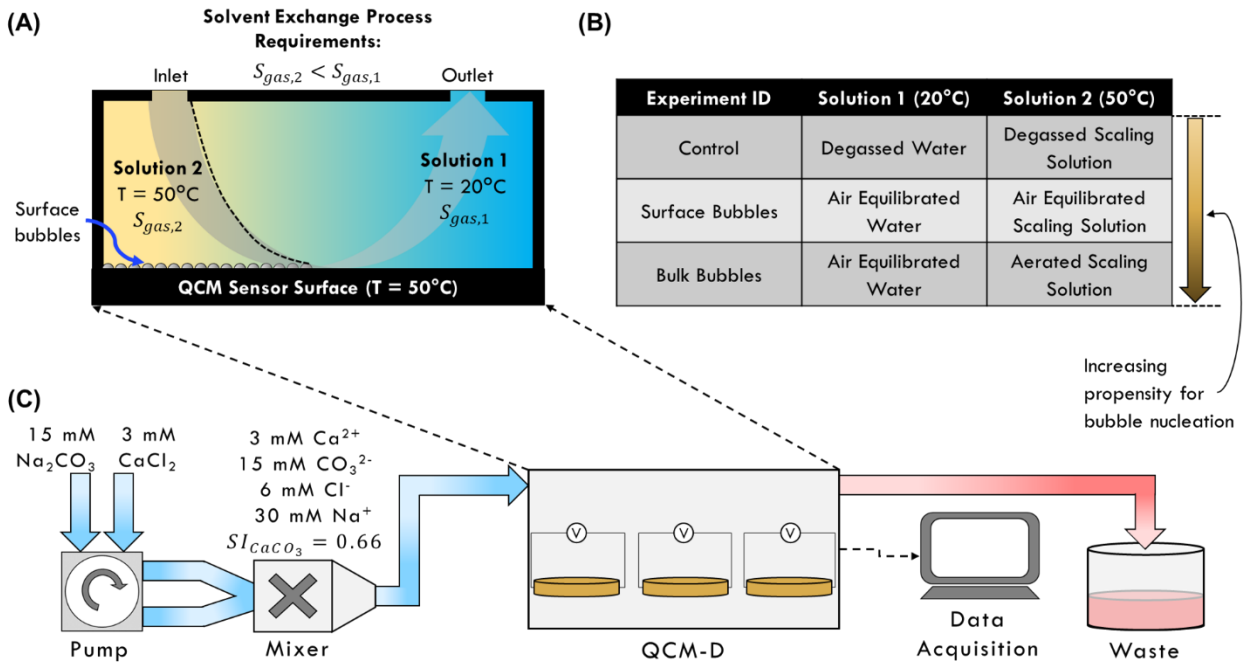


**Figure 2. 1.** (A) Schematic diagram of the solvent exchange process employed to establish interfacial gas layers in this study. Initially, the QCM cell is heated to 50°C and the crystal resonances are found in degassed DI water at 50°C. Then solution 1, at 20°C with gas solubility, $S_{gas,1}$, is injected into the cell where the sudden change in dissolved gas solubility due to temperature change induces bubble nucleation near the sensor surface. Next solution 2, at 50°C with gas solubility, $S_{gas,2}$, is injected into the cell. As the gas solubility of solution 2 is less than that of solution 1, i.e., $S_{gas,2} < S_{gas,1}$, due to temperature and salinity induced solubility difference, the mixing of the two solutions induces dissolved gas nucleation at the mixing frontier. (B) Description of the solutions used for solvent exchanges. (C) Schematic diagram of experimental setup used to study the influence of interfacial gas layers on calcium carbonate scaling kinetics with QCM-D.

The control, surface bubbles, and bulk bubbles experiments were strategically selected with increasing propensity for bubble nucleation and adsorption, and thus surface bubble coverage (**Figure 2.1B**). For example, both solution 1 and 2 in the control experiment were degassed, and thus no dissolved gases were present for bubble nucleation, while in the surface and bulk bubble experiments, the gas solubility ratio between solution 1 and 2 was on the order of $10^3$ [102–104]. Furthermore, solution 2 in the bulk bubble experiment was aerated with nitrogen gas with a nanobubble generator (25 nanoBoost with NPE pump, Moleaer Inc., NY, USA), giving the highest propensity for bubble coverage as bulk bubbles may also adsorb to the surface from the bulk [95,105,106]. The aerated solutions contained $1 \pm 0.2 \times 10^8$ $mL^{-1}$ of nanobubbles averaging 183 ± 11 nm in diameter (**Figure 2.2**, Malvern Nanosight NS300, UK).

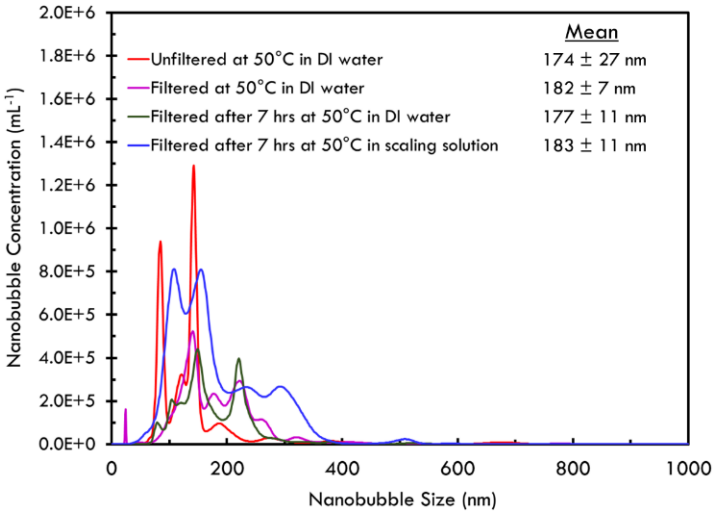


**Figure 2. 2.** Nanobubble concentration and size analysis after 10 min bubble generation in the Molear Boost supplied with 2.0 CFH nitrogen. The reservoir was allowed to sit at least 10 min before samples were removed to allow larger bubbles to destabilize. Nanobubble size and concentration was measured in deionized (DI) water at 50°C both with (light blue) and without filtering (red). Filtering did not remove or significantly effect the size distribution or concentration of nanobubbles. Nanobubble size and concentration in deionized water at 50°C after 7 hours and filtration (brown). Bubbles were stable for the 7 hours with no change in bubble size distribution of concentration. Nanobubble size and concentration in $CaCO_3$ scaling solution at 50°C (SI = 0.66) after 7 hours and filtration (blue). There was no significant effect on bubble size distribution or concentration.

In the control, surface bubble, and bulk bubble experiments, the solvent exchanges were first conducted with the respective solutions listed in **Figure 2.1B** to establish gas bubbles (or the lack thereof in the case of the control) on the surfaces. Immediately following the solvent exchanges, and without removing solution from the cell, solution 2 continued to flow over the sensor surface for a total of 7 hours to elucidate the effect of surface bubble coverage on mineral scaling. The scaling solutions were prepared by mixing a solution of 3 mM calcium chloride ($CaCl_2$) and a solution of 15 mM sodium carbonate ($Na_2CO_3$). Prior to mixing, the water was degassed (control), air equilibrated (surface bubbles), or aerated (bulk bubbles), held at 50°C and sealed from the ambient environment. The solutions were pumped to a mixer just before the QCM-D cell to form a saturated calcium carbonate scaling solution (SI = 0.66 calculated via PHREEQC v3.4, USGS) that then flowed into separate QCM-D cells over the fabricated sensor surfaces (**Figure 2.1C**).

*2.2.4. Quartz Crystal Microbalance Experiments.*

The solvent exchange and scaling experiments were conducted using a quartz crystal microbalance with dissipation monitoring (QCM-D, QSense E4 Analyzer, Sweden). After surface

modification, the quartz crystal sensors were transferred to their respective flow cells, which were held at 50°C. Degassed deionized MilliQ water, held at 50°C, was then injected into the cell at 50 μL $min^{-1}$ for 10 min to equilibrate the sensor. After equilibration, the sensor's resonant frequencies were found using the QSense Dfind software and a stable baseline was established (≤ 2 Hz frequency drift and ≤ 0.2 $\times 10^{-6}$ dissipation drift). Sensors that cannot result in stable baseline were replaced. After establishing stable baselines, the frequency and dissipation responses were recorded over the entire solvent exchange and scaling experiments and analyzed with the QSense Dfind software.

*2.2.5. Mineral Scaling Characterization.*

Polished $SiO_2$ wafers (5 × 5 mm diced $SiO_2$ substrates from Ted Pella, Inc., CA, USA) were subject to identical surface fabrication procedures mentioned previously to produce hydrophilic, hydrophobic, and superhydrophobic wetting properties. These wafers were then inserted into a closed flow cell and subjected to the identical solvent exchange and scaling experimental conditions. To analyze the morphology of the mineral crystal layer after scaling experiments, the scaled surfaces were immediately removed from the flow cell and excess solution was blown off the surfaces with compressed nitrogen. The surfaces were imaged via scanning electron microscope fit with energy dispersive X-ray detector (SEM-EDX, Merlin, Zeiss, DE).

## 2.3. Results and Discussion

*2.3.1. QCM-D response to gas layer formation and mineral scaling*

In all experiments, QCM with dissipation (QCM-D) monitoring was used to evaluate the effect of surface wetting properties and solution conditions on gas bubble surface coverage during the solvent exchanges. After the solvent exchanges, scaling solution continued to flow over the quartz crystal sensors and QCM-D was used to elucidate the effect of gas bubble surface coverage on mineral scaling. For rigid mass coupling with the sensor surface, should it be liquid, gas bubbles, or mineral crystals, mass adsorption follows the Sauerbrey relationship (**Equation 2.1**) [107].

$$\Delta f_n = -\frac{n}{C}\Delta m \tag{2.1}$$

where $\Delta f_n$ is the change in resonant frequency of the quartz crystal oscillator upon adsorption of mass (in $Hz$), $n$ is the overtone order relative to the first harmonic resonant frequency (dimensionless), $C$ is the mass sensitivity constant (-17.7 ng $Hz^{-1}$ $cm^{-2}$ for the 5 MHz crystals used in this work), and $\Delta m$ is the areal mass density (in $ng\ cm^{-2}$) [108]. We note that the rigid film

approximation, empirically limited to $\Delta D_n / \Delta f_n < 10^{-7}\ Hz^{-1}$ by the manufacturer, where $\Delta D_n$ is the change in energy dissipation (dimensionless), is satisfied for all experiments. Thus, the rigid film assumption that validates the Sauerbrey relationship holds for all surface mass adsorption/desorption in this study [108,109]. In general, surface bubble nucleation and adsorption cause a positive frequency shift as denser liquid mass is replaced by gaseous mass at the sensor surface, while mineral scaling results in negative frequency shift as liquid/gaseous mass is replaced by the denser mineral crystals at the sensor surface (**Figure 2.3A**). This is a commonly observed phenomenon that can be well explained by the Sauerbrey equation (**Equation 2.1**) [96,101,110,111].

Along with validating the rigid film approximation, dissipation monitoring provides insight into the rigidity of the coupling between absorbed mass and the sensor surface [108]. In general, mineral crystal nucleation and/or deposition on the sensor surface increased dissipation, indicating an increasing non-rigid coupling between the mineral crystals and sensor surface (**Figure 2.3B**). Interestingly, surface bubble nucleation and adsorption resulted in a negative dissipation shift, indicating a "more rigid" coupling between the bubble covered surface and liquid. This phenomenon is most likely caused by the significant reduction in frictional drag between the liquid and sensor surface as nanobubbles displace water at the interface [96]. For a bubble-free liquid-solid surface coupling with the hydrophilic and hydrophobic surfaces in this study, the non-slip boundary condition tethers liquid to the sensor surface and results in positive dissipation due to energy dissipation via viscous force. However, the presence of surface gas bubble reduces such tethering and may even create a slip-boundary condition at the liquid-sensor interface that minimizes viscous energy dissipation.

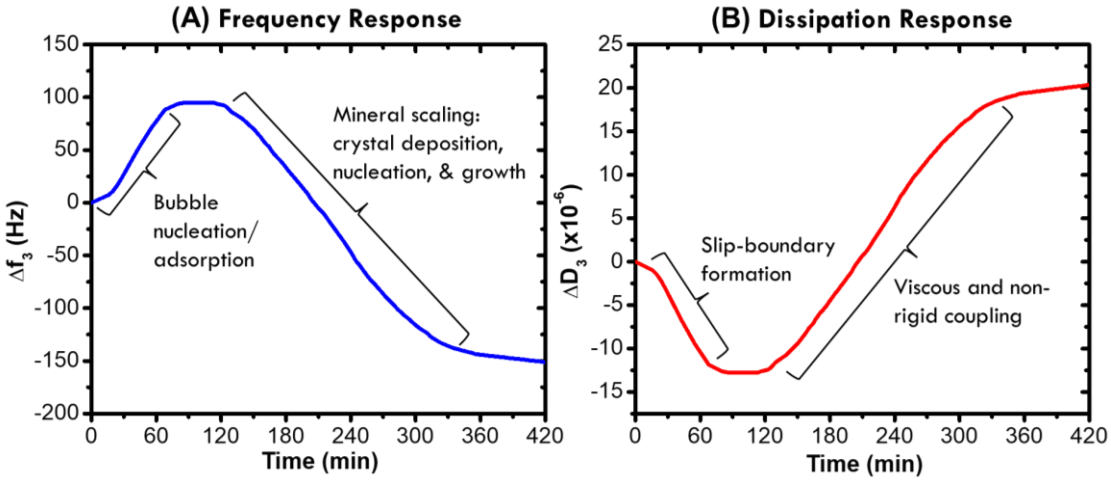


**Figure 2. 3** Representative QCM-D data including (A) frequency and (B) dissipation responses in QCM-D scaling experiments. Initially the solvent exchanges from **Figure 2.1B** were conducted in the first 10 minutes of the experiment, inducing positive frequency shifts as gas nanobubbles deplete water from the sensor surface. Positive frequency shift is indicative of the water layer at the sensor surface being replaced by the less dense gas bubbles. As bubbles nucleate and adsorb to the sensor surface, dissipation response decreases due to a slip-boundary formation that alleviates viscous energy dissipation that occurs when the sensor is in contact with purely liquid. Eventually the surface bubble layer equilibrates, and the frequency and dissipation responses stabilize for a short period of time (30-60 min) until mineral crystal nucleation/deposition occurs, resulting in negative frequency shift and positive dissipation shift. The negative frequency shift is caused by the denser mineral crystals replacing liquid or gas at the sensor surface, while the positive dissipation shift is due to non-rigid coupling between mineral crystals and the QCM sensor surface.

In liquids, the frequency response is proportional to the square root of bulk liquid viscosity and density (**Equation 2.2**) [112–114].

$$\Delta f_n = -\frac{1}{C}\sqrt{\frac{n\rho_l\eta_l}{2\omega_F}} \tag{2.2}$$

where $\rho_l$ is the bulk liquid density, $\eta_l$ is the bulk liquid viscosity, and $\omega_F$ is the angular fundamental resonance frequency. According to **Equation 2.2**, the changes in liquid density and viscosity (which are both temperature and salinity dependent) from solutions 1 to 2 should induce a change in resonant frequency. In the control experiment, the solutions were degassed, i.e., dissolved gases present for possible bubble nucleation or adsorption were removed, to quantify the effect of changing solution density and viscosity on frequency response according to **Equation 2.2**. Any frequency or dissipation shift measured during the control experiment was subtracted from the frequency or dissipation shifts measured during the surface bubble and bulk bubble solvent exchanges to isolate the nanobubble specific responses.

*2.3.2. Surface Wetting Properties*

Hydrophilicity was imparted on a polished silicon dioxide quartz crystal surface by hydroxylating with UV/Ozone plasma and a short piranha etch. Complete wetting of the hydrophilic surface was indicated by a contact angle (CA) of zero (**Figure 2.4A**). Another polished silicon dioxide quartz crystal was hydroxylated, and a long-chain fluoroalkyl-silane (FAS) was grafted to it via chemical vapor deposition to produce a hydrophobic surface. The measured sessile drop CA of 107° ± 3° indicates hydrophobicity (**Figure 2.4B**). For either surface, the unmeasurable sliding angle (SA) indicates the presence of pinning between water and the sensor surface which leads to non-slip boundary condition for water flow along the surface. We note that the hydrophilic and hydrophobic quartz crystal surfaces were both polished to a root-mean-square (RMS) surface roughness less than 1 nm, and that the hydrophilic and hydrophobic surface treatments did not increase the surface roughness of the sensors [115,116].

Superhydrophobicity was imparted on a polished silicon dioxide quartz crystal by immersing the hydroxylated surface in toluene containing methyl trichlorosilane. A contact angle (CA) of 168° ± 6° and a sliding angle (SA) of 9° ± 4° were measured (**Figure 2.4C** left), indicating the achievement of superhydrophobicity (typically defined by a sessile drop CA > 150° and an SA < 10°). The three-dimensional polymer network that forms upon methyl trichlorosilane reaction with the hydroxylated surface creates a rough, nano-porous structure with multiscale roughness that entrains a metastable gas layer upon which the contacting liquid is suspended (**Figure 2.4C** right) [117]. In such a Cassie-Baxter wetting state, the small fraction of contact between the solid surface and the liquid ($f$) can be estimated using the Cassie-Baxter equation (**Equation 2.3**) [118,119].

$$cos\,\theta_A = f(cos\,\theta_0 + 1) - 1 \qquad (2.3)$$

where $\theta_A$ is the apparent CA and $\theta_0$ is the intrinsic CA (i.e., the CA on a molecularly smooth surface made of the same material as the rough surface that yields $\theta_A$). While we do not know the exact $\theta_0$ for a smooth methyl trichlorosilane-treated surface, it should be lower than that of FAS-grafted smooth surface (i.e., 107°) because a long-chain fluoroalkyl group is more hydrophobic than a methyl group due to both chain length and moiety. But even if we assume the methyl trichlorosilane-treated surface also has $\theta_0$ of 107° (should be lower in reality), applying equation 3 with a measured $\theta_A$ of 168° results in an aerial fraction of solid-water contact ($f$) of 3%. With a lower $\theta_0$ for methyl trichlorosilane-treated surface, $f$ is likely even smaller. Thus, the interfacial

contact on the superhydrophobic surface is dominated by the entrapped gas layer, which possesses at least 97% of the interfacial contact with the liquid.

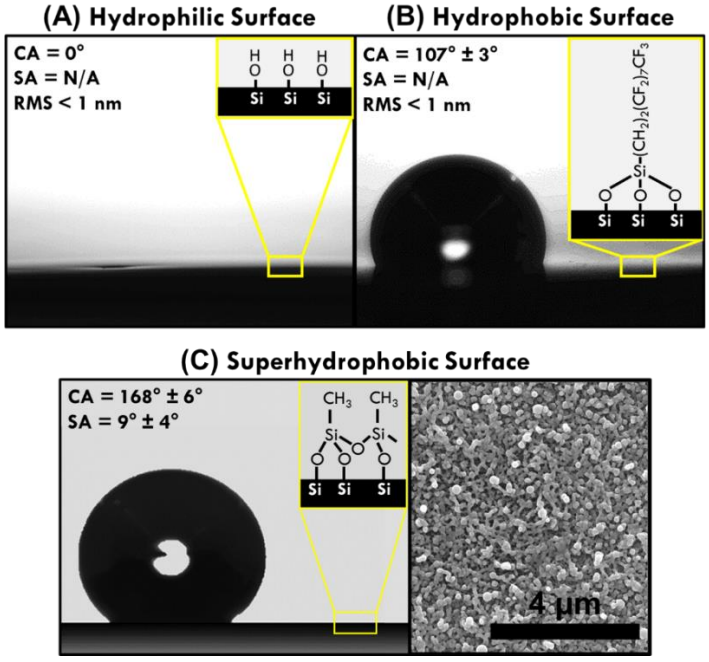


**Figure 2. 4**. Wetting properties of the smooth (A) hydrophilic and (B) hydrophobic surfaces and the rough (C) superhydrophobic surface. Contact angle (CA), sliding angle (SA), or the minimum tilt angle required to cause a droplet to unpin from the surface, and surface roughness, reported as the root mean square (RMS) surface roughness reported in the top left of the image. The SA was unmeasurable on both hydrophilic and hydrophobic surfaces as the water stayed attached to the surface even when inverted. SEM image of the rough superhydrophobic surface in (C) shows the rough nanoporous 3D methyl siloxane polymer network. Insets show the surface chemistry employed to achieve the desired wetting properties.

*2.3.3. Gas layer formation: impacts of surface wetting property and bubble generation method*

The solvent exchange solutions were chosen to systematically study the effect of surface wetting properties on gas layer surface coverage. QCM-D was used to semi-quantitatively monitor the extent of surface bubble coverage; as the less dense bubbles replaced a volume of water at the sensor surface, the frequency of the oscillating system increased (**Equation 2.1**). The magnitude of the positive frequency shifts increased as the propensity for surface bubble coverage increased, as expected by the experimental design (**Figure 2.5**). For example, in the control experiment, where the solutions were degassed and has no propensity for bubble nucleation, there was little to no positive frequency shift observed, while in the surface bubble and bulk bubble experiments, where the ratio of dissolved gas solubility was on the order of $10^3$, noticeable positive frequency shifts were observed.

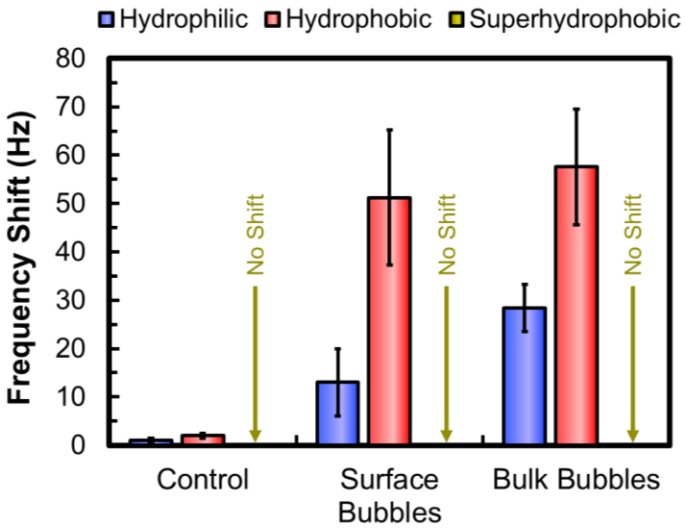


**Figure 2. 5.** Positive frequency shifts observed on hydrophilic (blue), hydrophobic (red), and superhydrophobic (dark yellow) surfaces from **Figure 2.4** after the control, surface bubbles, and bulk bubble experiment solvent exchanges from **Figure 2.1B**. The positive frequency shifts observed in the control experiments were subtracted from the surface bubble and bulk bubble frequency shifts to remove any response measured due to the changing solution densities and viscosities during the solvent exchanges. The maximum positive frequency shift was recorded after the surface bubble layer equilibrated and frequency response remained constant for at least 30 minutes. No positive frequency shifts were observed on the superhydrophobic surface. Error bars reflect the standard deviation over three trials.

The magnitude of the positive frequency shift increased from 13 ± 7 Hz on the hydrophilic surface in the surface bubble experiment to 28 ± 5 Hz in the bulk bubble experiment likely because of increased surface bubble coverage as bubbles adsorbed from the bulk solution [101]. While the magnitude of the average positive frequency shift on the hydrophobic surface did slightly increase from 51 ± 14 Hz in the surface bubble experiment to 58 ± 12 Hz in the bulk bubble experiment, these values are relatively similar within experimental error. This is likely because the hydrophobic surface was nearly saturated with adsorbed bubbles in both the surface and bulk bubble experiments. We note that the positive frequency shifts measured on the hydrophobic surfaces were consistently larger than those measured on the hydrophilic surfaces (**Figure 2.5**), which is consistent with previous studies [96]. This phenomenon can be explained by a combination of two effects (1) propensity for bubble nucleation on the hydrophobic surface was greater due to lower energy barrier for nucleation [120] and (2) long-range hydrophobic-hydrophobic interaction between the gas bubbles and hydrophobic surface favors bubble adsorption from the bulk [121]. While the effects of the solvent exchanges were readily observed on the smooth hydrophilic and hydrophobic surfaces, they did not produce positive frequency shifts on the superhydrophobic

surface (**Figure 2.5**). This is likely because a gas layer is intrinsically present in a submerged superhydrophobic surface and any bubbles that nucleated or adsorbed on the superhydrophobic surface rapidly coalesced into the entrapped gas layer already present there.

In the reference experiment, where the ratio of dissolved gas solubility between solution 1 (ethanol) and solution 2 (water) was on the order of ~$10^1$, a positive frequency shift of 4 ± 1 Hz on the hydrophilic surface and 38 ± 8 Hz on the hydrophobic surface were observed (**Figure 2.6**). The magnitudes of the shifts in the reference experiment were very similar to what has been reported for similar surfaces, identical solvent exchanges, and with the same QCM-D instrument [96]. Notably, the positive frequency shifts in the reference experiment were also less than what was observed in the surface bubbles and bulk bubbles experiments where the ratio of dissolved gas solubility between solution 1 (water) and solution 2 (scaling solution) was on the order of ~$10^3$. This evidence not only serves to validate our experimental observations but gives support that increasing dissolved gas solubility difference between solution 1 and solution 2 produces higher positive frequency shift, and thus results in more interfacial gas bubble formation.

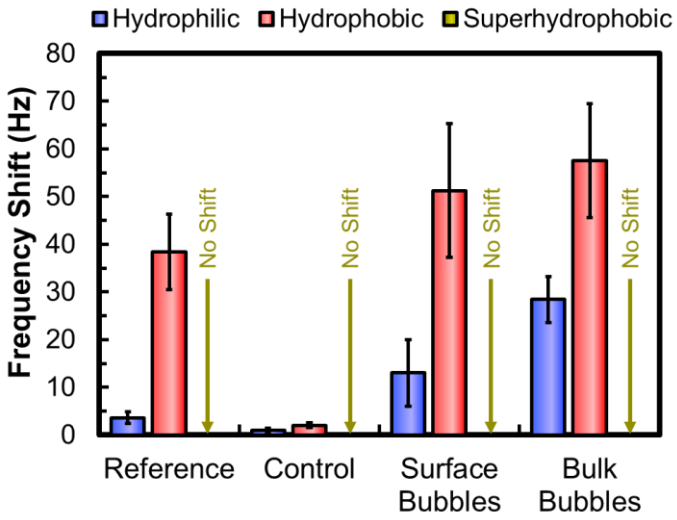


**Figure 2. 6**. Positive frequency shifts observed on hydrophilic (blue), hydrophobic (red), and superhydrophobic (dark yellow) surfaces from **Figure 2.4** after the reference, control, surface bubble, and bulk bubble experiment solvent exchanges from **Figure 2.1B**. The positive frequency shifts observed in the control experiments were subtracted from the surface bubble and bulk bubble frequency shifts to remove any response measured due to the changing solution densities and viscosities during the solvent exchanges. The maximum positive frequency shift was recorded after the surface bubble layer equilibrated and frequency response remained constant for at least 30 minutes. No positive frequency shifts were observed on the superhydrophobic surface. Error bars reflect the standard deviation over three trials.

*2.3.4. Impacts of gas layer formation on mineral scaling kinetics*

After solvent exchange, the mineral scaling solution (i.e., solution 2 in the control, surface bubbles, and bulk bubbles experiments) flowed over the sensor surface for a total of seven hours to allow the study of the effect of the surface bubble coverage on the mineral scaling process. As surface bubbles or water are replaced by the denser mineral crystals at the sensor surface, a negative frequency shift was observed (**Figure 2.7** top row). While mineral crystal mass deposition did tend to form a less rigid film, as indicated by the positive dissipation shifts (**Figure 2.7** bottom row), the rigid film approximation held in all experiments and, thus, the Sauerbrey equation was used to model the mass accumulation on each surface (**Equation 2.1**). We note that the reference solvent exchange was carried out for a total of eight hours and showed that the submerged gas layer was stable for the entire experiment (**Figure 2.8**). This long-term gas bubble stability on submerged surfaces has also been well documented in the literature [86,94,122].

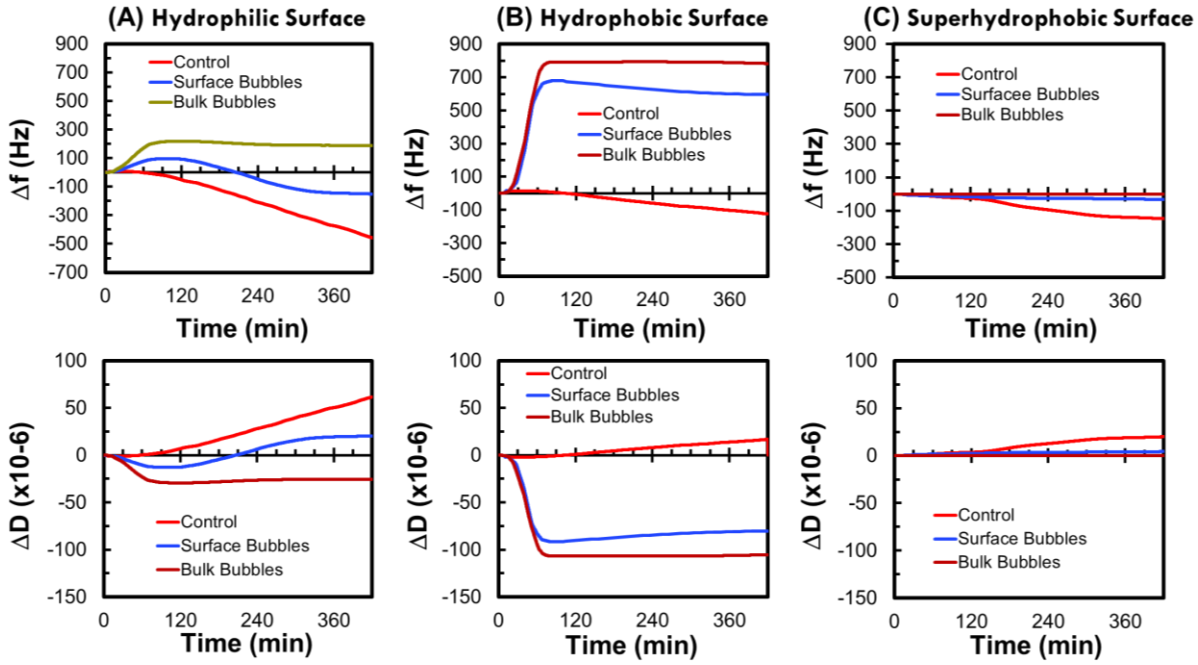


**Figure 2. 7.** (Top Row) Frequency shifts recorded during the control, surface bubbles, and bulk bubble experiments in this study on the (A) hydrophilic surface, (B) hydrophobic surface, and (C) superhydrophobic surface. (Bottom Row) Dissipation shifts recorded during the control, surface bubbles, and bulk bubble experiments in this study on the (A) hydrophilic surface, (B) hydrophobic surface, and (C) superhydrophobic surface.

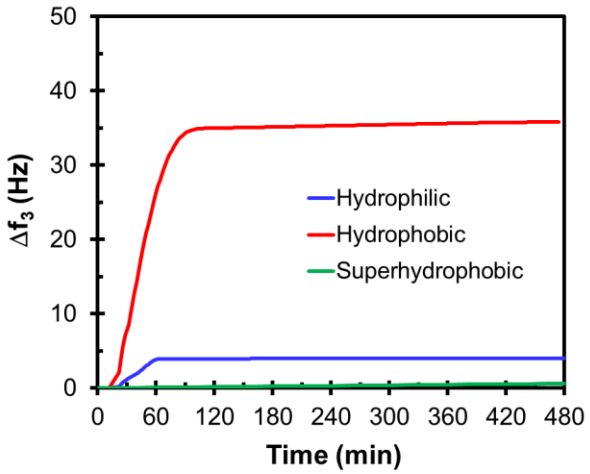


**Figure 2. 8** Long solvent exchange with reference solutions from **Figure 2.1B** (solution 1: air equilibrated ethanol at 20°C, solution 2: air equilibrated water at 50°C). After the bubble layer forms and equilibrates, it is stable for the entire 7-hour experiment, realized by the stable frequency shift from ~60-90 min to 480 min.

In these experiments, the control represents the scaling response in the absence of a surface bubble layer, while the surface bubble coverage increased from the surface bubble experiment to the bulk bubble experiment for both the hydrophilic and hydrophobic surface (**Figure 2.9**). As surface bubble coverage increased, mineral scaling kinetics decreased. Specifically, the induction time for mineral nucleation/deposition, indicated by the onset of mass accumulation on the surface, was longer as the surface bubble coverage increased (**Figure 2.9A & 2.9B**). Likewise, the final mass of crystals deposited on the surface decreased with the surface bubble coverage. The trend between crystallization kinetics and surface bubble coverage holds true for different solvent exchanges on the same surface or for the same solvent exchange on different surfaces.

For the superhydrophobic surface, positive frequency shift was not observed upon the introduction of surface or bubbles, likely because submerged superhydrophobic membrane spontaneously bore an air film that led to the slip boundary condition even without bubble introduction. However, even with superhydrophobic surface, the introduction of surface or bulk bubbles still contribute to enhanced scaling resistance (**Figure 2.9C**). Like experiments with other surfaces, mitigation of scaling on a superhydrophobic membrane was more effective with bulk bubbles than with surface bubbles. Interestingly, the final mineral crystal mass deposited on a superhydrophobic surface after the control solvent exchange (i.e., with degassed solutions) was very similar to that on the hydrophobic surface. With a degassed solution flowing over the superhydrophobic surface, there was a large driving force for the entrapped gas layer to destabilize

and dissolve into the degassed solution and promote a transition from the Cassie-Baxter to the Wenzel wetting state. At the Wenzel state, scaling kinetics was even slightly faster on the "superhydrophobic" surface compared to the smooth hydrophobic surface, likely because (1) the surface energy of short chain methyl-terminated surfaces is higher than long chain perfluorinated surfaces; and (2) the wetted superhydrophobic surface, due to its porosity, has a higher specific surface area than the smooth hydrophobic surface.

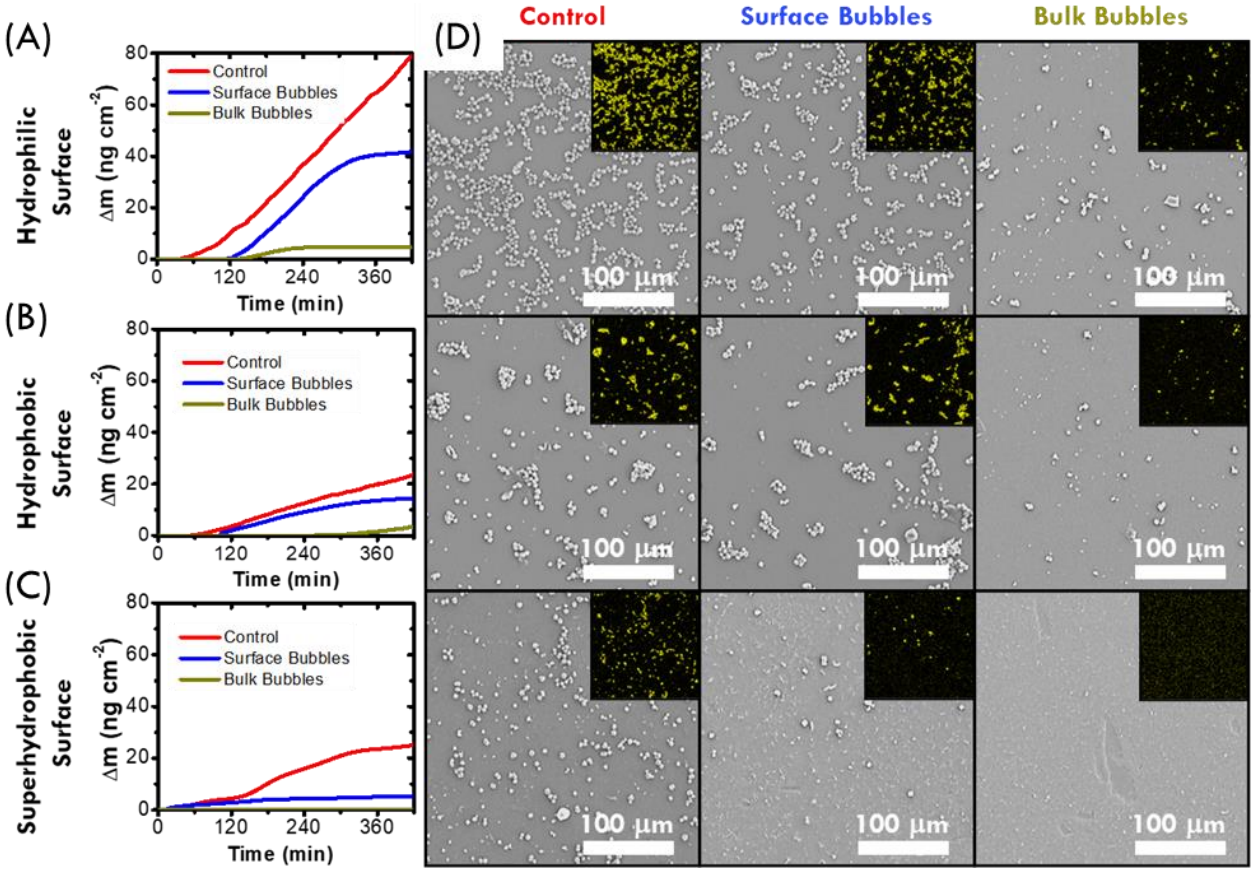


**Figure 2. 9.** Areal mass density of scale accumulated on (A) hydrophilic, (B) hydrophobic, and (C) superhydrophobic surfaces in long-term scaling experiments measured via QCM-D. (D) SEM images of the scaled surfaces after the scaling experiments in (A-C). Inset shows EDX map of calcium (yellow) on the surface. The experiment ID's refer to the initial solvent exchanges according to **Figure 2.1B**. Degassed deionized (DI) water was used to find the crystal resonances and establish stable baseline for ~10 min, then the solvent exchange was conducted to produce an interfacial gas layer. The scaling solution flowed at 50 µl $min^{-1}$ over the sensors for a total of 7 hours after said solvent exchange. The baseline for mass accumulation began once the surface bubble layer equilibrated and the frequency response stabilized for at least 30 min (**Figure 2.7**).

Images of the final mineral scaling layer on each surface obtained with the scanning electron microscope equipped with energy dispersive x-ray (SEM-EDX) detector reveals the mineral crystal surface coverage decreased as the surface bubble coverage increased, supporting the

findings from QCM-D experiments (**Figure 2.9D**). Furthermore, there was a strong correlation between final mineral crystal mass measured via QCM-D and mineral crystal areal surface coverage measured from SEM-EDX images (**Figure 2.10**). For example, the final mass measured via QCM-D on the hydrophilic surface with the control solvent exchange (80 ng $cm^{-2}$) was approximately twice as that measured on hydrophilic surface with the surface bubble solvent exchange (41 ng $cm^{-2}$, **Figure 2.9A & 2.10**). SEM-EDX mapping confirms that approximately half the amount of mineral crystal was deposited on the hydrophilic surface during the surface bubble solvent exchange compared to the control solvent exchange with degassed solution (**Figure 2.10**). Similar correlation was observed between the hydrophilic (**Figure 2.9A**) and hydrophobic (**Figure 2.9B**) surface with the same solvent exchange. For example, approximately half of the mineral crystal deposit was observed on the hydrophobic surface as compared to the hydrophilic surface in the absence of a submerged gas layer in the control solvent exchange experiment (**Figure 2.9D & 2.10**).

The final mineral crystal mass deposited on the superhydrophobic surface after the surface bubble experiment (5 ng $cm^{-2}$, **Figure 2.9C**) was much less than that on the hydrophobic surface (14 ng $cm^{-2}$, **Figure 2.9B**). This is likely caused by the larger degree of gas-liquid contact at the superhydrophobic surface induced by Cassie-Baxter wetting state as compared to the Wenzel wetting state on the hydrophobic surface with discrete nanobubble coverage. More importantly, virtually no mineral crystal mass accumulation on the superhydrophobic surface was detected by QCM-D or SEM-EDX after the bulk bubble solvent exchange (**Figure 2.9C & 2.9D**). As adsorption and coalescence of bulk nanobubbles continuously recharged the entrapped gas layer on the superhydrophobic surface, thereby maintaining a robust Cassie-Baxter state and contributing to exceptional long-term scaling resistance.

The observed trend of improved mineral scaling resistance by increasing the surface hydrophobicity of the smooth surfaces can be explained by a reduced propensity for crystal nucleation and growth on the more hydrophobic surface [45]. This is true in the absence of a surface bubble layer in the control experiments where the intrinsic surface energy of the hydrophobic surface alone reduced the propensity for mineral crystal nucleation relative to that of the hydrophilic surface. However, in the presence of interfacial bubbles in both the surface bubble and bulk bubble experiments, mineral scaling kinetics were even slower on the hydrophobic surface than in the control experiment or the same solvent exchanges on the hydrophilic surfaces.

The exceptional scaling resistance was attributable to the enhanced degree of interfacial bubble formation on the hydrophobic surface. Surface bubbles acted to physically shield the surface from mineral crystal nucleation or deposition as they reduced the area of solid-liquid contact.

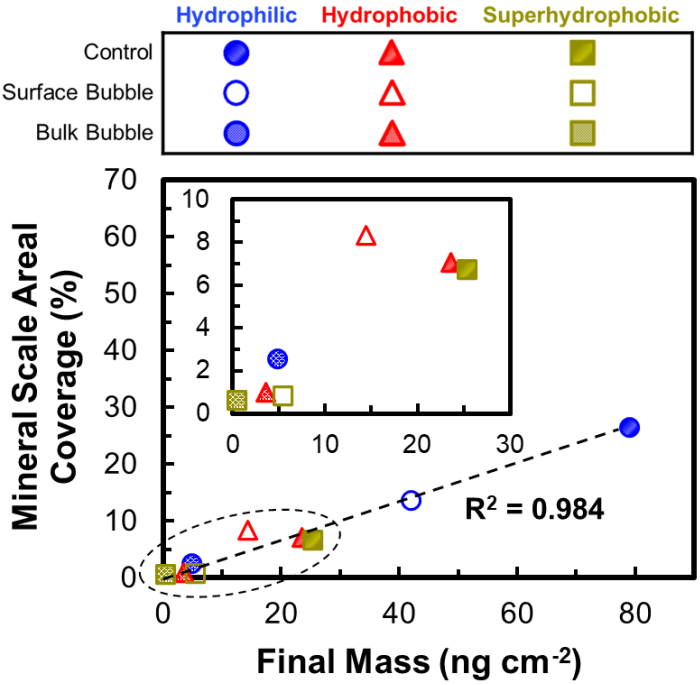


**Figure 2. 10.** Percentage of total area covered by mineral crystals measured from SEM-EDX images in **Figure 2.9D** using particle size analysis in ImageJ software versus the final crystal mass deposited on the surface according to measured frequency response with QCM-D in **Figure 2.9A-C**. Inset shows the highlighted region in the low final mass/areal coverage range. Legend above matches each symbol with their experimental ID and surface wetting properties. The correlation ($R^2$) calculated between mineral scale areal coverage measured from SEM-EDX images and final mass measured from QCM-D data for all experiments is displayed with linear trendline.

### 2.4. Conclusions and Implications

From this study we can draw four main conclusions. (1) Regardless of surface wetting properties, the scaling resistance induced by the solvent exchanges followed bulk bubble > surface bubble > no bubble (control). Higher degree of interfacial bubble formation reduces the direct liquid-solid contact for mineral crystal deposition; (2) When solution conditions are conducive to surface or bulk bubble formation, i.e., not degassed, the scaling resistance of the surfaces follows superhydrophobic > hydrophobic > hydrophilic. This is because increasing hydrophobicity promotes interfacial gas layer stability on submerged surfaces; (3) In the absence of interfacial gas layers, scaling resistance decreases with increasing surface energy; and (4) Incorporation of bulk nanobubbles into a scale-prone solution can improve the scaling resistance of any surface

regardless of wetting properties. Furthermore, incorporation of bulk nanobubbles into a scale-prone solution in contact with a superhydrophobic surface virtually eliminates mineral scaling as bulk bubbles coalesce into the entrained gas layer of the superhydrophobic surface and maintain its long-term stability. Bulk nanobubbles may also stabilize a suspension of bulk precipitated mineral crystals via a flotation effect, leading to further enhancement in scaling resistance regardless of surface properties [123,124].

Implications from these findings may help to optimize the combination of surface wetting properties and operating conditions for membrane processes, heat exchangers, and marine structures that are prone to mineral scaling. For example, intermittent solvent exchanges or other operational techniques that promote surface nanobubble nucleation, such as surface localized temperature changes, may help to prolong the scaling resistance of the surface. While the best scaling resistance can be realized with a superhydrophobic surface, the stability of the Cassie-Baxter state directly relates to the lifetime of the surface's scaling mitigation capabilities. As such, the use of degassed solutions, where the driving force for the entrapped gas layer to dissolve into solution is high, should be avoided. In the best case, regardless of the surface wetting property requirements, mineral scaling can be avoided by aerating with an inert gas such as nitrogen. The presence of bulk bubbles not only prolongs and enhances the surface coverage of adsorbed and nucleated surface bubbles but exhibits antifouling effects in the bulk via a floatation mechanism.

**Acknowledgement:** This material is based upon work supported by the National Alliance for Water Innovation (NAWI), funded by the U.S. Department of Energy, Office of Energy Efficiency and Renewable Energy (EERE), Advanced Manufacturing Office, under Funding Opportunity Announcement Number DE- FOA-0001905.

# CHAPTER 3: MEMBRANE WETTING PROPERTIES AND THEIR ROLE IN ORGANIC FOULING OF MEMBRANE DISTILLATION MEMBRANES

This chapter has been published in the journal Chemical Engineering Journal Advances as the following peer-reviewed manuscript: **Horseman, T.**, Wang, Z., and Lin, S., Colloidal interactions between model foulants and engineered surfaces: Interplay between roughness and surface energy. Chemical Engineering Journal Advances **8** (2021). P. 100138. doi: 10.1016/j.ceja.2021.100138.

## 3.1. Introduction

Fouling is a phenomenon that may potentially occur where colloids and organics adsorb to submerged surfaces such as membranes, marine structures, and heat exchangers. Membrane fouling is detrimental as the adsorption of foulants blocks membrane pores, compromising membrane performance and significantly increasing operating costs [30,125,126]. Heat exchanger fouling is detrimental as the adsorption of foulants adds heat transfer resistance between the two working streams [127,128]. Additionally, fouling on submerged marine surfaces, such as ship vessel hulls, may lead to inferior hydrodynamics, reducing fuel efficiency and increasing overall maintenance costs [129–131]. Because fouling is a major limiting factor for practical applications of membrane technologies, heat exchangers, and marine vessels, the mechanisms and mitigation thereof have been extensively studied [45,50,132–139].

Previous studies have investigated the specific behavior of common foulants, including natural organic matters (NOMs), oils, and inorganic colloidal particles [140–145]. Experiments have been performed to elucidate the influence of surface properties, including charge, pore size, and roughness (texture), on the fouling mechanisms in membrane processes [146–152]. However, the effect of surface roughness on fouling in membrane separations is debated. For example, the kinetics of colloidal fouling on reverse osmosis (RO) and nanofiltration (NF) membranes has been shown to positively correlate with membrane surface roughness [153–155]. On the other hand, several studies claim that surface roughness improves the fouling resistance of the membrane by reducing the interaction between foulants and the membrane surface [156–159]. Likewise, there is also debate on the effect of surface roughness and wettability on fouling of vapor-gap membranes (i.e., water does not transport through the membrane in liquid form) such as those used in membrane distillation (MD) and membrane contactors (e.g. for ammonia or methane recovery). For example, humic acid fouling has shown to decrease with increasing hydrophobicity (increased roughness and decreased surface energy) [160–163], while oil fouling can be mitigated altogether

by increasing membrane hydrophilicity (increased roughness and surface energy) [164–167]. On the other hand, studies claim that increasing hydrophobicity may slightly increase humic acid fouling [168,169] and oil fouling can be mitigated by increasing membrane hydrophobicity [162].

For marine structures, such as ship vessel hulls, and heat exchangers, particularly those used for seawater cooling and in the food & beverage industry, biofouling is particularly common. Formation of a biofouling layer is predated by the adsorption of soft matter such as bacteria, NOMs, proteins, and oils that serve as precursors for additional foulant attachment [45,170,171]. As such, the fouling behaviors of these species and the surface properties that influence the kinetics and strength of their attachment have been extensively studied in these fields [129,172]. However, there is no consensus on the effect of surface roughness and wetting property on the specific fouling behavior of certain organic foulants such as oils, humic substances, or bacteria. For example, increased surface roughness has shown to increase surface area for foulant attachment and increase foulant adhesion for marine vessels or heat exchange surfaces [172–175], while other studies suggest that increased surface roughness may inhibit strong organic foulant attachment depending on the length scale of the surface texture features [176,177]. Likewise, increased surface hydrophobicity (increased roughness and decreased surface energy) has shown to limit organic foulant surface density [178,179], while other studies claim smooth, hydrophobic (low surface energy), surfaces lead to less fouling [180] or that low surface energy surfaces alone (regardless of roughness) mitigate foulant deposition and attachment [181].

To date, no systematic and comprehensive study has been performed to elucidate the combined effect of texture and surface energy on submerged surface fouling. The objective of this study is to systematically investigate the interactions between colloidal probes that mimic representative foulants and model substrates with different morphologies and surface energies, aiming to provide insights for designing fouling-resistant surfaces. To achieve this goal, we constructed smooth and textured silicon dioxide surfaces then grafted them with poly(ethylene glycol) (PEG) and a fluoroalkylsilane (FAS), to obtain smooth and textured hydrophilic and hydrophobic surfaces, respectively. We characterized the surfaces in terms of surface morphology and wetting properties, then performed atomic force microscopy (AFM) force spectroscopy measurements in water with a hydrophilic carboxylate coated polystyrene (C-PS) colloidal probe and a hydrophobic polyethylene (PE) colloidal probe. The maximum adhesion forces and rupture distances between the colloidal probes and surfaces are analyzed to extract insights for developing a framework for

fabricating robust fouling resistant surfaces. We note that the study is not intended to focus a specific application, but rather to provide broadly applicable understanding of the dependence of fouling propensity on foulant and surface properties.

## 3.2. Materials and Methods

### *3.2.1. Fabrication of surfaces with roughness*

Quartz microscope slides (VWR, Radnor, PA) were utilized in this study as the substrate subject to surface modification. To obtain textured surfaces, the slides were rinsed with DI water, followed by sonication, first in ethanol, and then in DI water, each for 10 minutes. After being dried in air, the slides were immersed in an aqueous dispersion of silica nanoparticles (SiNPs, diameter ~ 200 μm), synthesized using Stöber method [182], with 30 minutes of sonication. Upon complete evaporation of water in the aqueous solution, slides with surface coated with multiple layers of SiNPs were obtained. The SiNPs-coated slides were then heated at 600 ºC for 1 hour and purged with pressurized air to remove unassociated impurities. These surfaces were used as the model rough surfaces for further modification.

### *3.2.2. Functionalization of surfaces to impart different surface energies*

Intrinsic hydrophilicity was imparted to both the smooth and textured surfaces via grafting of poly(ethylene glycol) (PEG) using silane chemistry. Before PEG-grafting, each slide was cleaned by sonication in ethanol and then DI water, each for 10 minutes, followed by room temperature drying in air, and lastly 5 minutes of ozone plasma treatment. The cleaned slide was then submerged in a toluene solution with 10 mM HCl and 1 mM 2-[Methoxypoly-(ethyleneoxy)-propyl]trimethoxylsilane (Gelest, Morrisville, PA) for 19 hours at room temperature. The modified slides were then rinsed with toluene, ethanol, and DI water, respectively, and dried in an oven at 80 °C for 5 minutes [183].

Surface hydrophobicity was imparted to both smooth and textured substrates with surface grafting of fluoroalkylsilane (FAS). Similar to grafting of PEG, each slide was sonicated in ethanol and water then treated by ozone plasma. After plasma treatment, the slide and 150 μL of FAS (1H, 1H, 2H, 2H-perfluorodecyltriethoxysilane, Sigma Aldrich, St. Louis, MO) were placed in a Petri dish. The covered Petri dish with the slide and FAS was placed in a vacuum oven at 90 °C for 24 hours for vapor deposition. The modified slides were then heated at 80 °C in air for 3 hours [184].

*3.2.3. Characterizations of morphology and wetting property*

The surface morphology of the smooth and textured model surfaces was observed using both scanning electron microscopy (5 kV, HE-SE2 secondary electron detector, SEM, Merlin, Zeiss, Thornwood, NY), and AFM-based force spectroscopy (ScanAsyst mode, Dimension Icon, Bruker, Billerica, MA). The static liquid contact angles (CAs) of the surfaces were measured with water in air and with mineral oil underwater. All CAs were measured with an optical tensiometer (TL100, Attension, Finland). The in-air CA measurements were performed using sessile drop method, while the underwater oil CA measurements were conducted following captive bubble method with the air bubble replaced by a mineral oil droplet. For each sample, the CAs were measured at five different locations on the surface and averaged with standard deviation reported.

*3.2.4. Colloidal probe force spectroscopy*

Force spectroscopy was used to measure the interfacial forces between functionalized colloidal probes (Novascan, Ames, IA) and model surfaces using an AFM (**Figure 3.1**). Two different types of colloidal probes were used, including polyethylene (PE) colloidal probe and polystyrene colloidal probe functionalized with carboxyl groups (C-PS). The PE probe is made of a soft and hydrophobic PE colloidal particle that mimics the behavior of deformable hydrophobic colloidal foulants (e.g. oil droplets and proteins), while the C-PS probe has been used to study the fouling by organic matter that is typically rich in carboxyl groups (e.g. humic acid and algae) [152,185–188]. The diameters for the PE probe and C-PS probe were 5 μm and 4.5 μm, respectively. Force measurements were conducted in 10 mM aqueous solution of NaCl following previous studies [154,189–191]. Other solution chemistries could be used, which would mostly affect the electrical double layer (EDL) interaction. The effects of electrolyte type and concentrations on particle-surface interaction has been extensively studied and well understood [192–194], and thus would not be the focus of this investigation. The trigger force, ramp size, and ramp rate were 5 nN, 2.5 μm, and 1 Hz, respectively. The raw force data was collected by the AFM during the extension (approaching) and retraction regimes of the experiment. For each sample, force spectroscopy was conducted at 300 different positions within a 25 $\mu m^2$ area near the center of the surface to obtain interaction force curves that were analyzed using NanoScope Analysis 1.5.

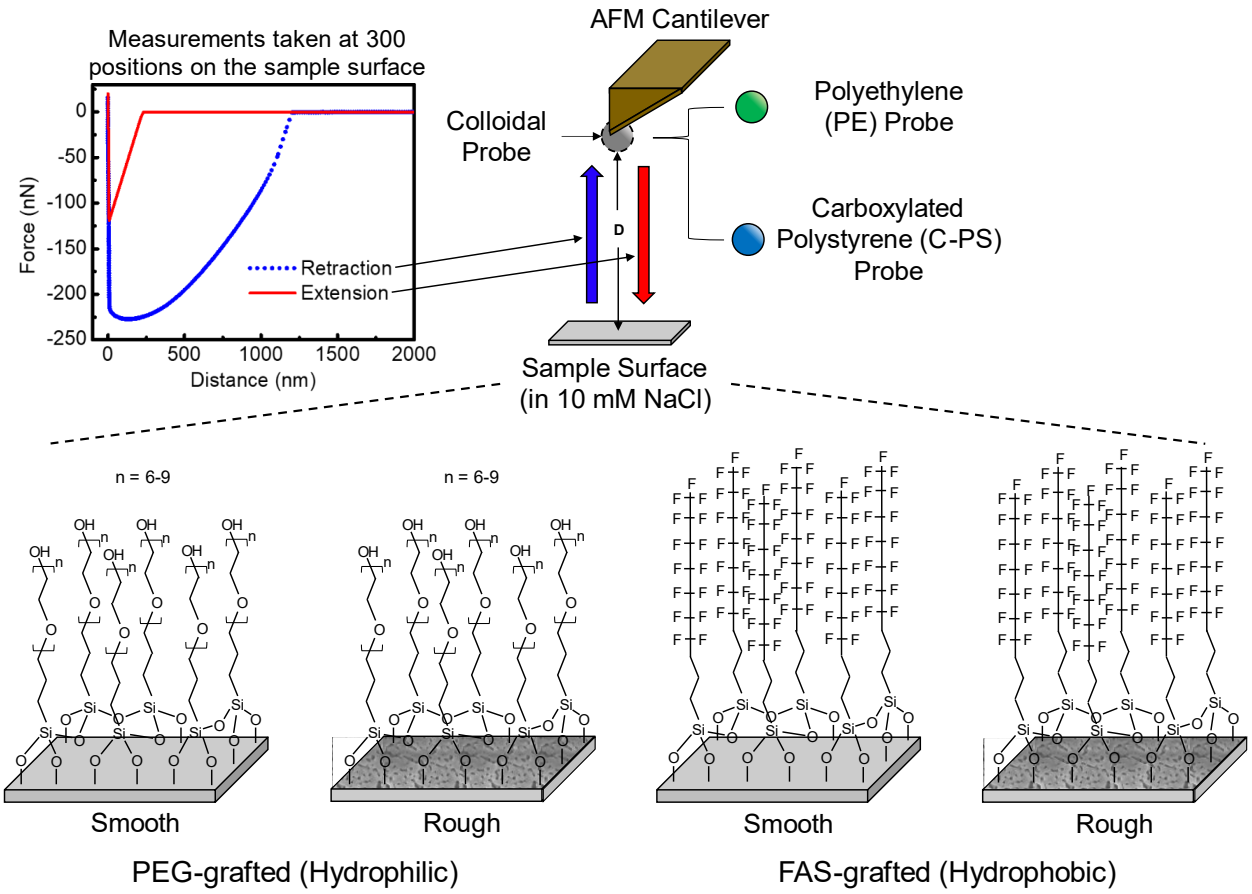


**Figure 3. 1.** Schematic diagram showing AFM-based colloidal probe force spectroscopy, featuring representative extension curve (red) and retraction curve (blue). Two colloidal probes were used: a polyethylene (PE) probe that mimics a soft hydrophobic colloidal foulant such as an oil droplet and a carboxylated polystyrene (C-PS) probe with the carboxyl groups representing moieties commonly found in natural organic matter. Model surfaces consisted of hydrophilic poly(ethylene glycol) (PEG) grafted surfaces and hydrophobic fluoroalkylsilane (FAS) grafted surfaces, each with a smooth version and rough version textured with silica nanoparticles. All measurements were conducted with sample surface and colloidal probe immersed in 10 mM aqueous solution of NaCl.

## 3.3. Results and Discussion

### *3.3.1. Morphologies of the surfaces*

The morphology of smooth and textured surfaces are drastically different (**Figure 3.2A & 3.2B**, respectively). Specifically, the presence of SiNPs renders the modified surface significantly rougher than the pristine surface without SiNPs. The deposited SiNPs multi-layer coalesced upon sintering at 600 °C and formed a continuous surface with texture (**Figure 3.2B**). Such a sintering effect also immobilizes the SiNPs so that they do not detach from the surface or move laterally as the colloidal probe interacts with the surface in the force spectroscopy experiments.

The surface morphology of the smooth and textured surfaces was also measured via AFM (**Figure 3.2C and 3.2D**, respectively). Similar to the SEM images, the AFM images show that the surface deposited with SiNPs (**Figure 3.2D**) is much rougher than the bare, smooth surface (**Figure 3.2C**). Specifically, the measured average roughness ($R_a$) and root mean square roughness ($R_q$) of the rough surface are 62.2 and 79.7 nm, respectively, nearly, two orders of magnitude larger than those of the smooth surface ($R_a$ = 0.8 nm , $R_q$= 1.0 nm).

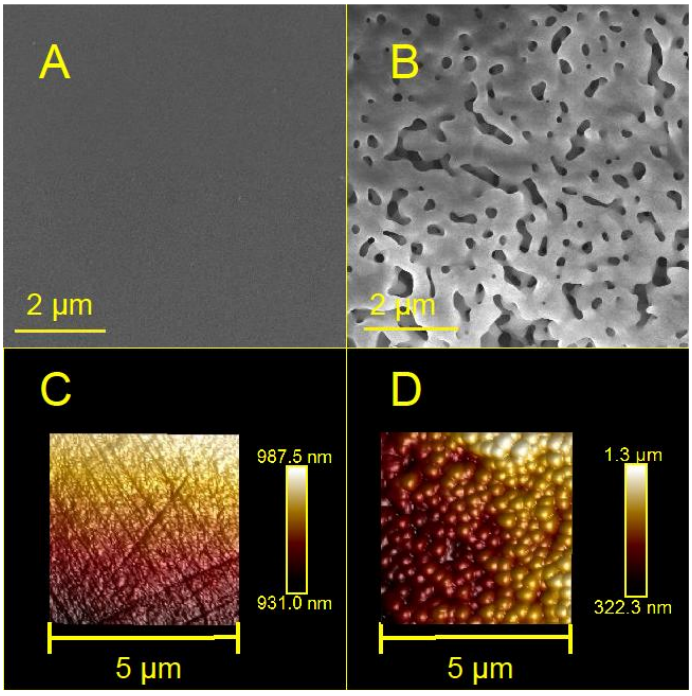


**Figure 3. 2.** SEM images of the surfaces of (A) the smooth, pristine, microscope slide and (B) the rough, SiNPs surface multi-layer, slide. The corresponding AFM images of the surfaces (C) the smooth, pristine, slide and (D) the rough SiNPs surface coated slide.

*3.3.2. Wetting properties of the smooth and rough surfaces*

The PEG-grafted smooth surface has an in-air water CA of 38.0 ± 0.3° (**Figure 3.3**). In comparison, the in-air water CA of the PEG-grafted rough surface was not detectable, suggesting the surface was rendered superhydrophilic. The CA reduction of a PEG-grafted surface by increasing surface roughness can be explained via Wenzel's theory [195]: if the roughness ratio of the surface, defined as the ratio of actual surface area over the projected surface area, is *r*, the apparent CA of a rough surface, $\theta_A$, deviates from the intrinsic CA of a smooth surface with the same surface tension, $\theta_0$, following the equation below [196]:

$$\cos\theta_A = r\cos\theta_0 \tag{3.1}$$

The Wenzel's theory suggests that increasing surface roughness will amplify the hydrophilicity of an intrinsically hydrophilic surface and render the surface superhydrophilic.

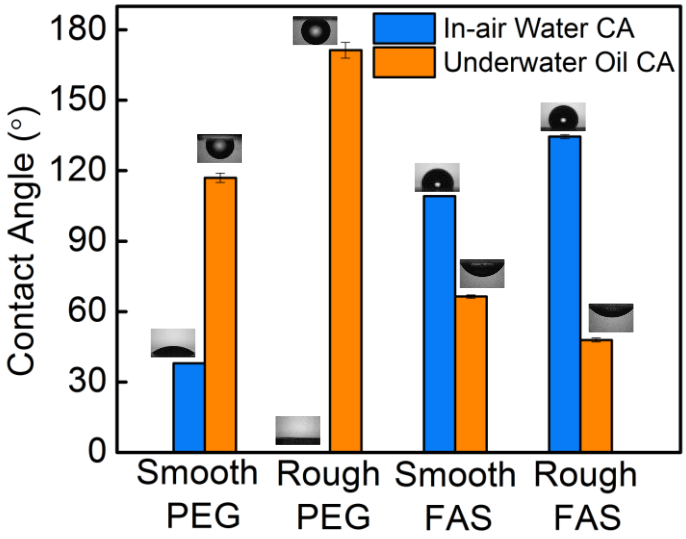


**Figure 3. 3.** (Blue) In-air water contact angles of the smooth PEG grafted surface, the rough PEG grafted surface, the smooth FAS deposited surface, and the rough FAS deposited surface. In-air water contact angle images displayed above each respective contact angle value. (Orange) Underwater oil contact angles of the smooth PEG grafted surface, the rough PEG grafted surface, the smooth FAS deposited surface, and the rough FAS deposited surface. Underwater oil contact angle images displayed above each respective contact angle value.

For the FAS-grafted surfaces, the in-air water CAs of the smooth and rough surfaces were 109.2 ± 0.2° and 134.5 ± 0.8° (**Figure 3.3**), respectively. The introduction of roughness to the surface enhanced the apparent CA of the hydrophobic surface. However, due to the roughness imparted on the rough FAS-grafted surface, the water droplet exists in a Cassie-Baxter state, where the droplet is supported by not only the FAS-grafted surface, but also air pockets within the surface roughness features [118,119]. In a Cassie-Baxter state, the apparent CA, $\theta_A$, relates to the intrinsic CA, $\theta_0$, by the following equation:

$$\cos\theta_A = f(\cos\theta_0 + 1) - 1 \tag{3.2}$$

where $f$ is the areal fraction of water-solid contact and thus $(1 - f)$ is the areal fraction of water-air contact. If we assume the roughness on the FAS-grafted silica surface without SiNPs deposition to be negligible, then $\theta_0$ is 109.2 ± 0.2° and $f$ is calculated to be ~0.54.

The FAS-grafted rough surface, with a CA of 134.5 ± 0.8°, is not qualified as a superhydrophobic surface which typically requires an apparent CA higher than 150°. In previous studies using surfaces modified with fluorinated SiNPs, superhydrophobicity can be readily achieved [64,197–202]. Here, sintering SiNPs changed the morphology of deposited SiNPs layer,

smoothing the interconnections between SiNPs, and consequently reducing $f$ and reducing the mean curvature of the "surface protrusions". We choose to use such a sintered surface for adhesion force measurement even though it is not superhydrophobic, as we want to prevent, to the greatest extent possible, the potential lateral movement or detachment of SiNPs during the adhesion force measurements. The key feature of the rough surface we want to achieve for comparison with a smooth surface is not a super-high apparent CA, but rather the presence of air pockets that lead to Cassie-Baxter contact between the textured hydrophobic surface and a hydrophobic colloidal probe.

The underwater CAs measured with mineral oil are also presented in **Figure 3.3**. The PEG-grafted smooth surface, which is in-air hydrophilic, is underwater oleophobic with an underwater oil CA of 117.0 ± 2.0°. The PEG-grafted rough surface, which is in-air superhydrophilic, is underwater superoleophobic with an ultrahigh underwater oil CA of 171.3 ± 3.3°. The oleophobicity (or superoleophobicity) of the PEG-grafted surface is attributable to the hydration force [193,203,204]: for an oil droplet to spread over the PEG-grafted surfaces, the hydrophilic (or superhydrophilic) surfaces have to first be dehydrated. The dehydration of a highly hydrophilic surface submerged in water is thermodynamically unfavorable. In comparison, the FAS-grafted smooth and rough surfaces are both underwater oleophilic due to the attractive hydrophobic-hydrophobic interaction between the oil droplet and the FAS-grafted surface [121,205–207]. The surface roughness enhanced the underwater oleophilicity of the FAS-grafted surface, reducing the underwater oil CA from 66.4 ± 0.7° to 47.9 ± 0.8°. Assuming the system to be in a Cassie-Baxter state (which is consistent with previous experimental observation [30]), $f$ is calculated to be 0.55, very close to the $f$ value estimated using in-air water CA.

### *3.3.3. Colloidal Probe Force Spectroscopy*
### *3.3.4. Adhesions between the colloids and the surfaces*

The discussion in Section 3.3.3 is based primarily on representative force curves, each chosen from hundreds of repetitive force measurements at different locations on the model surface. The retraction regime of each force curve yields two key characteristic parameters, the maximum adhesion force, and the rupture distance. The maximum adhesion force is the maximum force measured while retracting the colloidal probe from the substrate surface. This adhesion force is directly related to the net adhesion energy ($W_{PS}$) between the probe ($P$) and substrate ($S$). In the three-phase system consisting of water ($L$), substrate, and probe, the balance of interfacial energies

($\gamma_{ij}$) and contact-area between the probe and substrate ($A_{PS}$) tends to an energy minimum according to:

$$W_{PS} = A_{PS}(\gamma_{SL} + \gamma_{PL} - \gamma_{PS}) \quad (3.3)$$

Rupture distance is the maximum distance where the interaction between the colloidal probe and the substrate surface is no longer present [226,227]. Strong attractive interactions between the colloidal probes and the substrate surfaces generate larger maximum adhesion forces and larger rupture distances, and vice versa. For each probe-substrate surface pairing, the force curves were measured at 300 locations on the surface, and the distributions of maximum adhesion force and rupture distance were calculated for each pairing (**Figure 3.5**). The mean maximum adhesion forces and mean rupture distances are summarized in **Table 3.1**.

**Table 3. 1.** Adhesion force statistics of the polyethylene (PE) and carboxylate coated polystyrene (C-PS) colloidal probes interacting with the smooth and rough hydrophilic PEG-grafted surfaces and smooth and rough hydrophobic FAS-grafted surfaces.

| **Probe** | **Surface Type** | | **Maximum Adhesive Force (nN)** | **Rupture Distance (nm)** |
|---|---|---|---|---|
| PE | PEG (Hydrophilic) | Smooth | 18 ± 4 | 283 ± 56 |
| | | Rough | 3 ± 2 | 75 ± 41 |
| C-PS | | Smooth | 4.1 ± 0.3 | 43 ± 4 |
| | | Rough | 0.7 ± 0.4 | 26 ± 11 |
| PE | FAS (Hydrophobic) | Smooth | 346 ± 35 | 1157 ± 160 |
| | | Rough | 440 ± 31 | 2036 ± 198 |
| C-PS | | Smooth | 93 ± 45 | 163 ± 38 |
| | | Rough | 241 ± 30 | 1374 ± 142 |

For the interactions between colloidal probes and hydrophilic surfaces (**Figure 3.5A, 3.5B, 3.5E, and 3.5F**), the adhesion force is substantially weaker, and the rupture distance is significantly shorter as compared to the interaction with hydrophobic surfaces (**Figure 3.5C, 3.5D, 3.5G, and 3.5H**). With the same colloidal probe, the maximum adhesion forces and rupture distances measured with the rough hydrophilic surfaces (**Figure 3.5B and 3.5F**) are considerably less than those measured with the smooth hydrophilic surfaces (**Figure 3.5A and 3.5E**). The hydrophilic surfaces favor contact with water (i.e. surface hydration, $\gamma_{PL} < \gamma_{PS}$ and $\gamma_{SL} < \gamma_{PS}$), so retracting the colloidal probe from the surface and replacing the area $A_{PS}$ with the substrate-water interface, minimizes the net interfacial energy of the three-phase system [193]. According

to **Equation 3. 3**, $\gamma_{SL}$, $\gamma_{PL}$, and $\gamma_{PS}$ are identical for the rough and smooth hydrophilic surfaces in contact with the same colloidal probe. Because the interfacial area, $A_{PS}$, between the probe and rough hydrophilic surface is less than that with the smooth hydrophilic surface, there is less net adhesive energy, and thus lower max adhesion force that must be overcome to remove the probe from the surface. Likewise, with the same morphology of the hydrophilic surfaces, the maximum adhesion forces measured with the C-PS colloidal probe is smaller than that measured with the PE colloidal probe. This is likely caused by two reasons. Firstly, the PE probe is slightly larger (5 μm diameter) and softer (Young's Modulus ~ 500 MPa) than the C-PS probe (4.5 μm diameter and Young's Modulus ~ 3,000 MPa), meaning the interfacial area between the PE probe and substrate ($A_{PS}$ in **Equation 3.3**) is always greater than that of the C-PS probe for the same surface, resulting in lower maximum adhesive force [193]. Secondly, is the higher degree of hydration of the C-PS probe as compared with the PE probe ($\gamma_{PL,C-PS} < \gamma_{PL,PE}$), caused by the negatively charged carboxyl groups on the C-PS probe that form hydrogen bonds with water. The hydration of the C-PS probe renders its contact with the hydrophilic substrate energetically unfavorable as it increases the net interfacial energy, and its detachment from the hydrophilic substrate energetically highly favorable.

In general, strong adhesive forces and large rupture distances were observed with rough hydrophobic (FAS-coated) surface regardless of type of colloidal probe (**Figure 3.5D and 3.5H**). These strong and long-ranged interactions are attributable to the capillary interaction between the particles and the air-film anchored to the textured hydrophobic surface in the Cassie-Baxter state [206,211,215–217,228]. In particular, the interaction was the strongest between the textured hydrophobic surface and the hydrophobic PE probe (**Figure 3.5D**). However, surface texture is not a pre-requisite for strong and long-ranged attractive interaction which has also been observed between the hydrophobic PE probe and the smooth hydrophobic surface due to the hydrophobic-hydrophobic interaction (**Figure 3.5C**). Specifically, the retraction of the PE colloidal probe from the hydrophobic surface would increase the interfacial area between water and the hydrophobic surfaces and reduce the overall interfacial entropy of the system, rendering a thermodynamically unfavorable state [193]. Such an effect is considerably smaller for interaction between a smooth hydrophobic surface and a C-PS probe that is less hydrophobic than the PE probe (**Figure 3.5G**). The comparison of the average maximum adhesion forces between these different scenarios is also summarized in **Figure 3.6**.

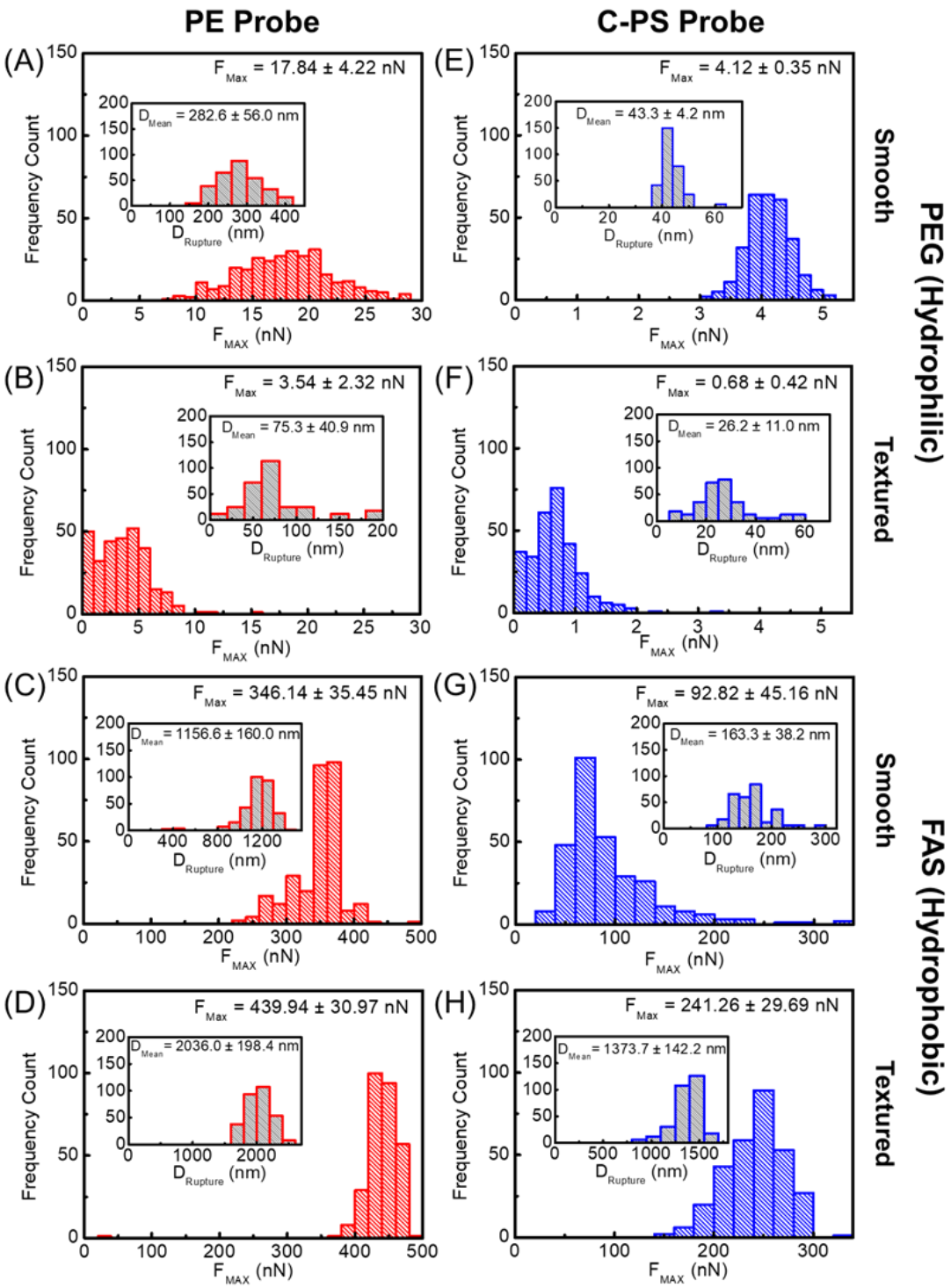


**Figure 3. 5.** Distributions of max adhesion force ($F_{Max}$) and rupture distances ($D_{Rupture}$, insets) measured at 300 different positions on the sample surfaces. Adhesion statistics of polyethylene (PE) colloidal probe interacting with (A) the smooth hydrophilic surface, (B) the rough hydrophilic surface, (C) the smooth hydrophobic surface, and (D) the rough hydrophobic surface, respectively. Adhesion statistics of carboxylated polystyrene (C-PS) colloidal probe interacting with (E) the smooth hydrophilic surface, (F) the rough hydrophilic surface, (G) the smooth hydrophobic surface, and (H) the rough hydrophobic surface, respectively.

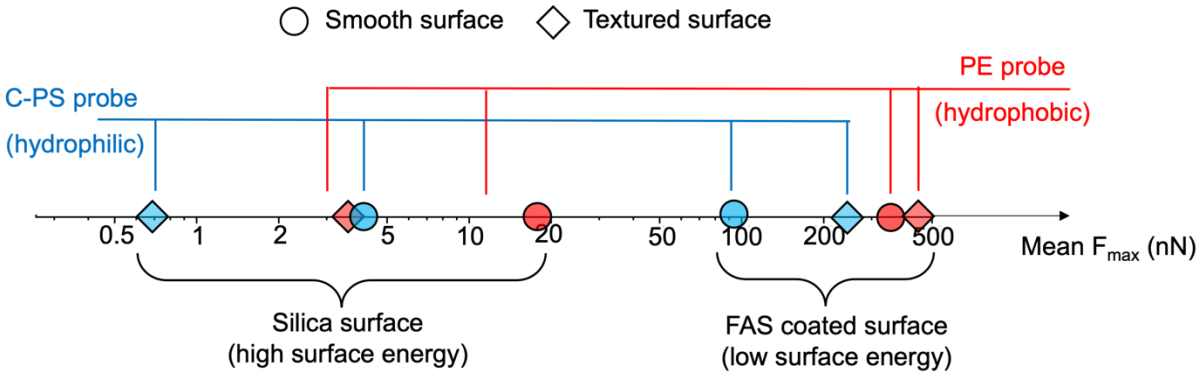


**Figure 3. 6.** Comparison between the mean values of maximum adhesion force for different interactions based on data presented in **Figure 3.5**. The axis is in log scale.

## 3.4 CONCLUSIONS

Using AFM force spectroscopy, we elucidate the role of surface texture and surface energy on the interaction between model foulants and surfaces with different morphology and surface energy. We found that: (1) submerged hydrophilic surfaces are generally less prone to fouling than is a submerged hydrophobic surface, which is relatively well known; (2) compared to a smooth hydrophobic surface, a rough hydrophobic surface increases not only the strength but also the characteristic length of the attractive interaction; and (3) compared to a smooth hydrophilic surface, a rough hydrophilic surface reduces not only the strength but also the characteristic length of the attractive interaction. In other words, the surface roughness/texture amplifies the intrinsic interaction between the foulants and a substrate surface, which is similar to how it amplifies the surface wetting properties.

The implications gleaned from this study provide significant insight for fabrication of anti-fouling surfaces used membrane separations, heat exchangers, and marine structures. In general, mitigation of organic fouling, should it be oil or natural organic matter, prefers super-hydrophilic surfaces characterized by high surface energy and large roughness. If hydrophobic materials must be used for specific processes, the presence of surface roughness (texture) would result in strong adhesion of hydrophobic foulants due to capillarity, which is unfavorable for mitigating organic fouling. We note that such suggestions apply specifically to organic fouling and that the mitigation of mineral scaling may follow completely different rules.

**Acknowledgements:** The authors acknowledge the support from American Chemical Society Petroleum Research Foundation via award ACS-PRF 57353 DNI and from National Science Foundation via award 1705048.

# CHAPTER 4: ENHANCE FOULING RESISTANCE OF MEMBRANE DISTILLATION MEMBRANES VIA A NOVEL OPERATIONAL-MATERIAL APPROACH

This chapter has been published in the journal Environmental Science & Technology Letters as the following peer-reviewed manuscript: **Horseman, T.**, Su, C., Christie, K. S., & Lin, S. Highly effective scaling mitigation in membrane distillation using a superhydrophobic membrane with gas purging. Environmental Science & Technology Letters, **6**(7), (2019). 423-429. doi: 10.1021/acs.estlett.9b00354.

## 4.1. Introduction

Membrane distillation (MD) is a thermal desalination process in which water evaporation and condensation occur within the pores of a microporous hydrophobic membrane [14]. As a desalination process that can harness low-grade waste heat to treat hypersaline brine, MD has been actively explored as a promising technology for brine management in produced water treatment and zero liquid discharge (ZLD) [5,229–232]. Managing hypersaline brine is a critical environmental challenge, especially because reverse osmosis (RO), the state-of-the-art desalination technology, cannot be applied in these scenarios in which the brine osmotic pressure exceeds the current allowable working pressure of RO [233–236]. In comparison, the performance of MD as a thermal distillation process is relatively independent of brine salinity, which in theory allows MD to achieve a high degree of brine volume reduction or even brine crystallization [237,238]. The major and inevitable challenge for such an application, however, is membrane scaling, i.e., the formation or deposition of mineral crystals on the membrane surface that ultimately leads to complete process failure [14,230].

Scaling is detrimental to MD performance because crystals may (1) block membrane pores, which reduces membrane permeability for vapor transfer, and (2) grow through the pores, allowing the salty feed solution to pass directly through the membrane and contaminate the distillate (i.e., wetting) [239]. The mode of crystal growth during scaling is mixed. Some crystals are nucleated homogeneously or heterogeneously from seeds in the bulk solution and deposited onto the membrane surface, while other crystals may nucleate heterogeneously directly on the membrane surface and grow in situ (i.e., interfacial crystallization) [19,240]. Interfacial crystallization is more problematic because it may lead to a larger contact area and thus stronger overall crystal−polymer interaction [241,242]. This also allows crystals to mold to the geometry of the membrane pore structure and further enhance the crystal−membrane interaction. In contrast, large crystals that

form in the bulk solution and deposit on the membrane surface have weaker interactions and a smaller contact area with the membrane surface [243].

Classical nucleation theory suggests that heterogeneous crystallization on surfaces with the right interfacial properties is favored over homogeneous crystallization [244]. With that, increasing membrane hydrophobicity has been shown to discourage interfacial crystallization and reduce the overall scaling kinetics [66,198,245–248]. However, only delaying scaling is insufficient for the practical application of MD in treating hypersaline brine if scaling is irreversible. Previous MD studies have also investigated gas purging or blowing compressed air through the membrane pores from the distillate to the feed side, for scale mitigation [249,250]. These studies showed that purging was effective only when the initial feed concentration was well above saturation so that most of the crystals formed in the bulk solution and deposited on the membrane surface. With the initial feed concentration below saturation, mineral crystals form within the membrane pores and become "anchor points" for the scale layer, which significantly compromises the effectiveness of purging [198].

With conventional hydrophobic membranes, the feed solution partially intrudes into the membrane pores, as the hydraulic pressure of the circulating feed stream exceeds the liquid entry pressure of some pores near the membrane surface [66,198,248]. Such partial intrusion increases the solid−water contact area available for interfacial heterogeneous crystallization and promotes the in-pore formation of mineral crystal "anchors" that lead to a robust scale layer that cannot be removed by purging (**Figure 4.1A**). We hypothesize that the use of a superhydrophobic membrane, which significantly reduces the solid−water contact area, will minimize in-pore crystal formation and the adhesion of the crystal to the membrane surface, thereby making purging significantly more effective in maintaining membrane performance by removing the deposited salt crystals (**Figure 4.1B**).

In this study, we test the hypothesis described above by comparing the effectiveness of purging in maintaining the performance of hydrophobic and superhydrophobic membranes subject to gypsum scaling. We first fabricate a superhydrophobic membrane by modifying the surface of a commercial polyvinylidene fluoride (PVDF) membrane using silica nanoparticles (SiNPs) coated with fluoroalkylsilane (FAS). We then perform MD experiments using the hydrophobic and superhydrophobic membranes with an undersaturated gypsum feed solution to compare the scaling

kinetics with and without periodic purging. Finally, we also examine the morphology of the scaled membrane to elucidate the difference in the effectiveness between different scaling mitigation strategies.

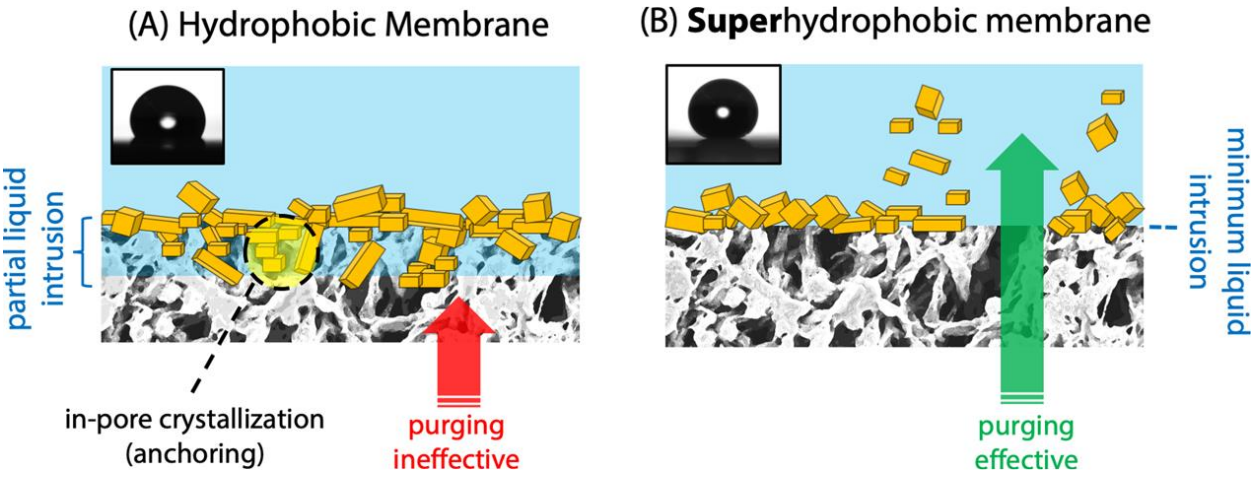


**Figure 4. 1.** Schematic illustration of the central hypothesis in this study. (A) With a conventional hydrophobic membrane, the feed solution partially wets the pores near the membrane surface, resulting in in-pore growth of gypsum crystals. Consequently, gas purging is ineffective in removing the crystal due to stronger adhesion and physical anchoring. (B) With a superhydrophobic membrane, intrusion of the feed solution and thus in-pore growth of the crystal are minimized, which renders gas purging highly effective in removing the crystals deposited on the membrane surface.

## 4.2. Materials and Methods

### *4.2.1. Materials and Chemicals*

The commercial hydrophobic PVDF membranes with a 0.45 μm nominal pore size were purchased from GE Healthcare (Pittsburgh, PA). Sodium hydroxide (NaOH), 200 proof ethanol, 3-aminopropyltriethoxysilane (APTES, 99%), trizma-hydrochloride buffer, LUDOX HS-40 colloidal silica (SiNPs) with a diameter of 12 nm, hydrochloric acid (HCl), calcium chloride ($CaCl_2$), sodium sulfate ($Na_2SO_4$), and 1H,1H,2H,2H-perfluorodecyltriethoxysilane (fluoroalkylsilane, or FAS, 97%) were purchased from Sigma-Aldrich (St. Louis, MO). Silica nanoparticles (SiNPs) with a diameter of 40−60 nm were purchased from SkySpring Nanomaterials (Houston, TX).

### *4.2.2. Fabrication of a Superhydrophobic Membrane*

The superhydrophobic membrane was obtained by modifying the commercial PVDF membrane using FAS-coated SiNPs similar to the approach reported by Boo et al [184]. First, a pristine commercial PVDF membrane surface was placed on a 7.5 M NaOH solution for 3−4 h at

70°C. Due to the hydrophobicity, the PVDF membrane floated on the solution, which chemically modified only the membrane surface in contact with the NaOH solution to generate an abundance of surface hydroxyl groups. The treated membrane was then rinsed thoroughly with deionized (DI) water and dried for 1.5 h at 70°C. The membrane surface was then immersed in 1 vol % APTES (in ethanol) for 1 h under gentle mixing. SiNPs with a diameter of 40−60 nm were then dispersed at 1 wt % in 10 mM trizma hydrochloride with the pH adjusted to 4 at which point the APTES-functionalized surface is positively charged and the SiNPs are negatively charged. The APTES-functionalized surface of the PVDF membrane was placed in contact with the SiNP dispersion for adsorption of SiNPs to the surface via electrostatic interaction. As only the surface of the membrane was functionalized, the bulk of the membrane maintained its hydrophobicity and thus floated on the SiNP dispersion, adding SiNPs only to the surface. The SiNP-coated surface was rinsed with DI water and dried. Such a functionalization and adsorption process was repeated with 12 nm diameter SiNPs (i.e., applying the exact same procedure to the PVDF membrane coated with 40−60 nm diameter SiNPs). Finally, the SiNP-coated membrane surface was silanized with FAS via vapor phase reaction at 80 °C overnight. The surface modification process is schematically illustrated in **Figure 4.2.**

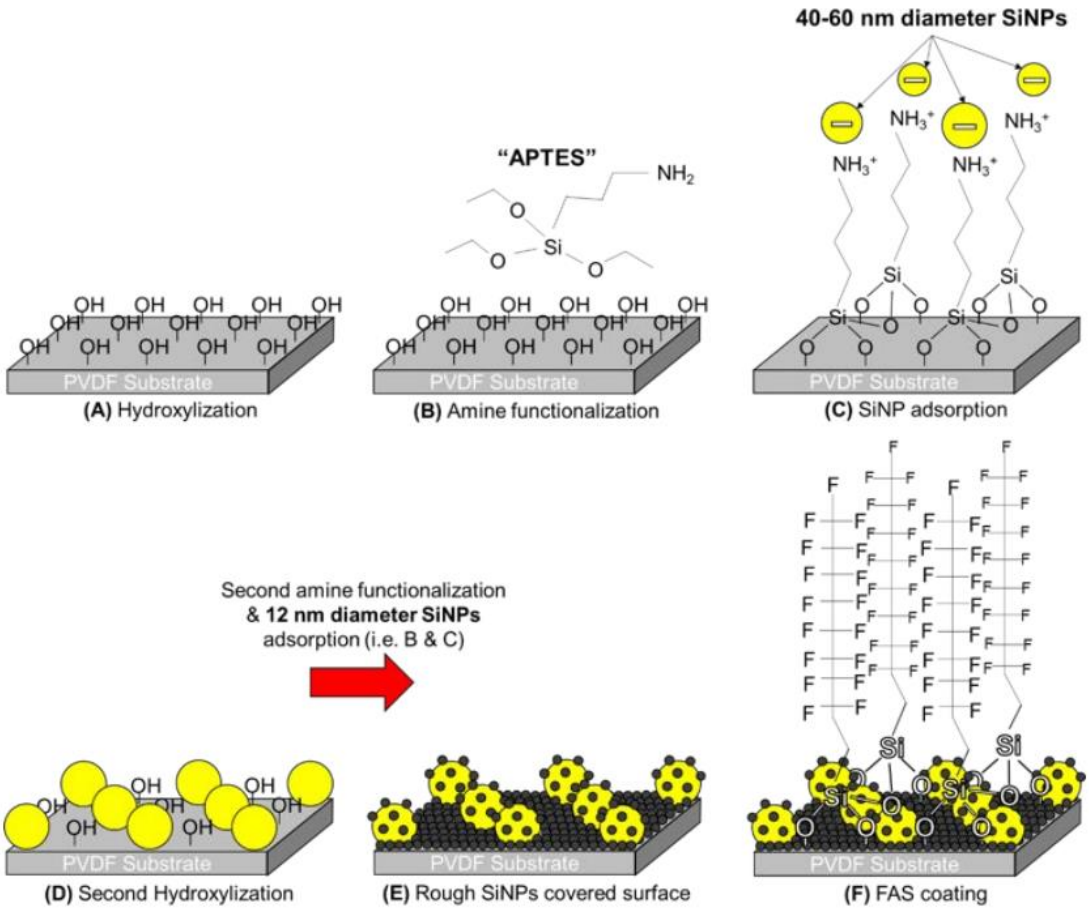


**Figure 4. 2.** Schematic illustration of superhydrophobic surface fabrication process. (A) The surface of a commercial PVDF membrane was hydroxylized with 7.5 M NaOH for ~3.5 hrs at 70°C. (B) 3-aminopropyl-triethoxysilane (APTES) is grafted to the hydroxyls via liquid phase reaction in ethanol solvent at 1 vol%. (C) SiNPs are suspended at 1 wt% in pH 4 buffer such that the amines are protonated and 40-60 nm diameter SiNPs are negatively charged. The SiNPs then electrostatically adsorb to the membrane surface. (D) The remainder of the surface without adsorbed SiNPs was hydroxylized again. (E) The remaining areas are again amine functionalized with APTES (as in (B)) and a second size of SiNPs (12 nm diameter) are adsorbed (as in (C)) to increase the surface coverage and/or hierarchical texture of the rough SiNPs layer. (F) The surface energy of the adsorbed SiNPs layer is lowered via vapor phase reaction with fluoroalkylsilane (FAS) overnight, creating a superhydrophobic surface.

*4.2.3. Membrane Characterization*

We compared the surface wetting properties of the membranes by measuring the static water contact angle (CA) with an optical tensiometer (T114, Attension). We also quantified CA hysteresis by measuring the sliding angle (SA) that is the critical tilting angle at which a water droplet starts to slide. The membrane surface morphology was characterized via scanning electron microscopy (SEM) (Zeiss Merlin).

*4.2.4. Membrane Scale Purging Experiments*

We used a direct contact MD system to perform the MD scaling experiments with the feed inlet temperature maintained at 75°C. The distillate inlet temperatures for MD experiments using the superhydrophobic and hydrophobic membranes were set at 18 and 43°C, respectively, to maintain a constant flux of 25 L $m^{-2}$ $h^{-1}$ in all cases and thus maintain the same level of concentration polarization (CP). The flow rates of the feed and distillate were maintained at 600 and 500 mL $min^{-1}$, respectively (12.8 and 10.7 cm $s^{-1}$ in our MD module, respectively). The feed mixture, with an initial volume of 500 mL, contained 14 mM $CaCl_2$ and 14 mM $Na_2SO_4$. At 75°C, the gypsum saturation index, defined as the log of the ion activity product over the solubility product, was −0.10 (PHREEQC version 3.4 from the U.S. Geological Survey) [251]. The distillate mass and conductivity were recorded in real time to determine water vapor flux and salt rejection.

During the purging steps, we first drained the distillate side of the MD cell, closed its exit, and filled it with compressed nitrogen at 60 kPa. These operations on the distillate side were performed without interrupting the feed stream. The purging was performed for 60 s every hour. Experiments were terminated when the remaining feed volume was approximately 100 mL or concentrated roughly by a factor of five and became insufficient to keep the feed loop free of air bubbles. A detailed schematic of the scale purging setup is presented in **Figure 4.3.**

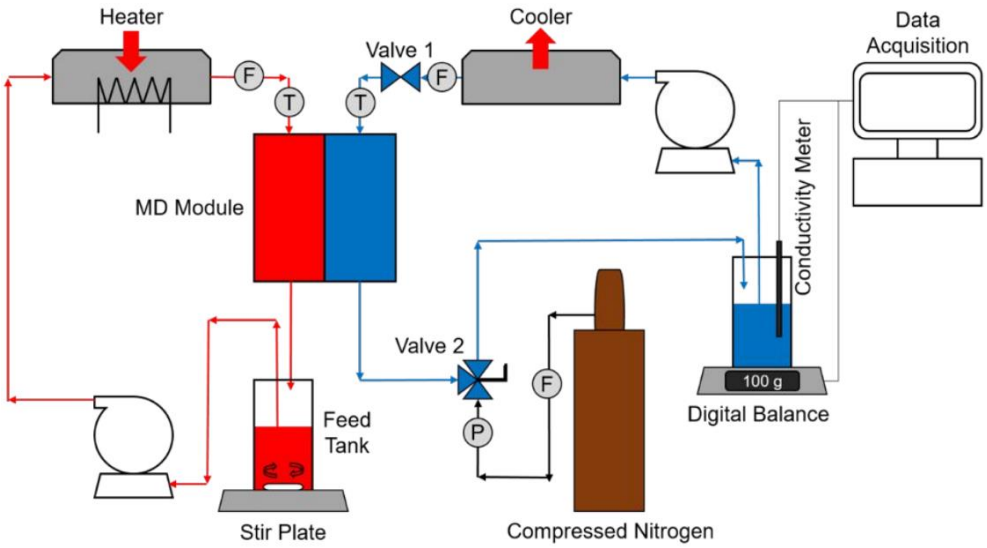


**Figure 4. 3.** Schematic of direct contact membrane distillation setup used for scale purging experiments. In regular operation the distillate loop (blue) is closed, i.e. valve 2 is turned such that the distillate outlet may return to the cooler and pass the membrane surface again. During a purge, the distillate pump is turned off, valve 1 is closed, and valve 2 is turned such that compressed nitrogen may flow into the system and pass through the membrane pores to the feed side. On the feed loop (red) liquid flow continues and the excess nitrogen exits the system from the feed tank.

## 4.3. Results and Discussion

*4.3.1. Membrane Surface Properties*

The adsorption of SiNPs to the commercial PVDF membrane surface significantly enhances the surface roughness, which is indispensible for achieving superhydrophobicity. The change in surface morphology is confirmed by comparing the SEM images of the PVDF membrane (**Figure 4.4A**) and the superhydrophobic membrane (**Figure 4.4B**). Due to both the high surface roughness and the low surface energy of the FAS coating, a very high water CA of 166 ± 4° was measured with the superhydrophobic membrane (inset of Figure 2B) as compared to the water CA of 115 ± 9° measured with the hydrophobic membrane (inset of Figure 2A).

The superhydrophobic membrane also yields an extremely low CA hysteresis. Compared to the very strong CA hysteresis of a commercial PVDF membrane with an unmeasurable SA (i.e., the water droplet remained adhered to an inverted membrane surface), the SA for the superhydrophobic membrane is only 4 ± 1°. Using a mixture of SiNPs of two different sizes (40−60 and 12 nm) as the morphological modifier works significantly better than using single-sized SiNPs (40−60 nm) for imparting the superhydrophobicity. When single-sized SiNPs were used as the sole morphological modifier, the CA was only 148 ± 2° (as compared to 166 ± 4°) and the SA was >20° (as compared to 4 ± 1°). The superior superhydrophobicity obtained using SiNPs of two different sizes may be attributed to the better surface coverage and/or to the hierarchical texture [252,253]. Regardless of the mechanism, the membrane modified with SiNPs of two different sizes achieves the superhydrophobicity (both ultrahigh CA and ultralow SA) that is required for testing our hypothesis. The excellent Cassie−Baxter state maintains a stable air layer near the membrane surface that helps to mitigate interfacial crystallization [239]. It also minimizes the depth of feed solution intrusion and the consequent growth of crystals within the membrane pores [198].

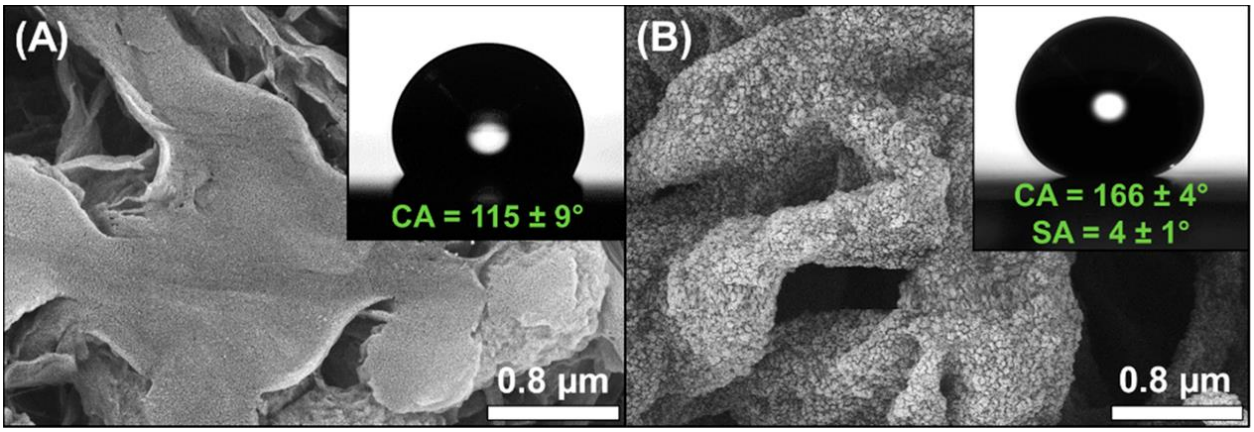


**Figure 4. 4.** SEM images of (A) commercial hydrophobic and (B) superhydrophobic membranes. Inset images show the static water contact angle (CA) and sliding angle (SA) measured with 10 µL DI water droplets. The SA of the commercial hydrophobic PVDF membrane is not reported as it was not measurable; i.e., the drop remained pinned even with an inverted membrane surface.

*4.3.2. Membrane Scaling and Effect of Purging*

The scaling behaviors of the hydrophobic and superhydrophobic membranes were first compared without purging. As more water was recovered, the feed solution became increasingly concentrated and eventually supersaturated. Formation of gypsum crystal blocks membrane pores and causes a significant flux decline [254]. The apparent flux decline occurs at a limiting saturation level or, equivalently, a limiting cumulative water recovery. This limiting recovery was around 250 mL for the hydrophobic and superhydrophobic membranes (**Figure 4.5A**). Furthermore, the initial scaling rates, defined as the average decline of normalized vapor flux per increment of distillate volume after scaling starts (i.e., the slope of flux decline in Figure 3A, which has a dimension of inverse volume), also differ between the two membranes. Before the occurrence of membrane wetting, indicated by the sharp increase in distillate conductivity at 325 mL for both membranes (**Figure 4.6A**), the initial scaling rate was around $-11 \pm 1$ $L^{-1}$ for the hydrophobic membrane, as compared to around $-7 \pm 4$ $L^{-1}$ for the superhydrophobic membrane. These observations of reduced scaling kinetics with increased membrane hydrophobicity are consistent with results from recent studies [198,239,248].

Delaying the initiation of membrane scaling or slowing the scaling rate using a superhydrophobic membrane is insufficient for practical applications of MD for treating hypersaline brine, because it does not address the fundamental challenge of scaling that leads to process failure. To truly enable MD for treating hypersaline brine, a strategy needs to be developed to either prevent scaling or readily recover the membrane performance after scaling occurs.

Toward this goal, we implemented an operation scheme with periodic gas purging to physically remove the crystals deposited on the superhydrophobic membrane surface. With 60 s of $N_2$ gas purging every hour, scaling on the superhydrophobic membrane was almost completely eliminated (blue circles in **Figure 4.5B**). Even though we observe a very small decline of vapor flux, it is mostly attributable to the reduced partial vapor pressure driving force instead of the reduced permeability of the membrane due to pore blockage. The feed solution was concentrated by 5-fold at the end of the experiment, which significantly increased the salinity and reduced the partial vapor pressure of the feed solution at the same temperature [12]. Furthermore, the purged superhydrophobic membrane never wetted, which is indicated by stable near-zero distillate conductivity (**Figure 4.6B**).

In comparison, purging with the same operation scheme mitigates scaling on a hydrophobic PVDF membrane to a significantly lower extent. Compared to MD using a hydrophobic membrane without purging, purging had a negligible influence on deterring scaling (**Figure 4.5B**). The flux decline still occurred at ~250 mL of cumulative distillate volume, and the rate of flux decline was also similar ($-7 \pm 3\ L^{-1}$). However, wetting seemed to be delayed to ~350 mL with purging as compared to ~325 mL without purging (**Figure 4.6**). The appearance of the membrane surfaces after MD experiments [with purging (**Figure 4.5C**)] differs dramatically between the hydrophobic and superhydrophobic membranes. There is clearly a film of crystal covering the entire surface of the hydrophobic membrane, whereas almost no crystal was observed on the superhydrophobic membrane except for a small fraction of the surface near the edges. Furthermore, the CA on the clear portions of the purged superhydrophobic membrane decreased very slightly to 160 ± 6° (compared to the original CA of 166 ± 4° before MD experiments). Such a CA was directly measured on the dried portion of the membrane after it was removed from the MD experiment without any further cleaning. This well-sustained superhydrophobicity suggests that (1) barely any gypsum crystal adhered to the surface of the superhydrophobic membrane when purging was implemented and (2) the FAS-coated SiNPs were stable even after multiple purging cycles.

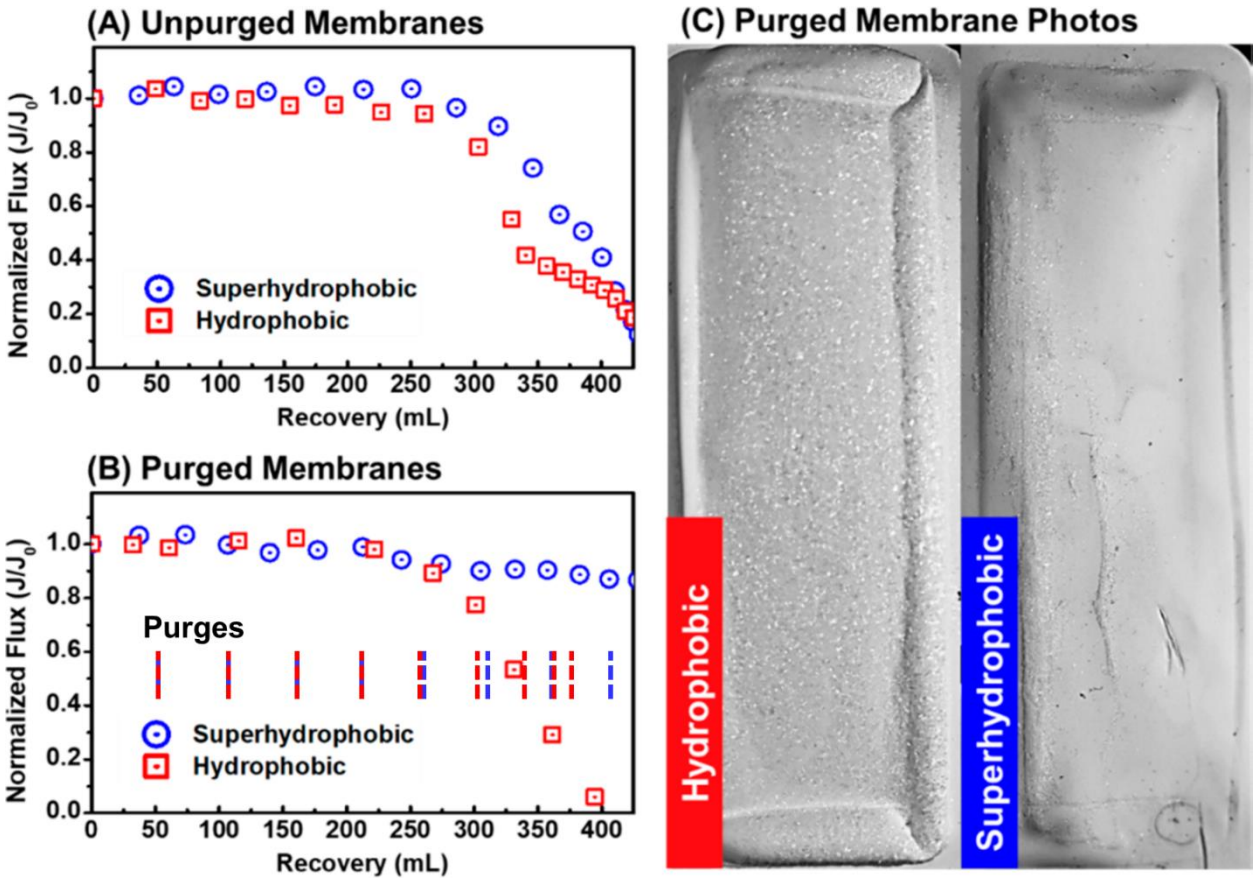


**Figure 4. 5.** (A) Normalized water flux of the hydrophobic (red squares) and superhydrophobic (blue circles) membranes during MD operation without purging. (B) Normalized water flux of the hydrophobic (red squares) and superhydrophobic (blue circles) membranes during MD operation using periodic purging with 60 kPa compressed $N_2$ for 60 s per hour (vertical dashed red and blue lines signify purges for the hydrophobic and superhydrophobic membranes, respectively). The feed solution consisted of 14 mM $CaCl_2$ and 14 mM $Na_2SO_4$ with an initial volume of 500 mL, and the feed temperature was maintained at 75°C. The distillate temperatures in experiments with the superhydrophobic and hydrophobic membranes were maintained at 18 and 43°C, respectively, such that the initial flux for both membranes was constant at 25 L $m^{-2}$ $h^{-1}$, which resulted in the same initial degree of concentration polarization. The flow rates of the feed and distillate were maintained at 600 and 500 mL $min^{-1}$, respectively (12.8 and 10.7 cm $s^{-1}$ in our MD module, respectively). (C) Photographic images of hydrophobic (left) and superhydrophobic (right) membranes after MD scaling experiments with purging (corresponding to the results shown in panel B).

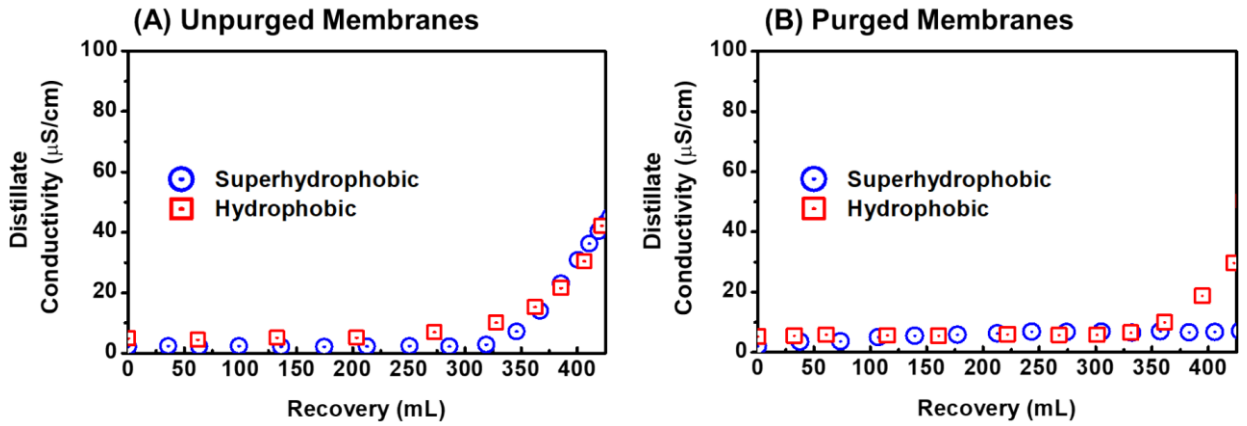


**Figure 4. 6.** Distillate conductivity from the experiments in **Figure 4.5A & B**. (A) Distillate conductivity for the hydrophobic (red squares) and superhydrophobic (blue circles) membranes during MD operation without purging. (B) Distillate conductivity for the hydrophobic (red squares) and superhydrophobic (blue circles) membranes during MD operation using periodic purging with 60kPa compressed $N_2$ for 60s per hour. The feed solution was 14 mM $CaCl_2$ and 14 mM $Na_2SO_4$ with 500 mL total volume and maintained at 75°C. The distillate temperatures of the superhydrophobic and hydrophobic membranes were maintained at 18°C and 43°C, respectively, such that the initial flux for both membranes was constant at 25 L $m^{-2}$ $h^{-1}$, thus controlling for concentration polarization. The flow rates of the feed and distillate were maintained at 600 mL $min^{-1}$ and 500 mL $min^{-1}$ (12.8 cm $s^{-1}$ and 10.7 cm $s^{-1}$ in our MD module), respectively.

*4.3.3. Mechanisms of Scale Mitigation via Purging*

Heterogeneous nucleation on favorable surfaces usually occurs more readily (and thus faster) than homogeneous nucleation according to classical nucleation theory [244]. Therefore, the increase in scaling kinetics by decreasing membrane hydrophobicity suggests that a less hydrophobic surface is more favorable for heterogeneous nucleation. The morphology of the crystal on the purged hydrophobic membrane (**Figure 4.7A**) reveals that the surface was almost fully covered by large rosette-like crystals, which is a common characteristic of heterogeneous nucleation in membrane desalination processes [255–257]. Thus, purging was ineffective in the removal of scale from the hydrophobic membrane for two possible reasons. The first is the stronger adhesion between the rosette-like crystals and the membrane surface due to both the higher surface energy of PVDF (than FAS on a superhydrophobic membrane) and the larger contact area. Perhaps more importantly, gypsum crystals grew within the hydrophobic membrane pores and formed crystal "anchors" that render physical removal of the scale layer very difficult (**Figure 4.7B**).

In contrast, purging the superhydrophobic membrane was effective in removing the crystals on the surface (**Figure 4.7C**). With superhydrophobic membranes, the crystals on the unpurged membrane and the small fraction along one edge of the purged membrane (**Figure 4.7C** inset)

were small, thin, and rod-like particles. The excellent Cassie−Baxter state achieved with the superhydrophobic membrane minimizes the intrusion of the feed solution into the membrane pores and prevents the formation of crystal "anchors" within the membrane pores (**Figure 4.7D**). Therefore, periodic purging was effective in removing the deposited gypsum particles. We note that it is not possible to replicate this effect purely with improved hydrodynamics, e.g., by increasing the feed flow rate. A recent study shows that the increased feed cross-flow velocity only delays, but does not prevent, mineral scaling on superhydrophobic membranes [198].

Previous studies investigated the use of periodic purging to mitigate scaling in MD with a hydrophobic membrane and reported that purging effectiveness was dependent upon the initial feed concentration [249,250]. For feed solutions with initial concentrations well above saturation, purging was slightly effective in slowing scaling. At such high initial feed concentrations, a large fraction of the crystals form in the bulk solution and deposit on the membrane surface as opposed to growing on the membrane surface via interfacial crystallization. However, for solutions with initial concentrations below saturation (as in the case of this study), purging did not affect the scaling behavior [251], which is similar to our experimental observation. These results suggest that purging is more effective at removing crystals that nucleate in the bulk solution and then deposit onto the surface than removing those that nucleate heterogeneously on the membrane surface and grow in situ. As it is less likely to encounter an industrial brine stream with a precipitated solid already formed, the use of a superhydrophobic membrane that minimizes interfacial crystallization and in-pore growth of crystals is necessary for purging to be effective.

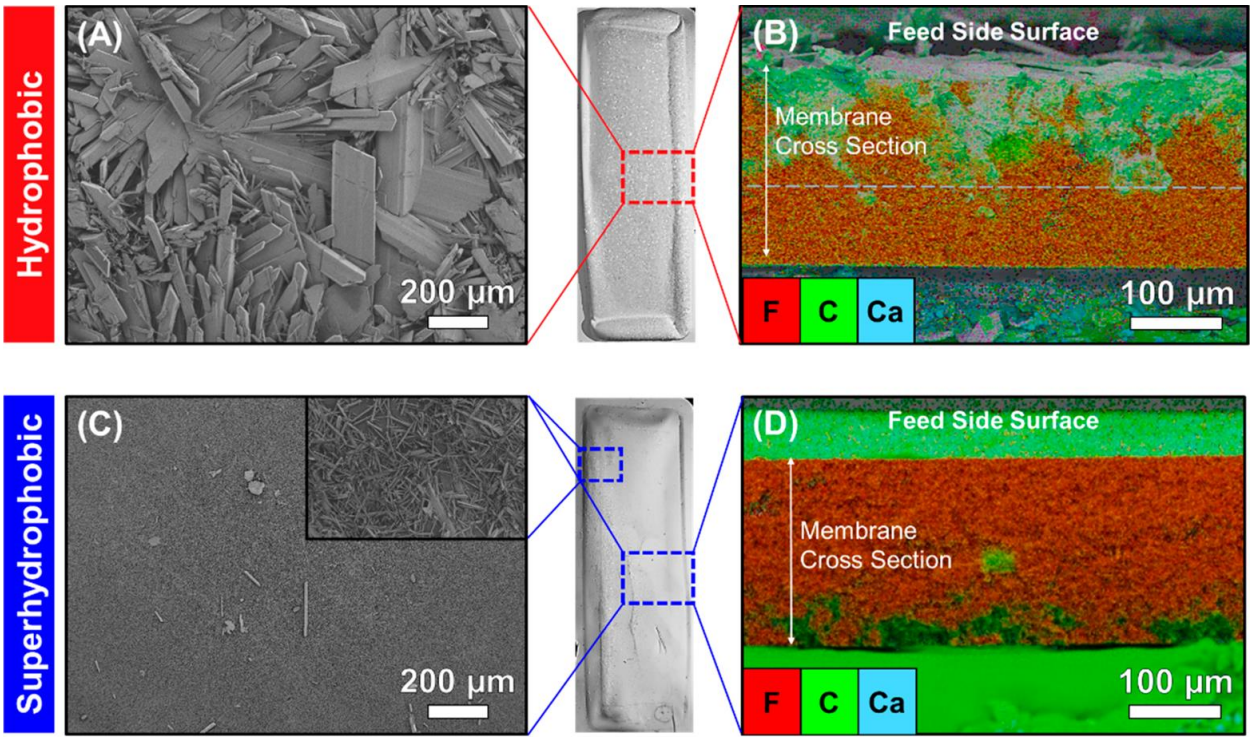


**Figure 4. 7.** Scale layer characterization on membranes from the MD experiments with purging. Membrane samples were removed from the experimental setup and dried immediately after the MD experiments. The photographic images at the center are the same as those in **Figure 4.5C**. (A) Top-down SEM image of the scale layer on the hydrophobic membrane surface. (B) SEM−EDS map of the content of fluorine (red), carbon (green), and calcium (blue) in the hydrophobic membrane cross section. The crystal intrusion depth is approximated by the blue dashed line. (C) Top-down SEM images of the crystal free region of the superhydrophobic membrane surface (main figure) and the small rod-like crystals along the edge of the superhydrophobic membrane surface (inset). (D) SEM−EDS map of the contents of fluorine (red), carbon (green), and calcium (blue) in the membrane cross section.

### 4.4. Implications

The proposed novel strategy that synergistically combines membrane superhydrophobicity and physical gas purging has been demonstrated to be highly effective in preventing gypsum scaling in MD. We show that only this synergistic combination, not purging or superhydrophobic membrane alone, can result in truly effective mitigation of membrane scaling. Overcoming the challenge of mineral scaling in MD using this novel strategy will enable MD to treat hypersaline brine with sustainable performance. This strategy can potentially be employed, with additional system integration and innovation, to achieve complete separation of water and salt crystals and thereby replace mechanical vapor compression as a lower-cost technology using low-grade waste heat for brine concentration and crystallization in ZLD.

**Acknowledgements:** This work is partially supported by National Science Foundation Grant CBET-1705048. T.H. acknowledges support from the American Chemical Society Petroleum Research Foundation via award ACS-PRF 57353 DNI. C.S. acknowledges support from the China Scholar Council via Scholarship 201804910753.

# CHAPTER 5: A NOVEL, NON-EVAPORATIVE APPROACH TOWARD BRINE MANAGEMENT AND ZERO LIQUID DISCHARGE

This chapter is in preparation for submission to the journal Nature Water as the following peer-reviewed manuscript: Horseman, T., Wang, R., Wang, X., and Lin, S. Electrodialytic-Crystallizer: Novel approach to simultaneous zero liquid discharge and mineral crystal recovery. Nature Water, (2022).

## 5.1. Introduction

With growing global population, the associated industrialization, climate change, and the associated droughts, experts project that nearly half of the global population will suffer from water stress by 2050 [258]. As such, more responsible water management is necessary for sustainable development of urban centers and industry moving forward [259,260]. While conventional water treatment processes only recover about 50% of freshwater from wastewater, the remaining 50% is high salinity brine that is often disposed of rather than being treated for reuse [5,261]. Industry historically generates large volumes of that brine, but with relatively looser regulations, typically discharged it to the environment. However, zero liquid discharge (ZLD) will soon become the preferred method for brine management as water sources become scarcer and regulations become stricter to mitigate the negative impacts of freshwater withdrawals and brine discharge on the environment [262].

Cost-effective ZLD is technically challenging due to the high level of salinity, or total dissolved salts (TDS), of the brine [5,263,264]. The state-of-the-art desalination process, reverse osmosis (RO), is operationally limited to a maximum level of TDS due to the dependence on applied pressure and osmotic pressure difference [26,265,266]. While RO does exist in conventional ZLD treatment trains, downstream steps for complete separation of mineral crystals and freshwater are limited to evaporative methods. These evaporative processes are intrinsically energy intensive due to the liquid-to-vapor phase change, which due to the relatively high latent heat of vaporization for water (> 650 kWh $m^{-3}$), is nearly two orders of magnitude greater than the minimum Gibbs free energy for concentrating and crystallizing the brine (typically < 10 kW $m^{-3}$) [18].

The key to reducing energy consumption of evaporative processes is to maximize latent heat recovery. State-of-the-art technologies, including mechanical vapor compression (MVC), multi-effect distillation (MED), and multi-stage flash distillation (MSF) employ this technique by

reusing heat released during vapor condensation in one stage to produce vapor in a subsequent stage [18]. However, even the most common and energy efficient evaporative technology, MVC, consumes upwards of 30-40 $kWh_e$ $m^{-3}$ of the treated brine [10]. Not only does the high energy consumption of MVC constrain the economic viability of ZLD, but the high capital cost associated with expensive materials of fabrication and long lead times associated with custom fabrication limits the practical application of ZLD [5,7]. Thus, reducing the energy consumption for brine concentration and crystallization and improving the modularity of these downstream units will enable more practical and universal application of ZLD and brine management.

Electrodialysis (ED) is a well-established electrically driven process capable of concentrating solutions of high salinity. In a typical ED system, the incoming feed stream flows through a stack of alternating cation and anion ion exchange membranes sandwiched between two electrodes. An applied electric field causes ions to migrate toward the electrode of opposite charge, across their respective ion exchange membranes. Due to the alternating configuration of ion exchange membranes, alternating compartments are either diluted or concentrated within the ED unit. Thus, in conventional ED, the incoming feed stream is split into a lower concentration, diluate stream and a concentrated brine stream (**Figure 5.1A**). Conventionally, electrodialysis is utilized for brackish water treatment [37,267,268], however, unlike RO, ED can treat brines of higher salinity because it is less susceptible to fouling due to mineral crystals and does not require high operating pressure to induce separation. In fact, ED has been used for making table salts and has been investigated as a unit process in a ZLD treatment train for further concentrating RO brine before MVC-based concentration and crystallization [37–44]. However, in existing treatment trains, evaporative crystallizers are still required following ED to achieve complete ZLD and mineral crystal recovery.

Herein, we propose a novel, modular, fully-electrified, and non-evaporative brine concentration and crystallization system called an electrodialytic-crystallizer (EDC). Although EDC fundamentally employs ED to desalinate the incoming feedwater, it operationally differs from conventional ED in three major aspects. First, there is a feed inlet that splits into diluate and brine outlet streams in conventional ED. In EDC, there is only one feed stream entering and one diluate stream exiting the system. Ions transport from the diluate to an internally circulated brine loop via ED operation. Because it is initially saturated, ions supersaturate the brine loop and crystals are precipitated and removed in a crystallization vessel, either be a jacketed settling tank

with temperature control or a microfiltration unit (**Figure 5.1A**). Second, ED is typically used to treat feedwater in the range of brackish water (< 5 g $L^{-1}$), whereas in EDC, the salinity of the incoming feed stream is on the range of seawater or higher (> 10 g $L^{-1}$). This results in much lower salt concentrations, and solution conductivities, in both the diluate and brine streams in conventional ED compared to EDC (**Figure 5.1B**). Third, the low salinities in conventional ED result in larger voltage drop across the ion exchange membranes in the ED stack. The low salinity of the diluate dominates the voltage drop in the system as it approaches zero due to concentration polarization near the ion exchange membrane in conventional ED (according to $V_{mem}$, **Figure 5.1C**) [32]. In EDC, even the salt concentration in the diluate is greater than the typical salt concentration in the brine of conventional ED, as such, the voltage drop across the ion exchange membranes in the ED stack tends to be around half of that compared to conventional ED.

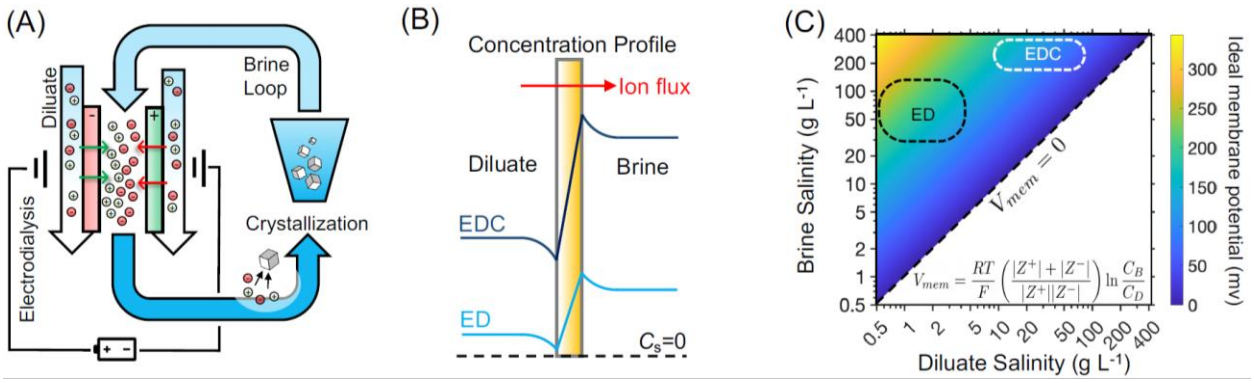


**Figure 5. 1.** Schematic of (A) the proposed electrodialytic-crystallizer (EDC) system with an internally circulated brine loop with crystal collector/temperature swing crystallizer. (B) Schematic diagram of the relative concentration profiles in ED vs EDC. (C) Ideal membrane potential in ED compared to EDC. As a result of the higher solution salinity in EDC, typical membrane potential is approximately half of that compared to conventional ED.

To demonstrate the working principle of EDC, we construct a bench-top EDC system utilizing a commercially available electrodialysis (ED) cell to concentrate single salt solutions at concentrations like hypersaline reverse osmosis brine. We utilize a small temperature swing in a stirred crystallizer to produce and collect crystals while controlling for long induction times. Fundamentally, we elucidate the role of system operating parameters (i.e., applied current density, crystallizer temperature, and crystallizer residence time) on crystallization kinetics and crystal size distribution. Based on the comparison of salt solubility in the crystallizer and water transport in the ED cell, we also analyze EDC's capabilities to concentrate and crystallize a series of common

single salts and ultimately suggest a governing criterion that dictates which specific salt species may be successfully crystallized in the EDC system.

## 5.2. Materials and Methods

### *5.2.1. Materials and Chemicals.*

The electrodialysis cell was a commercial lab-scale cell, ED64002 offered by PCCell GmbH (Heusweiler, Germany) with 64 $cm^2$ active membrane area, 80 cm processing length, up to 20 cell pair capacity, and terminal PC MTE cation exchange membranes. Commercial ion exchange membranes PC SA (anion) and PC SK (cation) meant for standard desalination and PC Acid 60 OT (anion) and PC S100 (cation) meant for low water transfer were purchased from PCCell GmbH. Commercial ion exchange membranes AMVN (anion) and CMVN (cation) meant for standard desalination and high salinity brine treatment were purchased from AGC Chemicals Americas, Inc. (Exton, PA). Sodium sulfate ($Na_2SO_4$, anhydrous, ACS reagent), potassium sulfate ($K_2SO_4$, ACS reagent), sodium carbonate ($Na_2CO_3$, anhydrous, ACS reagent), potassium chloride (KCl, ACS reagent), and magnesium sulfate ($MgSO_4$, anhydrous, reagent) were purchased from Sigma-Aldrich (St. Louis, MO). Potassium nitrate ($KNO_3$, ACS reagent), sodium chloride (NaCl, ≥ 99.0%), and ammonium chloride ($NH_4Cl$, ≥ 99.5%) were purchased from Fisher Scientific (Waltham, MA). The microfiltration membrane was a 316 stainless steel filter mesh with 5-micron nominal pore size purchased from McMaster-Carr (Elmhurst, IL).

### *5.2.2. Electrodialytic Crystallizer Experiments.*

In all experiments in this study, diluate and brine flow rates were maintained at 200 mL $min^{-1}$ and electrode rinse flow rate was maintained at 500 mL $min^{-1}$. Conductivity and temperature were recorded from the diluate reservoir and crystallizer to determine salt transport, total suspended solids (TSS) was measured gravimetrically from the crystallizer to determine solid crystal concentrations, and volume change in the diluate was recorded to determine water transport. Voltage across the ED stack was monitored from the constant current power source.

### *5.2.3. System Evaluation and Optimization Experiments.*

Preliminary batch experiments were conducted with a rudimentary proof-of-concept system (**Figure 5.2A**) to demonstrate the working principle of EDC. The ED cell was configured with 2 cell pairs of the standard PC SA and PC SK (**Table 5.1**) ion exchange membranes from PCCell GmbH with terminal cation exchange membranes at both electrodes. The brine reservoir, or

crystallizer, was a stirred 316 stainless steel vessel immersed in a cooling bath. Small temperature swing was utilized to induce crystal nucleation within reasonable operational period. At the saturation levels achieved in this study, the induction time for all salts was over 12 hours, so the temperature swing not only induced crystal nucleation and controlled for different residence time between different salts, but also allowed continuous crystal production within the period of the EDC experiment. To inhibit crystal formation within the ED cell, the saturated brine exiting the crystallizer passed through a heater held at 25°C before entering the ED cell.

**Table 5. 1.** Properties of the ion exchange membranes used in this study.

| | **PCA GmbH** | | **PCA GmbH** | | **AGC Chemicals Americas, Inc.** | |
|---|---|---|---|---|---|---|
| **Membrane Type** | Anion Exchange | Cation Exchange | Anion Exchange | Cation Exchange | Anion Exchange | Cation Exchange |
| **Model** | PC SA | PC SK | PC Acid60 OT | PC S100 | AMVN | CMVN |
| **General Use** | *Standard Desalination* | | *Low water transfer* | | *Standard Desalination* | |
| **Thickness (mm)** | 0.1-0.11 | 0.1-0.12 | 0.1-0.11 | 0.1-0.11 | 0.1 | 0.1 |
| **Resistivity (Ω cm$^{-2}$)** | 1.8 | 2.5 | 2.4 | 4.5 | 2.0[b)] | 2.0[b)] |
| **Transport Number** | >0.95[a)] | >0.95[a)] | >0.96[a)] | >0.96[a)] | >0.97 | >0.95 |

[a)] Measured in 0.1 and 0.5 N KCl [b)] Measured in 0.5 M NaCl

We initially studied the effect of crystallizer temperature on crystallization kinetics with the proof-of-concept system. We varied the initial concentration of the brine such that it was initially saturated $Na_2SO_4$ (in 1 L of DI water) at 10, 15, and 20°C, while the temperature of the solution in the crystallizer was 2°C less than the saturation temperature, i.e., 8, 13, and 18°C, respectively. The diluate was initially 6 wt% $Na_2SO_4$ in 2 L of deionized (DI) water and the circulated electrolyte, or electrode rinse, was 3 wt% $Na_2SO_4$ at room temperature.

Crystal formation led to clogging of the process streams and ED cell, risking process failure in the proof-of-concept system. To prevent clogging and allow for better control of crystallizer residence time, an improved system was assembled (**Figure 5.2B**). The brine exiting the crystallizer was pumped through a custom cross flow microfiltration (MF) cell following the crystallizer where the rejected solid-liquid stream was immediately returned to the crystallizer. Following the MF cell, the permeate passed through a heater held at 25°C to prevent crystal formation within the ED cell. Ions transported from the diluate to the saturated brine stream within the ED cell and the supersaturated brine returned to the crystallizer where excess ions were

precipitated as solid salts. As the induction time for the single salts in this study may vary from several hours to several days, a small temperature swing of 2°C was used to induce crystal nucleation.

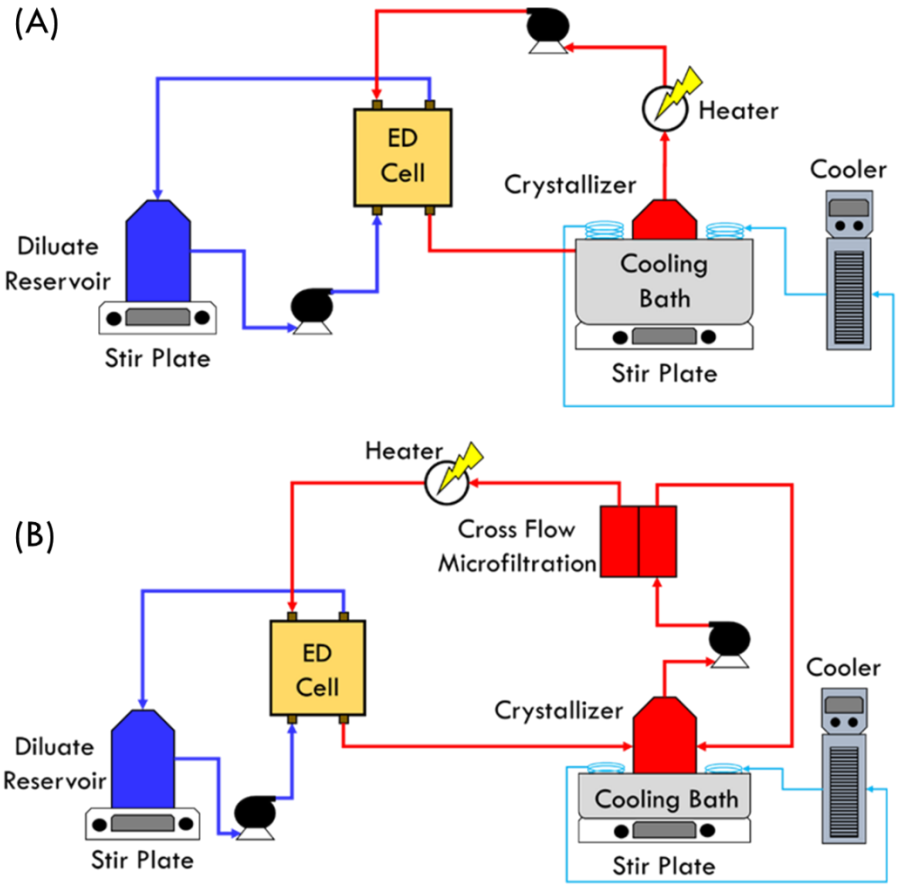


**Figure 5. 2.** Schematic diagram of (A) the proof-of-concept and (B) improved bench-top EDC systems.

To compare the performance of the proof-of-concept and improved systems, we varied current density (35, 50, and 65 mA $cm^{-2}$) to elucidate the effect on crystallization kinetics and size distribution. The ED cell was configured with 2 cell pairs of the PCCell PC SA and PC SK membranes with terminal cation exchange membranes at both electrodes. The initial diluate was 6 wt% $Na_2SO_4$ in 2 L of deionized (DI) water, the initial brine was saturated $Na_2SO_4$ (192 g $L^{-1}$ at 20°C [269]) in 1 L of DI water, and the electrolyte, or electrode rinse, was 3 wt% $Na_2SO_4$. The temperature in the crystallizer was maintained at 18°C. Images of crystals in solution were obtained via stereo microscope with digital camera purchased from AmScope (Irvine, CA) and size distribution was evaluated using ImageJ free image processing software.

*5.2.4. Membrane Comparison Experiments.*

With the improved EDC system, we used constant current density (20 mA $cm^{-2}$) batch experiments to evaluate the performance of commercial ion exchange membranes from PCCell GmbH and AGC Chemicals Americas, Inc. (**Table 5.1**) in the context of EDC. The ED cell was configured with 2 cell pairs with terminal cation exchange membranes at both electrodes. The initial diluate was 6 wt% $Na_2SO_4$ in 2 L of deionized (DI) water at room temperature, the initial brine was saturated $Na_2SO_4$ (192 g $L^{-1}$ at 20°C) in 1 L of DI water, and the electrolyte, or electrode rinse, was 3 wt% $Na_2SO_4$ at room temperature. The temperature in the crystallizer was maintained at 18°C.

*5.2.5. Crystallization Criterion Experiments.*

After selection of the most appropriate ion exchange membrane, we evaluated which salts could be successfully crystallized in the improved EDC system. The ED cell was configured with 5 cell pairs with terminal cation exchange membranes at both electrodes. The initial diluate was 0.6 M of the single salt in 4 L of deionized (DI) water at room temperature. The initial brine solution was saturated with respect to the single salt being studied at 20°C in 1 L of DI water [269]. The electrode rinse solution was 0.25 M sulfate salt (in 2L DI water) of the respective cation being studied, i.e., $Na_2SO_4$ for NaCl or $K_2SO_4$ for KCl, at room temperature. The temperature in the crystallizer was maintained at 18°C.

## 5.3. Results and Discussion

*5.3.1. System Evaluation and Optimization.*

In the preliminary stages of this study, a rudimentary proof-of-concept system was assembled to demonstrate the working principle of EDC (**Figure 5.3A**, option 1 in red without microfiltration, MF). Crystallizer temperature was 8, 13, and 18°C while the brine was saturated with $Na_2SO_4$ at 10, 15, and 20°C, respectively. The EDC concept was successfully demonstrated at each temperature as sodium sulfate crystals were produced. At constant crystallizer temperature, $Na_2SO_4$ crystal concentration, indicated by total suspended solids (TSS), in the crystallizer increased with time (**Figure 5.3B**). This is due to increased salt transport; at constant current density, total salt transport from the diluate to the brine stream increases with time. Because the brine stream is initially saturated, this salt transport supersaturates the brine within the ED cell. As

that supersaturated brine enters the crystallizer and temperature decreases, the saturation index increases rapidly, and crystals precipitate out of solution.

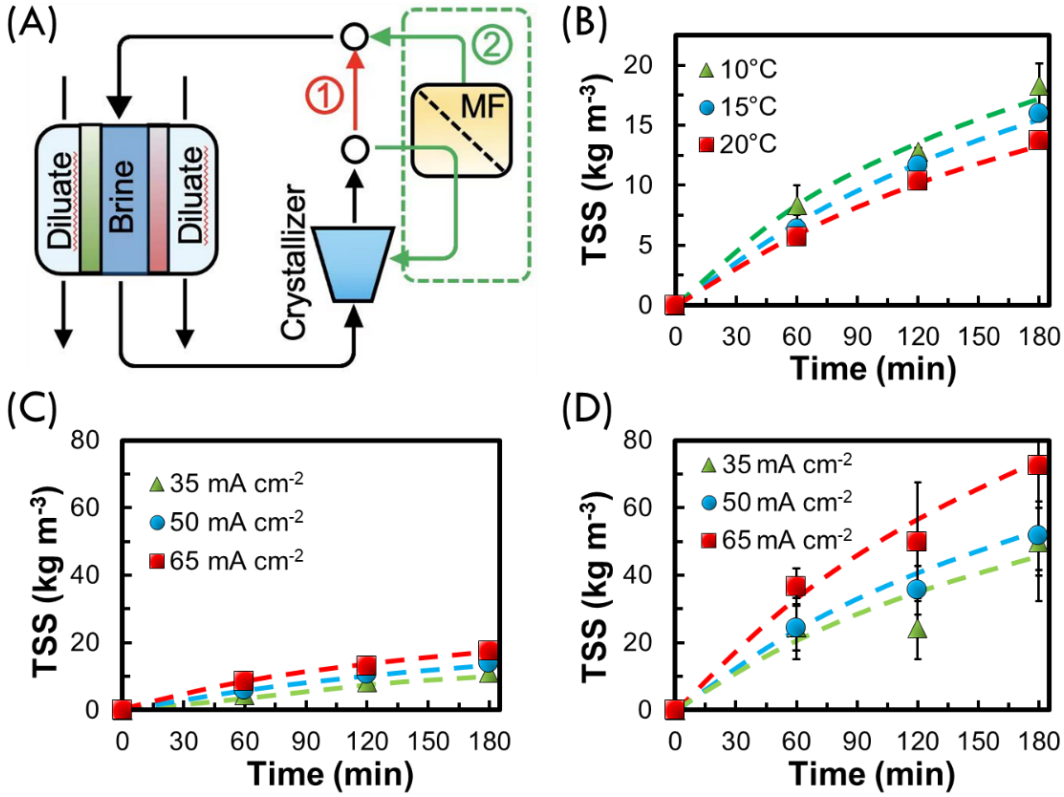


**Figure 5. 3.** (A) Schematic diagram of EDC system with optional microfiltration (MF) unit. Proof-of-concept system was without MF cell (option 1 in red) while the improved system had the MF cell incorporated (option 2 in green). (B) Total suspended solids (TSS) production rate in the proof-of-concept EDC system. Initially saturated 1 L sodium sulfate brine at 20°C (192 g $L^{-1}$), 15°C (132 g $L^{-1}$), and 10°C (91 g $L^{-1}$). The temperature of the brine in the crystallizer was maintained at 18°C for the brine saturated at 20°C, at 13°C for the brine saturated at 15°C, and at 8°C for the brine saturated at 10°C. Applied current density was 50 mA $cm^{-2}$. Total suspended solids (TSS) production rate with (C) the proof-of-concept system (depicted in **Figure 5.1A**) and (D) the improved EDC system (depicted in **Figure 5.1B**). Applied current densities 35, 50, and 65 mA $cm^{-2}$, initially saturated 1 L sodium sulfate brine (192 g $L^{-1}$ at 20°C), and crystallizer temperature at 18°C. (B-D) Error bars represent the standard deviation of two trials, when not visible, error bars are smaller than the size of the data point. ED cell configured with 2 cell pairs of the PC SA and PC SK standard desalination ion exchange membranes from PCA GmbH. Initial diluate was 2 L of 6 wt% sodium sulfate. Dashed lines added to guide the eye.

Regardless of $Na_2SO_4$'s strong solubility-temperature relationship, which is stronger as temperature increases from 10-20°C [269], crystallizer temperature did not affect crystal induction time as crystals formed almost instantaneously upon initiation of the experiment. However, a tradeoff exists between the initial amount of salt required to saturate the brine versus the energy consumption to induce temperature swing in the crystallizer. At low crystallizer temperature (8°C),

less salt is required to saturate the brine initially, but the energy consumption to induce temperature swing is greatest. Alternatively, higher crystallizer temperature (18°C) requires more salt to saturate the brine initially, but energy consumption is almost negligible. As such, we chose to move forward with small 20-18°C temperature swing in the crystallizer as to reduce energy consumption in the EDC process. Notably, we observed that with all else held constant, i.e., current density, flow rates, and initial diluate concentration, crystallization kinetics increased by approximately 20% as crystallizer temperature decreased. This requires a more detailed explanation and will be discussed in a later section.

To elucidate the role of salt transport on crystallization kinetics, we applied three constant current densities in the proof-of-concept system (35, 50, and 65 mA $cm^{-2}$). Crystallization kinetics, as demonstrated by the slope of TSS over time, increased with increasing current density (**Figure 5.3C**). This is to be expected as the flux of salt to the brine stream is proportional to current density. Thus, with constant membrane area and time, higher current density results in higher rate of salt transport. Because the brine stream is initially saturated, increased rate of salt transport results in faster supersaturation of the brine, and thus, increased crystallization kinetics. However, in the proof-of-concept EDC system (**Figure 5.3A**, option 1 in red without MF), suspended crystals exited the crystallizer and flowed through the EDC system. This not only risked clogging the brine stream within the ED cell, pumps, and tubings, ultimately risking complete process failure, but also reduced the crystal residence time within the crystallizer, which stunts crystal growth. As such, an industrially relevant, improved EDC system was assembled with a cross-flow microfiltration (MF) cell integrated into the brine loop (**Figure 5.3A**, option 2 in green with MF). This MF served to reject crystals > 5 μm from entering the brine loop and ED cell and quickly returned them to the crystallizer, ultimately, increasing the crystal residence time within the crystallizer.

To elucidate the role of salt transport on crystallization kinetics, we applied three constant current densities in the proof-of-concept system (35, 50, and 65 mA $cm^{-2}$). Crystallization kinetics, as demonstrated by the slope of TSS over time, increased with increasing current density (**Figure 5.3C**). This is to be expected as the flux of salt to the brine stream is proportional to current density. Thus, with constant membrane area and time, higher current density results in higher rate of salt transport. Because the brine stream is initially saturated, increased rate of salt transport results in faster supersaturation of the brine, and thus, increased crystallization kinetics. However, in the

proof-of-concept EDC system (**Figure 5.3A**, option 1 in red without MF), suspended crystals exited the crystallizer and flowed through the EDC system. This not only risked clogging the brine stream within the ED cell, pumps, and tubings, ultimately risking complete process failure, but also reduced the crystal residence time within the crystallizer, which stunts crystal growth. As such, an industrially relevant, improved EDC system was assembled with a cross-flow microfiltration (MF) cell integrated into the brine loop (**Figure 5.3A**, option 2 in green with MF). This MF served to reject crystals > 5 µm from entering the brine loop and ED cell and quickly returned them to the crystallizer, ultimately, increasing the crystal residence time within the crystallizer.

Like the proof-of-concept system, increased salt transport due to increased current density resulted in increased crystallization kinetics in the improved system. Expectedly, salt transport between the proof-of-concept and improved systems did not vary drastically, indicated by the similar decline in diluate conductivity (**Figure 5.4A** and **5.4B**, respectively). However, TSS at any given time increased by an approximate factor of 4 in the improved system compared to the proof-of-concept system (**Figure 5.3D**). Crystals harvested from the crystallizer at 50 and 65 mA $cm^{-2}$ in both systems were imaged via stereo microscope and analyzed via ImageJ image processing software.

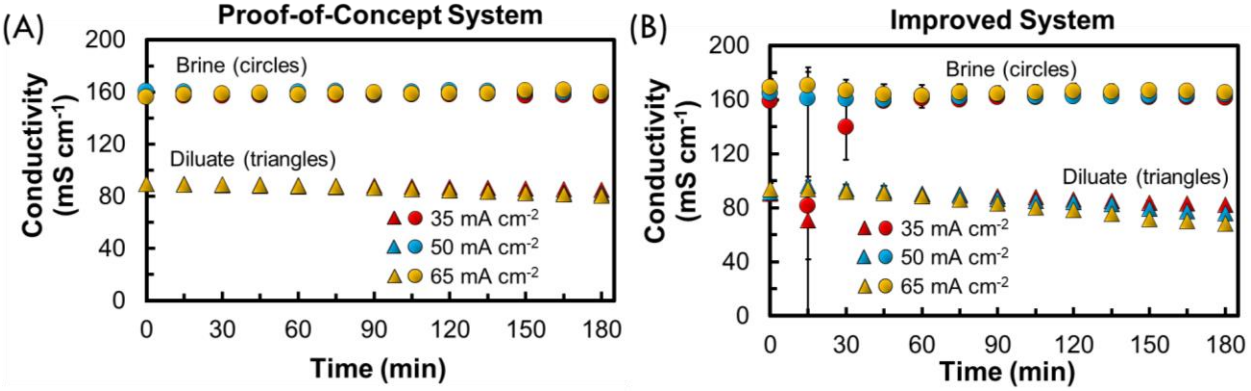


**Figure 5. 4.** Data from the systematic study of the effect of current density on crystal concentration from **Figure 5.3C & 5.3D**. Brine (circles) and diluate (triangles) conductivity in (A) the proof-of-concept system and (B) in the improved system (two systems depicted in **Figure 5.1**). ED cell configured with 2 cell pairs of the PC SA and PC SK standard desalination ion exchange membranes from PCA GmbH. Applied current density was 35, 50, and 65 mA $cm^{-2}$, the initial diluate was 2 L of 6 wt% sodium sulfate, and the initial brine was 1 L of saturated sodium sulfate (192 g $L^{-1}$) at 20°C. The temperature of the brine in the crystallizer was maintained at 18°C. Error bars represent the standard deviation of two trials. When not visible, error bars were slightly smaller than the size of the data points.

While the average crystal size increased from 50 to 65 mA $cm^{-2}$ in both systems, the crystal size distribution was much narrower with the improved system. For example, at 50 mA $cm^{-2}$, the spread of crystal sizes around the mean, or the coefficient of variation, for the proof-of-concept system was 0.59 while it was only 0.35 with the improved system (**Figure 5.5A**). Similarly, at 65 mA $cm^{-2}$, the coefficient of variation for the proof-of-concept system was 0.66 while it was only 0.42 for the improved system (**Figure 5.5B**). This enhancement in TSS production rate and narrowing of crystal size distribution can be attributed to increased residence time within the crystallizer. By addition of MF cell into the brine loop, smaller crystals (> 5 µm in this study) that stay suspended in solution within the crystallizer and are more likely to exit via the suction side of the pump, are rejected by the MF cell and quickly returned to the crystallizer where they can grow. Without MF cell, smaller crystals in the proof-of-concept system are continually precipitated at the lower temperature in crystallizer then redissolved at the higher temperature within the brine loop between the crystallizer and ED cell.

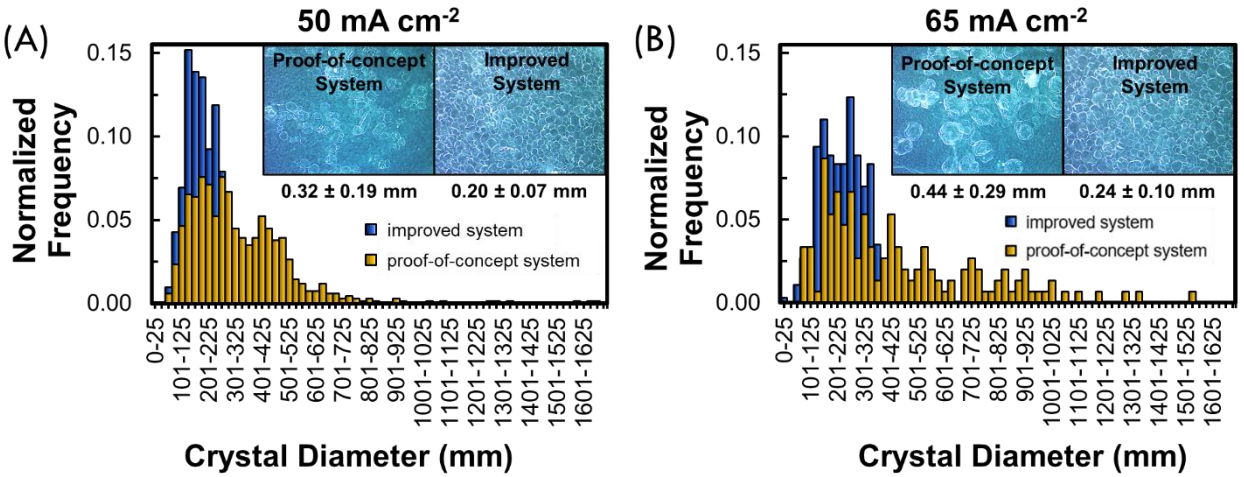


**Figure 5. 5.** Crystal size distribution for the crystals produced with proof-of-concept (orange) and improved system (blue) at (A) 50 mA $cm^{-2}$ and (B) 65 mA $cm^{-2}$. Insets show stereo microscope images of the crystals with average and standard deviation of the crystals denoted below.

With demonstrated crystal size uniformity enhancement with the improved system, the ability to control crystal size was further analyzed. We compared the crystal sizes at 35, 50, and 65 mA $cm^{-2}$ with the improved system and observed a consistent increase in average crystal size as the current density increased (**Figure 5.6A**), while the coefficient of variation remained relatively constant at each current density (**Figure 5.6B**). Early in the experiment (60 min), the crystal size distribution tended to be slightly skewed toward the right (**Figure 5.6C-E**). However, with time,

the crystal size tended to a more normal distribution (**Figure 5.6F-H** & **5.6I-K**). Furthermore, as the crystal size distribution became more normal, crystal size increased by about 27% on average every 60 min. For example, at 65 mA $cm^{-2}$, the average crystal size increased by 25% from 60 to 120 min and by 20% from 120 to 180 min (**Figure 5.6E, H, K**). Even though our crystallizer was more of a cylindrical shape and agitated by stir bar at the bottom of the vessel, these preliminary results give promise for advanced crystal size control in an industrially relevant, conical-bottom crystallizer with variable speed agitation.

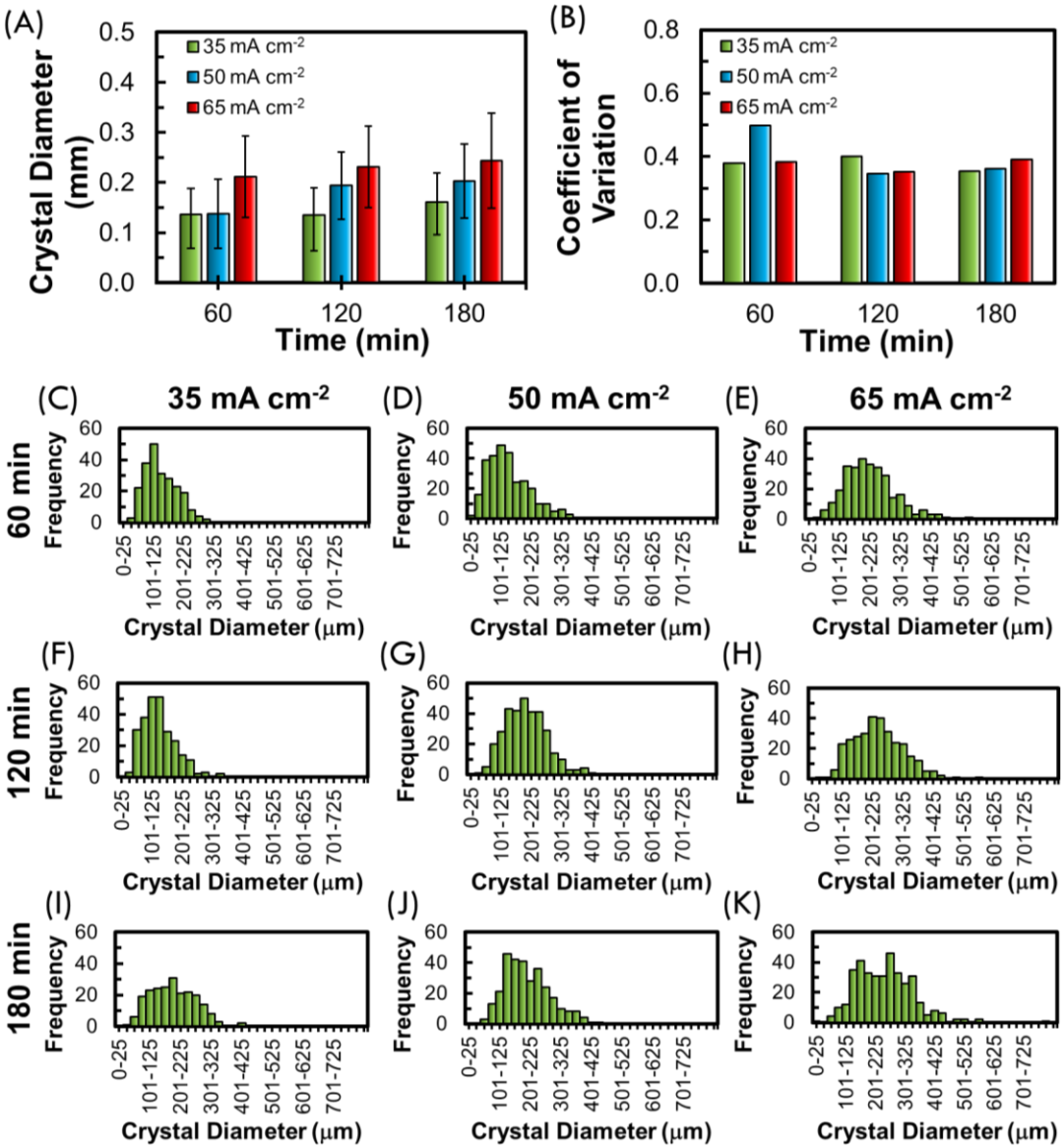


**Figure 5. 6.** (A) Crystal diameter measured during the experiments in **Figure 5.3D**. Error bars represent the standard deviation over approximately 200 crystal diameter measurements taken via ImageJ. (B) Coefficient of variation for the data presented in (A). (C-K) Crystal size distributions from experiments in **Figure 5.3D**.

*5.3.2. Membrane Comparison.*

After EDC system optimization and evaluation, the performance of several commercial ion exchange membranes were analyzed in the improved EDC system with respect to energy consumption, desalination performance, and most importantly, crystallization capabilities. Standard desalination and low water transfer membranes from PCCell GmbH and membranes from AGC Chemicals Americas, Inc. that are marketed for high salinity brine treatment were analyzed. At constant operating conditions, the voltage drop across the ED stack with the low water transfer membranes from PCCell was approximately 25% greater than the voltage drop measured with the standard PCCell and AGC ion exchange membranes (**Figure 5.7A**). As the membranes studied are all of similar thickness, voltage drop can be attributed to the relatively higher resistivity of the low water transfer PCCell membranes (**Table 5.1**). Voltage drop across the ED stack is directly related to the energy consumption in the EDC process, as such, membranes with higher resistance tend to increase energy consumption in EDC.

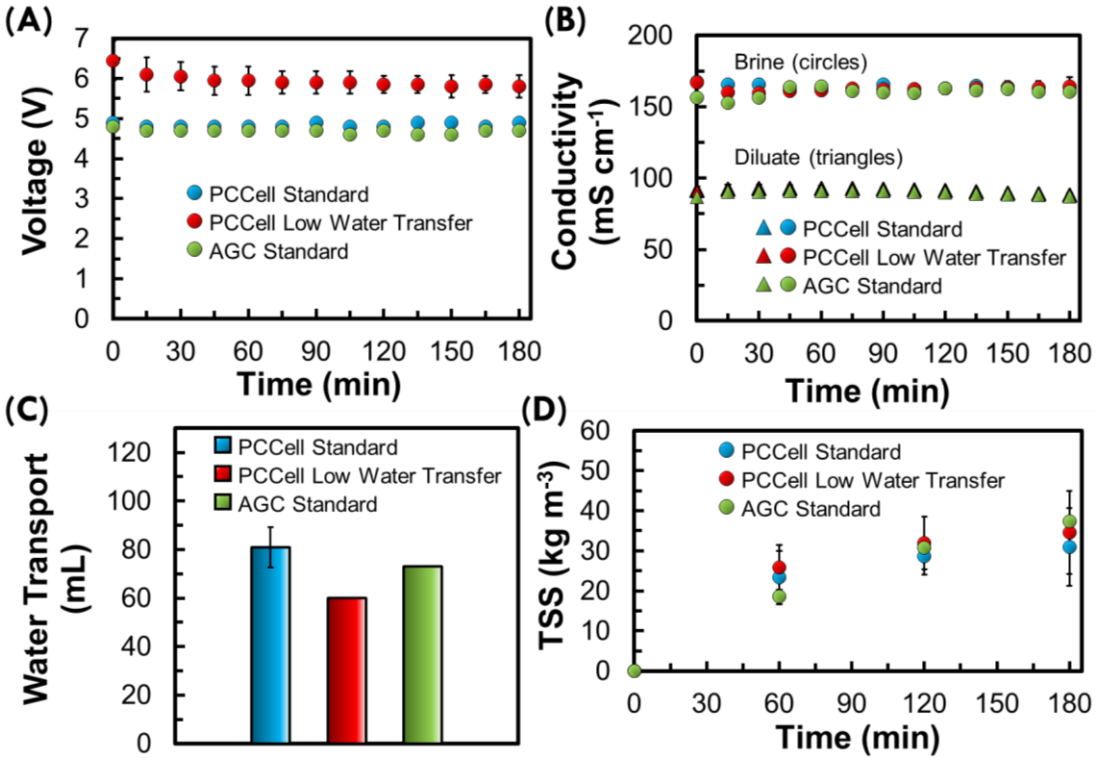


**Figure 5. 7.** Performance comparison between the selected ion exchange membranes analyzed in this study. (A) Voltage drop across the ED cell, (B) conductivity of the brine (circles) and diluate (triangles), (C) measured total water transport over the 3-h experiment, and (D) total suspended solids (TSS) production rate in the improved EDC system. Error bars represent the standard deviation of two trials. ED cell configured with 2 cell pairs, applied current density was 20 mA $cm^{-2}$, initial diluate was 2 L of 6 wt% sodium sulfate, and initial brine was 1 L of saturated sodium sulfate (192 g $L^{-1}$) at 20°C. The temperature of the brine in the crystallizer was maintained at 18°C.

In terms of desalination performance, EDC with each of the membranes reduced the salinity in the diluate (indicated by conductivity) by the same amount (**Figure 5.7B**). Interestingly, while the PCCell low water transfer and the AGC membranes are marketed for high salinity brine treatment and/or low water transport, they did reduce the overal water transport during EDC operation relative to the standard PCCell membranes (**Figure 5.7C**). However, this water transport had little effect on the crystallization kinetics, where each membrane produced nearly identical TSS at any given time (**Figure 5.7D**). Theoretically, the effect of water transport due to osmosis and electro-osmosis may limit the maximum concentration achievable in the brine stream [270]. However, reduced water transport with the membranes analyzed in this study had little effect on TSS. As such, the standard PCCell membranes were selected for systematic study of crystallization criterion in the following section due to their relatively low energy consumption.

*5.3.3. Crystallization Criterion*

Electrodialysis is a complicated process consisting of several unique transport mechanisms. In an ideal system, salt transport along the applied potential gradient (from the diluate to brine stream) would be the sole transport mechanism. However, due to chemical potential gradients and ion hydration-induced advective transport of water, this is not the case. Chemical potential gradients between the brine and diluate stream result in back diffusion of salt through the ion exchange membrane from the brine to diluate stream, while also causing osmotic water transport through the ion exchange membrane from the diluate to the brine stream (**Figure 5.8**). Both transport mechanisms are undesired as they act against the goal of ED operation and limit the maximum concentration in the brine stream. These chemical potential-induced ion and water transport mechanisms, while undesired, have relatively less effect on the maximum concentration achievable in the brine stream [270–272]. The dominant transport mechanisms in electrodialysis are salt transport due to electromigration and water transport due to electroosmosis from the diluate to the brine stream. These coupled transport mechanisms dictate the ability of EDC to crystallize specific salts.

The fundamental criterion for successful crystallization of a specific salt in EDC is that the molar ratio of salt flux ($J_s$) to water flux ($J_w$) must be greater than the molar ratio of salt to water at the solubility limit for that specific salt, i.e., $J_s/J_w$ > solubility (**Figure 5.8**). Otherwise, the salt in the brine stream will be diluted below the solubility limit and crystals will not form. Salt hydration number ($n_h^{-1}$), or the molar ratio of salt to water associated with the ions' hydrations

shells as they transport through the ion exchange membranes, can serve as a proxy for the salt-water flux ratio. Water transport due to electroosmosis can be thought of as a forced advection of water molecules due to ion-water interaction in the first and second hydration shells. As such, this salt hydration number represents water transport in ED relatively well [272].

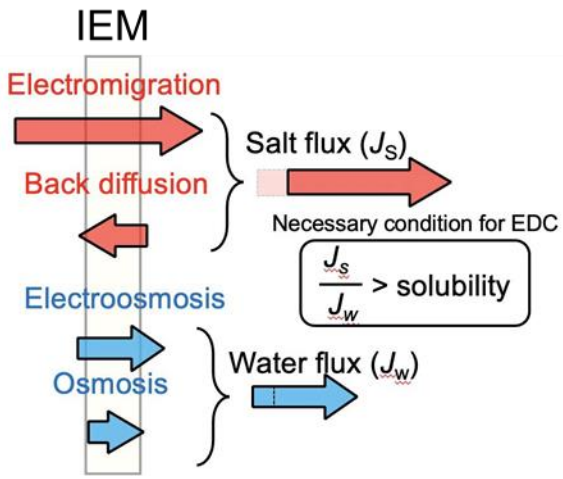


**Figure 5. 8.** Water and ion transport in electrodialysis that dictates the efficacy of EDC in crystallizing specific salts. Ions transport to the brine through the ion exchange membrane (IEM) due to applied potential, i.e., electromigration, while the concentration gradient from the brine to diluate induces back diffusion ion transport from the brine to diluate. Water transport in electrodialysis flows from the diluate to the brine following the potential gradient due to electroosmosis and the chemical potential gradient due to osmosis. Electroosmosis, osmosis, and back diffusion limit the maximum concentration achievable in the brine stream where electromigration is the only desired transport in an ideal EDC system. To achieve successful crystallization of a specific salt with EDC, the salt hydration numbers must be greater than the molar ratio of salt to water at that specific salt's solubility limit at the respective temperature in the crystallizer.

To analyze the EDC system's crystallization capabilities and evaluate our crystallization criterion, we attempted to crystallize several single salt solutions in the EDC system. Of those tested, potassium sulfate, potassium nitrate, sodium carbonate, and sodium sulfate were successfully crystallized with EDC (**Figure 5.9A**). Interestingly, although operating conditions were identical for each single salt experiment, crystallization kinetics varied depending on the salt being studied. For example, the TSS production rate for potassium nitrate was the greatest while it was the least for sodium carbonate. While these salts obviously satisfied the crystallization criterion (**Figure 5.8**), the difference in TSS production rate is related to the relative difference in salt hydration number and the molar ratio of salt to water at the solubility limit (**Figure 5.9B**). For example, the difference between the salt hydration number and the solubility ratio for potassium

nitrate was greatest, 0.034 mole salt mole water$^{-1}$, where the difference for sodium carbonate was only 0.005 mole salt mole water$^{-1}$. Further confirmation of the crystallization criteria was demonstrated by the inability to crystallize sodium chloride, potassium chloride, ammonium chloride, and magnesium sulfate in EDC. The salt hydration number for these salts was less than the solubility ratio, and as such, they were unable to be crystallized (**Figure 5.9C**). Additionally, if we recall the difference in TSS production rates between sodium sulfate at different crystallizer temperatures (**Figure 5.3B**), we can understand that this difference is most likely due to reduced solubility ratio at lower temperature (**Figure 5.9D**).

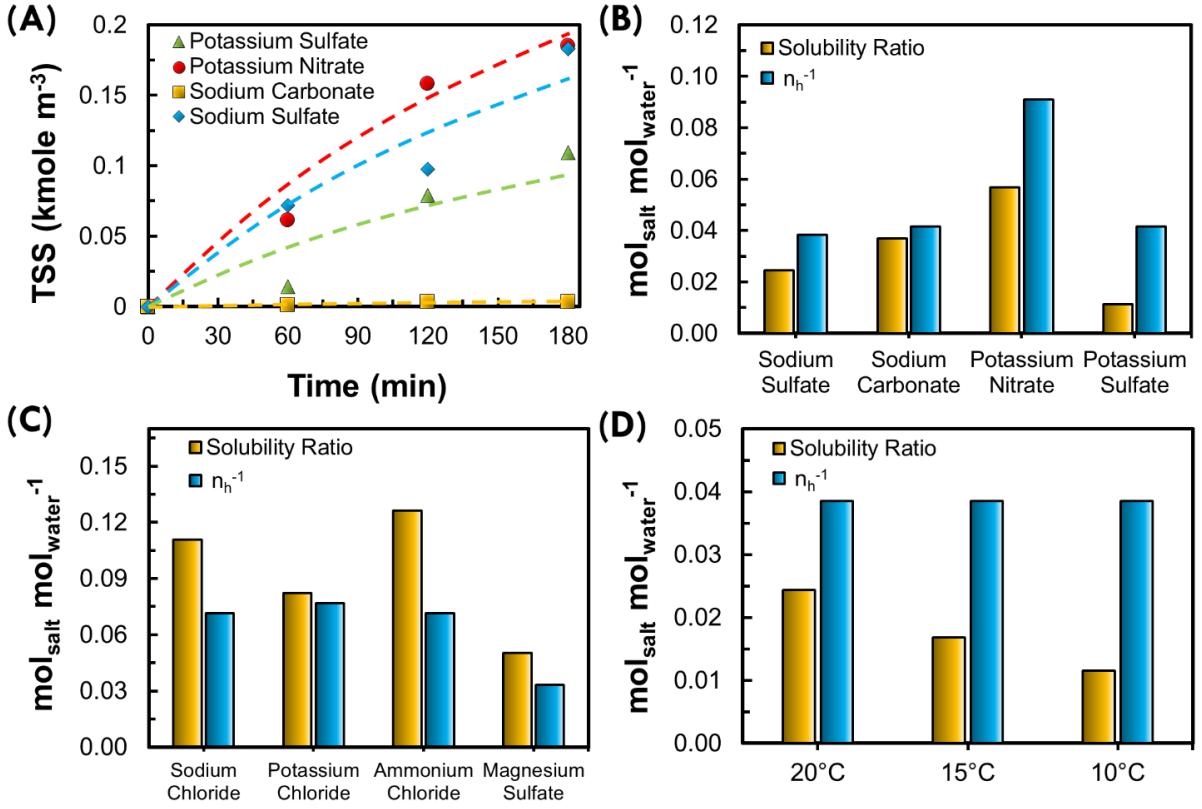


**Figure 5. 9.** (A) Total suspended solids (TSS) production rate in the improved EDC system with common single salts. ED cell configured with 5 cell pairs of the PC SA and PC SK standard desalination ion exchange membranes from PCA GmbH. Applied current density was 35 mA cm$^{-2}$. The initial diluate was 4 L of 0.6 M of the single salt. The initial brine was 1 L of saturated single salt solution at 20°C [269]. The temperature of the brine in the crystallizer was maintained at 18°C. Dashed lines added to guide the eye. (B) Salt hydration number (blue) and molar ratio for salt to water at the solubility limit at 20°C (orange) for the salts that were successfully crystallized in the EDC system. (C) Salt hydration number (blue) and molar ratio for salt to water at the solubility limit at 20°C (orange) for the salts that were not successfully crystallized in the EDC system. (D) Salt hydration number (blue) and molar ratio for salt to water at the solubility limit at 20°C (orange) for sodium sulfate at different crystallizer temperatures from **Fig. 5.3B**. Theoretical salt hydration numbers ($n_h^{-1}$) were calculated based on ionic hydration numbers and water transport from previous ED studies [272–277].

## 5.4. Conclusions and Implications

From this study, we can draw three main conclusions. (1) Crystallization kinetics increase with residence time in the crystallizer and applied current density in the ED unit. This is due to increased salt transport with time and current density from the diluate to the brine, which in turn supersaturates the brine and results and increased crystal production. (2) Integration of microfiltration (MF) unit into the brine loop of the EDC system improved crystallization kinetics and crystal size control. Rejection of solid crystals from the brine loop and ED cell via MF enhanced crystal residence time within the crystallizer. Furthermore, EDC operation with MF integrated into the brine loop offered control over crystal size. In reality, this is a more industrially relevant configuration of the EDC system and gives promise toward practical application. (3) The crystallization criterion, i.e., salt hydration numbers greater than the molar solubility ratio, dictates the ability of EDC to crystallize a specific salt. Furthermore, the relative difference between the two ratios dictates the crystallization kinetics for that specific salt.

Fundamentally, the net flux of salt to the brine stream versus water flux to the brine stream dictates whether the salt can remain at, or above, its solubility limit in the crystallizer and ultimately, whether the salt can precipitate. The crystallization criterion not only indicates which salts can and cannot be crystallized in the EDC system, but also presents room for potential improvement in the EDC process. Tuning crystallizer operating parameters to reduce solubility ratio, i.e., temperature change or addition of solvent with relatively low capacity for dissolution, salts that cannot be crystallized at the conditions investigated in this study have the potential to be crystallized. Likewise, tuning salt hydration numbers via membrane properties or operating conditions, i.e., increased diluate concentration and/or volume or reduction of osmotic and salt permeability of the ion exchange membrane, may allow for salts that were not crystallized in this study to be crystallized in EDC. In addition to its implications on crystallization efficiency, the relative difference between salt hydration numbers and the solubility ratio gives promise for selective crystallization. Taking advantage of this difference will allow for operating parameters to be tuned to precipitate relatively pure mineral crystals from a mixed brine solution or fractionation may allow for multiple pure single salts to be harvested over the duration of the EDC process.

# CHAPTER 6: CONCLUSIONS AND FUTURE WORK

Brine management is an emerging challenge that, with stricter environmental regulation and persistent water stress will become more prevalent in the near future. While conventional wastewater treatment trains terminated with the state-of-the-art desalination technology, reverse osmosis, can recover approximately 50% of freshwater, the norm will soon be zero-liquid discharge (ZLD) where complete separation of freshwater and mineral crystals is achieved. Although the current technologies that can achieve ZLD have pushed toward the practical limits of efficiency, there is still room to improve. Membrane distillation (MD) and electrodialytic-crystallization (EDC) presents an attractive solution that may provide considerable energy savings, modularity, and scalability that conventional downstream ZLD treatment processes cannot.

MD is an attractive option for brine management and ZLD due to its ability to utilize low-grade heat to desalinate high salinity water. However, fouling is a major challenge limiting the practical application of MD. Likewise, due to the high salinity of brine generated in ZLD treatment trains, conventional ZLD unit processes are limited to evaporative methods, where the driving force for water transport is weakly dependent on salinity. Due to the relatively high latent heat of water, the water-to-vapor phase change in these processes results in high energy consumption with evaporative ZLD technologies. Likewise, they are typically not modular as the systems are fabricated from expensive materials that must be sized to meet the end-user's specific needs. EDC is another attractive option for brine management and ZLD as it is fully electrified and modular, offering potential to achieve energy efficient ZLD and mineral crystal recovery in a novel, scalable manner.

In this dissertation, the fundamental mechanisms for membrane fouling in MD are investigated as they relate to surface wetting properties. While it is well-established in MD literature that membrane wetting properties may be tailored to alleviate fouling, the mechanisms for which are not well understood. Herein, we utilize quartz crystal microbalance and colloidal force spectroscopy to elucidate the kinetics and force interactions between model foulants and membranes with various surface properties. A summary of Chapters 2-4, that relate to fouling mitigation in MD are detailed below:

*Chapter 2*: Inspired by the limited understanding of inorganic fouling resistance with superhydrophobic membranes, we fabricated model membrane surfaces to investigate the role of

surface wetting properties on scaling resistance. We employed a well-established solvent exchange method to generate nanobubbles on the surface and in the bulk above these surfaces and utilized quartz crystal microbalance to quantify inorganic fouling, or mineral scaling kinetics. We concluded that regardless of surface wetting properties, the scaling resistance induced by the solvent exchanges was best when nanobubbles were injected into the bulk solution. In terms of surface nanobubbles, interfacial bubble formation reduces the direct liquid-solid contact for mineral crystal deposition. By subjecting the surfaces to solutions with and without dissolved gasses present, we showed that scaling resistance is best with superhydrophobic surfaces when dissolved gasses are present and conditions are conducive to surface or bulk bubble formation, however, without dissolved gasses available to form interfacial bubbles, scaling resistance decreases with increasing surface energy. We showed that bulk nanobubbles can improve the scaling resistance of any surface regardless of wetting properties and that bulk nanobubbles virtually eliminates mineral scaling on superhydrophobic surfaces as bulk bubbles coalesce into the entrained gas layer and maintain its long-term stability. Implications from these findings may help to optimize the combination of surface wetting properties and operating conditions for membrane processes, heat exchangers, and marine structures that are prone to mineral scaling.

*Chapter 3:* We utilize colloidal probe AFM force spectroscopy to investigate the interactions between model membrane surfaces with model organic foulants. We found that hydrophilic surfaces are less prone to organic fouling than hydrophobic surfaces. We also saw that roughness on hydrophobic surfaces increases the strength and characteristic length of the attractive interaction between organic foulants. Alternatively, we found that roughness of hydrophilic surfaces reduces the strength and characteristic length of the attractive interaction. The implications gleaned from this study provide significant insight for fabrication of organic fouling resistant surfaces used membrane separations, heat exchangers, and marine structures.

*Chapter 4:* From the studies in Chapter 2-3, we suggest a practical strategy for fouling mitigation in MD. The strategy combines membrane superhydrophobicity and physical gas purging for highly effective gypsum scaling prevention in MD. We showed that only the synergistic combination, not purging or superhydrophobic membrane alone, enhances membrane scaling resistance. This novel strategy will enable MD to treat hypersaline brine with sustainable performance.

*Chapter 5:* Although MD is modular, and offers potential for energy consumption, and ultimately, lower operating cost for brine management and ZLD, it is still an evaporative process with relatively high energy consumption. As such, we develop a novel, modular, fully-electrified brine management, ZLD, and mineral crystal recovery process that we refer to as EDC. We elucidate the effect of operating parameters, such as current density, crystallizer temperature, and crystallizer residence time on crystallization kinetics in the EDC system. Furthermore, we develop an industrially relevant EDC system that produces mineral crystals with a narrow size distribution, offering potential for distinct crystal size control. Finally, we demonstrate that the ability of EDC to crystallize specific salts depends on a fundamental crystallization criterion that, when satisfied to any extent, offers potential for selective salt crystallization and salt crystal fractionation. The modularity and potential for selective crystallization in EDC has the potential to extend a non-evaporative method for practical brine management, ZLD, and mineral crystal recovery.

*Future Work:* Based on the conclusions from this dissertation, future work can be extended from the following perspectives:

- The fundamental fouling mechanisms in this study were analyzed in simple waters with single model foulants. The studies could be extended to complex mixtures that more closely resemble industrial high salinity brine to confirm the findings still hold in a practical scenario.
- The implications suggested from Chapters 2-3 should be demonstrated in real membrane separation experiments to confirm the validity of the findings, both in simple single foulant wastewaters and in realistic wastewaters with a complex mixture of potential foulants.
- While superhydrophobicity limits inorganic fouling, it tends to promote organic fouling. An anti-fouling strategy that simultaneously prevents inorganic and organic fouling in MD is needed.
- The synergistic inorganic fouling mitigation strategy with purging and membrane superhydrophobicity should be investigated for its applicability to a series of common industrially relevant scalants and investigated to see its effectiveness with organic foulants in single component and mixed component solutions.

- Establish crystallization criteria for a series of commercially available ion exchange membranes to evaluate their potential performance in EDC application.
- Construct a theoretical mass transfer model for EDC to evaluate the theoretical limits of crystal recovery and selective crystallization.
- Evaluate the performance and capabilities of EDC with a feed composed of mixed salts.

# REFERENCES


[1] UNICEF & WHO, Progress on household drinking water, sanitation and hygiene, 2000-2017, (2019) 140. https://washdata.org/sites/default/files/documents/reports/2019-07/jmp-2019-wash-households.pdf.

[2] A.Y. Hoekstra, Water scarcity challenges to business, Nat. Clim. Chang. 2014 45. 4 (2014) 318–320. https://doi.org/10.1038/nclimate2214.

[3] K.N. Alrwis, A.M. Ghanem, O.S. Alnashwan, A.A.M. Al Duwais, S.A.B. Alaagib, N.M. Aldawdahi, Measuring the impact of water scarcity on agricultural economic development in Saudi Arabia, Saudi J. Biol. Sci. 28 (2021) 191–195. https://doi.org/10.1016/J.SJBS.2020.09.038.

[4] A. Kaya, M. Evren Tok, M. Koc, A levelized cost analysis for solar-energy-powered sea water desalination in the Emirate of Abu Dhabi, Sustain. 11 (2019). https://doi.org/10.3390/su11061691.

[5] T. Tong, M. Elimelech, The Global Rise of Zero Liquid Discharge for Wastewater Management: Drivers, Technologies, and Future Directions, Environ. Sci. Technol. 50 (2016) 6846–6855. https://doi.org/10.1021/acs.est.6b01000.

[6] J. Kim, J. Kim, S. Hong, Recovery of water and minerals from shale gas produced water by membrane distillation crystallization, Water Res. 129 (2018) 447–459. https://doi.org/10.1016/j.watres.2017.11.017.

[7] H. Dahmardeh, H.A. Akhlaghi Amiri, S.M. Nowee, Evaluation of mechanical vapor recompression crystallization process for treatment of high salinity wastewater, Chem. Eng. Process. - Process Intensif. 145 (2019) 107682. https://doi.org/10.1016/j.cep.2019.107682.

[8] M.O. Mavukkandy, C.M. Chabib, I. Mustafa, A. Al Ghaferi, F. AlMarzooqi, Brine management in desalination industry: From waste to resources generation, Desalination. 472 (2019) 114187. https://doi.org/10.1016/j.desal.2019.114187.

[9] J.A. Bush, J. Vanneste, E.M. Gustafson, C.A. Waechter, D. Jassby, C.S. Turchi, T.Y. Cath, Prevention and management of silica scaling in membrane distillation using pH adjustment, J. Memb. Sci. 554 (2018) 366–377. https://doi.org/10.1016/j.memsci.2018.02.059.

[10] R.L. McGinnis, N.T. Hancock, M.S. Nowosielski-Slepowron, G.D. McGurgan, Pilot demonstration of the NH3/CO2 forward osmosis desalination process on high salinity brines, Desalination. 312 (2013) 67–74. https://doi.org/10.1016/j.desal.2012.11.032.

[11] Z. Wang, T. Horseman, A.P. Straub, N.Y. Yip, D. Li, M. Elimelech, S. Lin, Pathways and challenges for efficient solar-thermal desalination, Sci. Adv. 5 (2019). https://doi.org/10.1126/sciadv.aax0763.

[12] A. Deshmukh, C. Boo, V. Karanikola, S. Lin, A.P. Straub, T. Tong, D.M. Warsinger, M. Elimelech, Membrane distillation at the water-energy nexus: Limits, opportunities, and challenges, Energy Environ. Sci. 11 (2018) 1177–1196.

https://doi.org/10.1039/c8ee00291f.

[13] K.W. Lawson, D.R. Lloyd, Membrane distillation, J. Memb. Sci. 124 (1997) 1–25. https://doi.org/10.1016/S0376-7388(96)00236-0.

[14] A. Alkhudhiri, N. Darwish, N. Hilal, Membrane distillation: A comprehensive review, Desalination. 287 (2012) 2–18. https://doi.org/10.1016/j.desal.2011.08.027.

[15] D.L. Shaffer, L.H. Arias Chavez, M. Ben-Sasson, S. Romero-Vargas Castrillón, N.Y. Yip, M. Elimelech, Desalination and reuse of high-salinity shale gas produced water: Drivers, technologies, and future directions, Environ. Sci. Technol. 47 (2013) 9569–9583. https://doi.org/10.1021/es401966e.

[16] K. Sardari, P. Fyfe, D. Lincicome, S. Ranil Wickramasinghe, Combined electrocoagulation and membrane distillation for treating high salinity produced waters, J. Memb. Sci. 564 (2018) 82–96. https://doi.org/10.1016/j.memsci.2018.06.041.

[17] Y. Choi, G. Naidu, L.D. Nghiem, S. Lee, S. Vigneswaran, Membrane distillation crystallization for brine mining and zero liquid discharge: Opportunities, challenges, and recent progress, Environ. Sci. Water Res. Technol. 5 (2019) 1202–1221. https://doi.org/10.1039/c9ew00157c.

[18] S. Lin, Energy Efficiency of Desalination: Fundamental Insights from Intuitive Interpretation, Environ. Sci. Technol. (2020). https://doi.org/10.1021/acs.est.9b04788.

[19] L.D. Tijing, Y.C. Woo, J.S. Choi, S. Lee, S.H. Kim, H.K. Shon, Fouling and its control in membrane distillation-A review, J. Memb. Sci. 475 (2015) 215–244. https://doi.org/10.1016/j.memsci.2014.09.042.

[20] K.S.S. Christie, T. Horseman, S. Lin, Energy efficiency of membrane distillation: Simplified analysis, heat recovery, and the use of waste-heat, Environ. Int. 138 (2020) 105588. https://doi.org/10.1016/j.envint.2020.105588.

[21] S. Lin, N.Y. Yip, M. Elimelech, Direct contact membrane distillation with heat recovery: Thermodynamic insights from module scale modeling, J. Memb. Sci. 453 (2014) 498–515. https://doi.org/10.1016/j.memsci.2013.11.016.

[22] L.M. Camacho, L. Dumée, J. Zhang, J. De Li, M. Duke, J. Gomez, S. Gray, Advances in membrane distillation for water desalination and purification applications, Water. 5 (2013) 94–196. https://doi.org/10.3390/w5010094.

[23] D.B. Gingerich, M.S. Mauter, Quantity, Quality, and Availability of Waste Heat from United States Thermal Power Generation, Environ. Sci. Technol. 49 (2015) 8297–8306. https://doi.org/10.1021/es5060989.

[24] M. Gryta, M. Tomaszewska, J. Grzechulska, a. W. Morawski, Membrane distillation of NaCl solution containing natural organic matter, J. Memb. Sci. 181 (2001) 279–287. https://doi.org/10.1016/S0376-7388(00)00582-2.

[25] K. Karakulski, M. Gryta, Water demineralisation by NF/MD integrated processes, Desalination. 177 (2005) 109–119. https://doi.org/10.1016/j.desal.2004.11.018.

[26] F. He, J. Gilron, H. Lee, L. Song, K.K. Sirkar, Potential for scaling by sparingly soluble salts in crossflow DCMD, J. Memb. Sci. 311 (2008) 68–80. https://doi.org/10.1016/j.memsci.2007.11.056.

[27] K.S.S. Christie, Y. Yin, S. Lin, T. Tong, Distinct Behaviors between Gypsum and Silica Scaling in Membrane Distillation, Environ. Sci. Technol. 54 (2020) 568–576. https://doi.org/10.1021/acs.est.9b06023.

[28] M. Gryta, Fouling in direct contact membrane distillation process, J. Memb. Sci. 325 (2008) 383–394. https://doi.org/10.1016/j.memsci.2008.08.001.

[29] D.M. Warsinger, J. Swaminathan, E. Guillen-Burrieza, H.A. Arafat, J.H. Lienhard V, Scaling and fouling in membrane distillation for desalination applications: A review, Desalination. 356 (2015) 294–313. https://doi.org/10.1016/j.desal.2014.06.031.

[30] Z. Wang, S. Lin, Membrane fouling and wetting in membrane distillation and their mitigation by novel membranes with special wettability, Water Res. 112 (2017) 38–47. https://doi.org/http://dx.doi.org/10.1016/j.watres.2017.01.022.

[31] S. Al-Amshawee, M.Y.B.M. Yunus, A.A.M. Azoddein, D.G. Hassell, I.H. Dakhil, H.A. Hasan, Electrodialysis desalination for water and wastewater: A review, Chem. Eng. J. 380 (2020) 122231. https://doi.org/10.1016/J.CEJ.2019.122231.

[32] H. Strathmann, Ion-Exchange Membrane Separation Processes, Membrane S, Elsevier B.V., Stuttgart, Germany, 2004.

[33] S.-C. Chua, M.H. Isa, Y.-C. Ho, Electrodialysis (ED): A review on the fundamental concept, advantages, limitations and future trend, J. Sci. Technol. 3 (2020) 14–22. https://myjms.mohe.gov.my/index.php/pjst/article/view/6146/5706 (accessed April 27, 2022).

[34] H. Strathmann, Electrodialysis, a mature technology with a multitude of new applications, Desalination. 264 (2010) 268–288. https://doi.org/10.1016/J.DESAL.2010.04.069.

[35] A.H. Galama, M. Saakes, H. Bruning, H.H.M. Rijnaarts, J.W. Post, Seawater predesalination with electrodialysis, Desalination. 342 (2014) 61–69. https://doi.org/10.1016/j.desal.2013.07.012.

[36] R. Singh, Desalination and On-site Energy for Groundwater Treatment in Developing Countries Using Fuel Cells, Emerg. Membr. Technol. Sustain. Water Treat. (2016) 135–162. https://doi.org/10.1016/B978-0-444-63312-5.00006-1.

[37] K.M. Chehayeb, D.M. Farhat, K.G. Nayar, J.H. Lienhard, Optimal design and operation of electrodialysis for brackish-water desalination and for high-salinity brine concentration, Desalination. 420 (2017) 167–182. https://doi.org/10.1016/j.desal.2017.07.003.

[38] R.K. McGovern, A.M. Weiner, L. Sun, C.G. Chambers, S.M. Zubair, J.H. Lienhard V, On the cost of electrodialysis for the desalination of high salinity feeds, Appl. Energy. 136 (2014) 649–661. https://doi.org/10.1016/j.apenergy.2014.09.050.

[39] R.K. Mcgovern, S.M. Zubair, J.H. Lienhard, The cost effectiveness of electrodialysis for diverse salinity applications, (2014). https://doi.org/10.1016/j.desal.2014.06.010.

[40] H. Yan, Y. Wang, L. Wu, M.A. Shehzad, C. Jiang, R. Fu, Z. Liu, T. Xu, Multistage-batch electrodialysis to concentrate high-salinity solutions: Process optimisation, water transport, and energy consumption, (2018). https://doi.org/10.1016/j.memsci.2018.10.008.

[41] H. Kawate, K. Miyaso, M. Takiguchi, Energy savings in salt manufacture by ion exchange membrane electrodialysis, in: Sixth Int. Symp. Salt, 1983: pp. 471–479.

[42] M. Turek, Dual-purpose desalination-salt production electrodialysis, Desalination. 153 (2002) 377–415.

[43] E.M.A. Becheleni, R.P. Borba, M.M. Seckler, S.D.F. Rocha, Water recovery from saline streams produced by electrodialysis, Environ. Technol. (United Kingdom). 36 (2015) 386–394. https://doi.org/10.1080/09593330.2014.978898.

[44] M. Turek, P. Dydo, R. Klimek, Salt production from coal-mine brine in ED-evaporation-crystallization system, (n.d.). https://doi.org/10.1016/j.desal.2005.03.047.

[45] T. Horseman, Y. Yin, K.S. Christie, Z. Wang, T. Tong, S. Lin, Wetting, Scaling, and Fouling in Membrane Distillation: State-of-the-Art Insights on Fundamental Mechanisms and Mitigation Strategies, ACS ES&T Eng. 1 (2021) 117–140. https://doi.org/10.1021/acsestengg.0c00025.

[46] A. Herz, M.R. Malayeri, H. Müller-Steinhagen, Fouling of roughened stainless steel surfaces during convective heat transfer to aqueous solutions, Energy Convers. Manag. 49 (2008) 3381–3386. https://doi.org/10.1016/j.enconman.2007.09.034.

[47] A. Al-Janabi, M.R. Malayeri, Innovative non-metal heat transfer surfaces to mitigate crystallization fouling, Int. J. Therm. Sci. 138 (2019) 384–392. https://doi.org/10.1016/j.ijthermalsci.2019.01.003.

[48] A.P. Watkinson, O. Martinez, Scaling of heat exchanger tubes by calcium carbonate, J. Heat Transfer. 97 (1975) 504–508. https://doi.org/10.1115/1.3450419.

[49] C.S. Oon, S.N. Kazi, M.A. Hakimin, A.H. Abdelrazek, A.R. Mallah, F.W. Low, S.K. Tiong, I.A. Badruddin, S. Kamanger, Heat transfer and fouling deposition investigation on the titanium coated heat exchanger surface, Powder Technol. 373 (2020) 671–680. https://doi.org/10.1016/J.POWTEC.2020.07.010.

[50] J.E. Gittens, T.J. Smith, R. Suleiman, R. Akid, Current and emerging environmentally-friendly systems for fouling control in the marine environment, Biotechnol. Adv. 31 (2013) 1738–1753. https://doi.org/10.1016/j.biotechadv.2013.09.002.

[51] R. Deng, T. Shen, H. Chen, J. Lu, H.-C. Yang, W. Li, Slippery liquid-infused porous surfaces (SLIPSs): a perfect solution to both marine fouling and corrosion?, J. Mater. Chem. A. 8 (2020) 7536–7547. https://doi.org/10.1039/d0ta02000a.

[52] J. Genzer, K. Efimenko, Recent developments in superhydrophobic surfaces and their relevance to marine fouling: a review., Biofouling. 22 (2006) 339–360. https://doi.org/10.1080/08927010600980223.

[53] D. Yang, J. Liu, X. E, L. Jiang, Experimental study of composition and influence factors on fouling of stainless steel and copper in seawater, Ann. Nucl. Energy. 94 (2016) 767–

772. https://doi.org/10.1016/j.anucene.2016.04.038.

[54] V.S. Saji, A.A. Meroufel, A.A. Sorour, eds., Corrosion and Fouling Control in Desalination Industry, Springer Nature Switzerland, 2020.

[55] K.S.S. Christie, T. Horseman, R. Wang, C. Su, T. Tong, S. Lin, Gypsum scaling in membrane distillation: Impacts of temperature and vapor flux, Desalination. 525 (2022) 115499. https://doi.org/10.1016/J.DESAL.2021.115499.

[56] N. Andritsos, A.J. Karabelas, Calcium carbonate scaling in a plate heat exchanger in the presence of particles, Int. J. Heat Mass Transf. 46 (2003) 4613–4627. https://doi.org/10.1016/S0017-9310(03)00308-9.

[57] Z. Amjad, Calcium sulfate dihydrate (gypsum) scale formation on heat exchanger surfaces: The influence of scale inhibitors, J. Colloid Interface Sci. 123 (1988) 523–536. https://doi.org/10.1016/0021-9797(88)90274-3.

[58] J.S. Gill, G.H. Nancollas, Kinetics of growth of calcium sulfate crystals at heated metal surfaces, J. Cryst. Growth. 48 (1980) 34–40. https://doi.org/10.1016/0022-0248(80)90190-6.

[59] D. Hasson, J. Zahavi, Mechanism of Calcium Sulfate Scale Deposition on Heat-Transfer Surfaces, Ind. Eng. Chem. Fundam. 9 (1970) 1–10. https://doi.org/10.1021/i160033a001.

[60] N. Abdel-Aal, K. Satoh, K. Sawada, Study of the adhesion mechanism of CaCO3 using a combined bulk chemistry/QCM technique, J. Cryst. Growth. 245 (2002) 87–100. https://doi.org/10.1016/S0022-0248(02)01657-3.

[61] J. MacAdam, S.A. Parsons, Calcium carbonate scale formation and control, 3 (2004) 159–169. http://www.europractice-ic.com/SiPhotonics_general.php.

[62] A. Matin, F. Rahman, H.Z. Shafi, S.M. Zubair, Scaling of reverse osmosis membranes used in water desalination: Phenomena, impact, and control; future directions, Desalination. 455 (2019) 135–157. https://doi.org/10.1016/J.DESAL.2018.12.009.

[63] Q. Liu, G.R. Xu, R. Das, Inorganic scaling in reverse osmosis (RO) desalination: Mechanisms, monitoring, and inhibition strategies, Desalination. 468 (2019) 114065. https://doi.org/10.1016/J.DESAL.2019.07.005.

[64] C. Su, T. Horseman, H. Cao, K. Christie, Y. Li, S. Lin, Robust Superhydrophobic Membrane for Membrane Distillation with Excellent Scaling Resistance, Environ. Sci. Technol. 53 (2019) 11801–11809. https://doi.org/10.1021/acs.est.9b04362.

[65] L. Liu, Z. Xiao, Y. Liu, X. Li, H. Yin, A. Volkov, T. He, Understanding the fouling/scaling resistance of superhydrophobic/omniphobic membranes in membrane distillation, Desalination. 499 (2021) 114864. https://doi.org/10.1016/J.DESAL.2020.114864.

[66] R. Zheng, H. Yin, Y. Liu, H. He, Y. Zhang, X.-M. Li, Y. Ji, Z. Xiao, X. Yuan, T. He, D. Li, Slippery for scaling resistance in membrane distillation: a novel porous micropillared superhydrophobic surface, Water Res. 155 (2019) 152–161. https://doi.org/10.1016/j.watres.2019.01.036.

[67] C. Yang, X.M. Li, J. Gilron, D. feng Kong, Y. Yin, Y. Oren, C. Linder, T. He, CF4plasma-modified superhydrophobic PVDF membranes for direct contact membrane distillation, J. Memb. Sci. 456 (2014) 155–161. https://doi.org/10.1016/j.memsci.2014.01.013.

[68] Y. Xu, Y. Yang, M. Sun, X. Fan, C. Song, P. Tao, M. Shao, High-performance desalination of high-salinity reverse osmosis brine by direct contact membrane distillation using superhydrophobic membranes, J. Appl. Polym. Sci. 138 (2021) 49768. https://doi.org/10.1002/APP.49768.

[69] Z. Zhu, L. Zhong, T. Horseman, Z. Liu, G. Zeng, Z. Li, S. Lin, W. Wang, Superhydrophobic-omniphobic membrane with anti-deformable pores for membrane distillation with excellent wetting resistance, J. Memb. Sci. (2020) 118768. https://doi.org/10.1016/j.memsci.2020.118768.

[70] Y. Lv, M. Liu, Surface Engineering Corrosion and fouling behaviours of copper-based superhydrophobic coating Corrosion and fouling behaviours of copper-based superhydrophobic coating, (2018). https://doi.org/10.1080/02670844.2018.1433774.

[71] Y. Lv, M.Y. Liu, L.F. Hui, A.N. Pavlenko, A.S. Surtaev, V.S. Serdyukov, Heat Transfer and Fouling Rate at Boiling on Superhydrophobic Surface with TiO 2 Nanotube-Array Structure, J. Eng. Thermophys. 28 (2019) 163–176. https://doi.org/10.1134/S1810232819020012.

[72] S.M.A. Mousavi, R. Pitchumani, Temperature-dependent dynamic fouling on superhydrophobic and slippery nonwetting copper surfaces, Chem. Eng. J. 431 (2022) 133960. https://doi.org/10.1016/J.CEJ.2021.133960.

[73] H.S. Ahn, K.M. Kim, S.T. Lim, C.H. Lee, S.W. Han, H. Choi, S. Koo, N. Kim, D.-W. Jerng, S. Wongwises, Anti-fouling performance of chevron plate heat exchanger by the surface modification, Int. J. Heat Mass Transf. 144 (2019). https://reader.elsevier.com/reader/sd/pii/S0017931019316096?token=4FD4F105E4BF8CE66083B636B128CDF37805BEF2E4548A98E91F5EF81A4974A63316A28EAB7F670AB9722C8DA50C0DDF&originRegion=us-east-1&originCreation=20220207151159 (accessed February 7, 2022).

[74] M. Ferrari, A. Benedetti, Superhydrophobic surfaces for applications in seawater, Adv. Colloid Interface Sci. 222 (2015) 291–304. https://doi.org/10.1016/J.CIS.2015.01.005.

[75] P. Lv, Y. Xue, Y. Shi, H. Lin, H. Duan, Metastable states and wetting transition of submerged superhydrophobic structures, Phys. Rev. Lett. 112 (2014) 196101. https://doi.org/10.1103/PHYSREVLETT.112.196101/FIGURES/5/MEDIUM.

[76] E. Bormashenko, R. Pogreb, G. Whyman, M. Erlich, Cassie-Wenzel Wetting Transition in Vibrating Drops Deposited on Rough Surfaces: Is the Dynamic Cassie-Wenzel Wetting Transition a 2D or 1D Affair?, Langmuir. 23 (2007) 6501–6503. https://doi.org/10.1021/la700935x.

[77] M.S. Bobji, S.V. Kumar, A. Asthana, R.N. Govardhan, Underwater Sustainability of the “Cassie” State of Wetting, Langmuir. 25 (2009) 12120–12126. https://doi.org/10.1021/la902679c.

[78] P. Tsai, R.G.H. Lammertink, M. Wessling, D. Lohse, Evaporation-triggered wetting transition for water droplets upon hydrophobic microstructures, Phys. Rev. Lett. 104 (2010) 116102. https://doi.org/10.1103/PHYSREVLETT.104.116102/FIGURES/6/MEDIUM.

[79] A.H. Nikoo, M.R. Malayeri, Incorporation of surface energy properties into general crystallization fouling model for heat transfer surfaces, Chem. Eng. Sci. 215 (2020) 115461. https://doi.org/10.1016/J.CES.2019.115461.

[80] A. Al-Janabi, M.R. Malayeri, A criterion for the characterization of modified surfaces during crystallization fouling based on electron donor component of surface energy, Chem. Eng. Res. Des. 100 (2015) 212–227. https://doi.org/10.1016/J.CHERD.2015.05.033.

[81] A. Al-Janabi, M.R. Malayeri, E. Guillén-Burrieza, J. Blanco, Field evaluation of coated plates of a compact heat exchanger to mitigate crystallization deposit formation in an MD desalination plant, Desalination. 324 (2013) 21–33. https://doi.org/10.1016/J.DESAL.2013.05.020.

[82] S. Bargir, S. Dunn, B. Jefferson, J. Macadam, S. Parsons, The use of contact angle measurements to estimate the adhesion propensity of calcium carbonate to solid substrates in water, Appl. Surf. Sci. 255 (2009) 4873–4879. https://doi.org/10.1016/J.APSUSC.2008.12.017.

[83] J.D. Doyle, K. Oldring, J. Churchley, S.A. Parsons, Struvite formation and the fouling propensity of different materials, Water Res. 36 (2002) 3971–3978. https://doi.org/10.1016/S0043-1354(02)00127-6.

[84] Y. Cai, M. Liu, L. Hui, Observations and mechanism of CaSO4 fouling on hydrophobic surfaces, Ind. Eng. Chem. Res. 53 (2014) 3509–3527. https://doi.org/10.1021/ie402308m.

[85] A. Al-Gailani, O. Sanni, T.V.J. Charpentier, R. Barker, R. Crisp, J.H. Bruins, A. Neville, Role of temperature, roughness and pressure in crystallization fouling from potable water on aluminium surface, Therm. Sci. Eng. Prog. 23 (2021) 100911. https://doi.org/10.1016/J.TSEP.2021.100911.

[86] J.R.T. Seddon, E.S. Kooij, B. Poelsema, H.J.W. Zandvliet, D. Lohse, Surface bubble nucleation stability, Phys. Rev. Lett. 106 (2011) 19–22. https://doi.org/10.1103/PhysRevLett.106.056101.

[87] A.C. Simonsen, P.L. Hansen, B. Klösgen, Nanobubbles give evidence of incomplete wetting at a hydrophobic interface, J. Colloid Interface Sci. 273 (2004) 291–299. https://doi.org/10.1016/j.jcis.2003.12.035.

[88] L. Zargarzadeh, J.A.W. Elliott, Thermodynamics of Surface Nanobubbles, Langmuir. 32 (2016) 11309–11320. https://doi.org/10.1021/acs.langmuir.6b01561.

[89] Y. Liu, X. Zhang, A unified mechanism for the stability of surface nanobubbles: Contact line pinning and supersaturation, J. Chem. Phys. 141 (2014). https://doi.org/10.1063/1.4896937.

[90] D. Lohse, X. Zhang, Surface nanobubbles and nanodroplets, Rev. Mod. Phys. 87 (2015)

981–1035. https://doi.org/10.1103/RevModPhys.87.981.

[91] J.W.G. Tyrrell, P. Attard, Atomic force microscope images of nanobubbles on a hydrophobic surface and corresponding force-separation data, Langmuir. 18 (2002) 160–167. https://doi.org/10.1021/la0111957.

[92] S.T. Lou, Z.Q. Ouyang, Y. Zhang, X.J. Li, J. Hu, M.Q. Li, F.J. Yang, Nanobubbles on solid surface imaged by atomic force microscopy, J. Vac. Sci. Technol. B Microelectron. Nanom. Struct. 18 (2000) 2573–2575. https://doi.org/10.1116/1.1289925.

[93] L. Wang, X. Wang, L. Wang, J. Hu, C.L. Wang, B. Zhao, X. Zhang, R. Tai, M. He, L. Chen, L. Zhang, Formation of surface nanobubbles on nanostructured substrates, Nanoscale. 9 (2017) 1078–1086. https://doi.org/10.1039/c6nr06844h.

[94] M.P. Brenner, D. Lohse, Dynamic Equilibrium Mechanism for Surface Nanobubble Stabilization, (2008). https://doi.org/10.1103/PhysRevLett.101.214505.

[95] B.H. Tan, H. An, C.D. Ohl, Stability of surface and bulk nanobubbles, Curr. Opin. Colloid Interface Sci. 53 (2021) 101428. https://doi.org/10.1016/J.COCIS.2021.101428.

[96] X.H. Zhang, Quartz crystal microbalance study of the interfacial nanobubbles, Phys. Chem. Chem. Phys. 10 (2008) 6842–6848. https://doi.org/10.1039/b810587a.

[97] M. Liu, W. Zhao, S. Wang, W. Guo, Y. Tang, Y. Dong, Study on Nanobubble Generation: Saline Solution/Water Exchange Method, ChemPhysChem. 14 (2013) 2589–2593. https://doi.org/10.1002/cphc.201201032.

[98] J.C. Millare, B.A. Basilia, Nanobubbles from Ethanol-Water Mixtures: Generation and Solute Effects via Solvent Replacement Method, ChemistrySelect. 3 (2018) 9268–9275. https://doi.org/10.1002/SLCT.201801504.

[99] J. Qiu, Z. Zou, S. Wang, X. Wang, L. Wang, Y. Dong, H. Zhao, L. Zhang, J. Hu, Formation and Stability of Bulk Nanobubbles Generated by Ethanol–Water Exchange, ChemPhysChem. 18 (2017) 1345–1350. https://doi.org/10.1002/CPHC.201700010.

[100] D. Li, L. Qi, Y. Liu, B. Bhushan, J. Gu, J. Dong, Study on the Formation and Properties of Trapped Nanobubbles and Surface Nanobubbles by Spontaneous and Temperature Difference Methods, Langmuir. 35 (2019) 12035–12041. https://doi.org/10.1021/ACS.LANGMUIR.9B02058/SUPPL_FILE/LA9B02058_SI_001.PDF.

[101] B. Wang, M. Wang, H. Zhang, N.S. Sobal, W. Tong, C. Gao, Y. Wang, M. Giersig, D. Wang, H. Möhwald, Kinetics of CO2 nanobubble formation at the solid/water interface, Phys. Chem. Chem. Phys. 9 (2007) 6313–6318. https://doi.org/10.1039/b705094a.

[102] J. Tokunaga, Solubilities of Oxygen, Nitrogen, and Carbon Dioxide in Aqueous Alcohol Solutions, J. Chem. Eng. Data. 20 (1975) 54. https://pubs.acs.org/sharingguidelines (accessed February 13, 2022).

[103] A. Schumpe, The estimation of gas solubilities in salt solutions, Chem. Eng. Sci. 48 (1993) 153–158. https://doi.org/10.1016/0009-2509(93)80291-W.

[104] H. Sørensen, K.S. Pedersen, P.L. Christensen, Modeling of gas solubility in brine, Org. Geochem. 33 (2002) 635–642. https://doi.org/10.1016/S0146-6380(02)00022-0.

[105] S. Maheshwari, M. Van Der Hoef, J. Rodrĺguez Rodrĺguez, D. Lohse, Leakiness of Pinned Neighboring Surface Nanobubbles Induced by Strong Gas-Surface Interaction, ACS Nano. 12 (2018) 2603–2609. https://doi.org/10.1021/ACSNANO.7B08614/SUPPL_FILE/NN7B08614_SI_002.AVI.

[106] N.D. Petsev, L.G. Leal, M.S. Shell, Universal Gas Adsorption Mechanism for Flat Nanobubble Morphologies, Phys. Rev. Lett. 125 (2020) 146101. https://doi.org/10.1103/PHYSREVLETT.125.146101/FIGURES/4/MEDIUM.

[107] G.Z. Sauerbrey, The use of quartz oscillators for weighing thin layers and for microweighing, Physics (College. Park. Md). 155 (1959) 206–222.

[108] I. Reviakine, D. Johannsmann, R.P. Richter, Hearing what you cannot see and visualizing what you hear: Interpreting quartz crystal microbalance data from solvated interfaces, Anal. Chem. 83 (2011) 8838–8848. https://doi.org/10.1021/ac201778h.

[109] A. Sheikhi, A.L.J. Olsson, N. Tufenkji, A. Kakkar, T.G.M. van de Ven, Overcoming interfacial scaling using engineered nanocelluloses: A QCM-D study, ACS Appl. Mater. Interfaces. 10 (2018) acsami.8b07435. https://doi.org/10.1021/acsami.8b07435.

[110] G. Liu, V.S.J. Craig, Improved cleaning of hydrophilic protein-coated surfaces using the combination of nanobubbles and SDS, ACS Appl. Mater. Interfaces. 1 (2009) 481–487. https://doi.org/10.1021/am800150p.

[111] G. Liu, Z. Wu, V.S.J. Craig, Cleaning of protein-coated surfaces using nanobubbles: An investigation using a Quartz Crystal Microbalance, J. Phys. Chem. C. 112 (2008) 16748–16753. https://doi.org/10.1021/jp805143c.

[112] W.P. Mason, Viscosity and shear elasticity measurements of liquids by means of shear vibrating crystals, J. Colloid Sci. 3 (1948) 147–162. https://doi.org/10.1016/0095-8522(48)90065-8.

[113] A.P. Borovikov, Measurement of viscocity of media by means of shear vibration of plane piezoresonators, Instruments Exp. Tech. 19 (1976) 223–224.

[114] K.K. Kanazawa, J.G. Gordon, Frequency of a quartz microbalance in contact with liquid, Anal. Chem. 57 (1985) 1770–1771.

[115] M. Holmes, J. Keeley, K. Hurd, H. Schmidt, A. Hawkins, Optimized piranha etching process for SU8-based MEMS and MOEMS construction, J. Micromech. Microeng. 20 (2010) 1. https://doi.org/10.1088/0960-1317/20/11/115008.

[116] T.M. Mayer, M.P. de Boer, N.D. Shinn, P.J. Clews, T.A. Michalske, Chemical vapor deposition of fluoroalkylsilane monolayer films for adhesion control in microelectromechanical systems, J. Vac. Sci. Technol. B Microelectron. Nanom. Struct. Process. Meas. Phenom. 18 (2000) 2433. https://doi.org/10.1116/1.1288200.

[117] J.X.H. Wong, H.Z. Yu, Preparation of transparent superhydrophobic glass slides: Demonstration of surface chemistry characteristics, J. Chem. Educ. 90 (2013) 1203–1206.

https://doi.org/10.1021/ed300809m.

[118] A. Marmur, Wetting on hydrophobic rough surfaces: To be heterogeneous or not to be?, Langmuir. 19 (2003) 8343–8348. https://doi.org/10.1021/la0344682.

[119] A.B.D. Cassie, Contact angles, Discuss. Faraday Soc. 3 (1948) 11. https://doi.org/10.1039/df9480300011.

[120] S. Datta, R. Pillai, M.K. Borg, K. Sefiane, Acoustothermal Nucleation of Surface Nanobubbles, 12 (2022) 33. https://doi.org/10.1021/acs.nanolett.0c03895.

[121] J. Israelachvili, R. Pashley, The hydrophobic interaction is long range, decaying exponentially with distance, Nature. 300 (1982) 341–342. https://doi.org/10.1038/300341a0.

[122] J.R.T. Seddon, D. Lohse, W.A. Ducker, V.S.J. Craig, A deliberation on nanobubbles at surfaces and in bulk, ChemPhysChem. 13 (2012) 2179–2187. https://doi.org/10.1002/cphc.201100900.

[123] N.V.Y. Quach, A. Li, J.C. Earthman, Interaction of Calcium Carbonate with Nanobubbles Produced in an Alternating Magnetic Field, ACS Appl. Mater. Interfaces. 12 (2020) 43714–43719. https://doi.org/10.1021/ACSAMI.0C12060.

[124] M.U. Farid, J.A. Kharraz, C.H. Lee, J.K.H. Fang, S. St-Hilaire, A.K. An, Nanobubble-assisted scaling inhibition in membrane distillation for the treatment of high-salinity brine, Water Res. 209 (2022) 117954. https://doi.org/10.1016/J.WATRES.2021.117954.

[125] A.L. Lim, R. Bai, Membrane fouling and cleaning in microfiltration of activated sludge wastewater, J. Memb. Sci. 216 (2003) 279–290. https://doi.org/10.1016/S0376-7388(03)00083-8.

[126] L. Song, Flux decline in crossflow microfiltration and ultrafiltration: Mechanisms and modeling of membrane fouling, J. Memb. Sci. 139 (1998) 183–200. https://doi.org/10.1016/S0376-7388(97)00263-9.

[127] P. Rajala, M. Bomberg, E. Huttunen-Saarivirta, O. Priha, M. Tausa, L. Carpén, Influence of chlorination and choice of materials on fouling in cooling water system under brackish seawater conditions, Materials (Basel). 9 (2016). https://doi.org/10.3390/ma9060475.

[128] K.M. Bataineh, Multi-effect desalination plant combined with thermal compressor driven by steam generated by solar energy, DES. 385 (2016) 39–52. https://doi.org/10.1016/j.desal.2016.02.011.

[129] M. Lejars, A. Margaillan, C. Bressy, Fouling release coatings: A nontoxic alternative to biocidal antifouling coatings, Chem. Rev. 112 (2012) 4347–4390. https://doi.org/10.1021/cr200350v.

[130] R.F. Brady, Properties which influence marine fouling resistance in polymers containing silicon and fluorine, Prog. Org. Coatings. 35 (1999) 31–35. https://doi.org/10.1016/S0300-9440(99)00005-3.

[131] A.G. Nurioglu, A.C.C. Esteves, G. De With, Non-toxic, non-biocide-release antifouling

coatings based on molecular structure design for marine applications, J. Mater. Chem. B. 3 (2015) 6547–6570. https://doi.org/10.1039/c5tb00232j.

[132] F. Wang, V. V. Tarabara, Pore blocking mechanisms during early stages of membrane fouling by colloids, J. Colloid Interface Sci. 328 (2008) 464–469. https://doi.org/10.1016/j.jcis.2008.09.028.

[133] T.H. Bae, T.M. Tak, Effect of TiO2 nanoparticles on fouling mitigation of ultrafiltration membranes for activated sludge filtration, J. Memb. Sci. 249 (2005) 1–8. https://doi.org/10.1016/j.memsci.2004.09.008.

[134] Z. Wang, D. Hou, S. Lin, Composite Membrane with Underwater-Oleophobic Surface for Anti-Oil-Fouling Membrane Distillation, Environ. Sci. Technol. 50 (2016) 3866–3874. https://doi.org/10.1021/acs.est.5b05976.

[135] F. Meng, S.R. Chae, A. Drews, M. Kraume, H.S. Shin, F. Yang, Recent advances in membrane bioreactors (MBRs): Membrane fouling and membrane material, Water Res. 43 (2009) 1489–1512. https://doi.org/10.1016/j.watres.2008.12.044.

[136] K. Chon, S. Sarp, S. Lee, J.H. Lee, J.A. Lopez-Ramirez, J. Cho, Evaluation of a membrane bioreactor and nanofiltration for municipal wastewater reclamation: Trace contaminant control and fouling mitigation, Desalination. 272 (2011) 128–134. https://doi.org/10.1016/j.desal.2011.01.002.

[137] Z. Wang, Z. Wu, X. Yin, L. Tian, Membrane fouling in a submerged membrane bioreactor (MBR) under sub-critical flux operation: Membrane foulant and gel layer characterization, J. Memb. Sci. 325 (2008) 238–244. https://doi.org/10.1016/j.memsci.2008.07.035.

[138] W. Wang, X. Du, H. Vahabi, S. Zhao, Y. Yin, A.K. Kota, T. Tong, Trade-off in membrane distillation with monolithic omniphobic membranes, Nat. Commun. 10 (2019) 1–9. https://doi.org/10.1038/s41467-019-11209-6.

[139] P. Rajala, E. Sohlberg, O. Priha, I. Tsitko, H. Väisänen, M. Tausa, L. Carpén, Biofouling on coated carbon steel in cooling water cycles using brackish seawater, J. Mar. Sci. Eng. 4 (2016). https://doi.org/10.3390/jmse4040074.

[140] S. Lee, J. Cho, M. Elimelech, Combined influence of natural organic matter (NOM) and colloidal particles on nanofiltration membrane fouling, J. Memb. Sci. 262 (2005) 27–41. https://doi.org/10.1016/j.memsci.2005.03.043.

[141] S. Hong, M. Elimelech, Chemical and physical aspects of natural organic matter (NOM) fouling of nanofiltration membranes, J. Memb. Sci. 132 (1997) 159–181. https://doi.org/10.1016/S0376-7388(97)00060-4.

[142] T. Mohammadi, M. Kazemimoghadam, M. Saadabadi, Modeling of membrane fouling and flux decline in reverse osmosis during separation of oil in water emulsions, Desalination. 157 (2003) 369–375. https://doi.org/10.1016/S0011-9164(03)00419-3.

[143] I.M.A. Elsherbiny, A.S.G. Khalil, M. Ulbricht, Influence of surface micro-patterning and hydrogel coating on colloidal silica fouling of polyamide thin-film composite membranes, Membranes (Basel). 9 (2019). https://doi.org/10.3390/membranes9060067.

[144] D. Ferrando, D. Toubiana, N.S. Kandiyote, T.H. Nguyen, A. Nejidat, M. Herzberg, Ambivalent role of calcium in the viscoelastic properties of extracellular polymeric substances and the consequent fouling of reverse osmosis membranes, Desalination. 429 (2018) 12–19. https://doi.org/10.1016/j.desal.2017.12.006.

[145] S. Shao, H. Liang, F. Qu, K. Li, H. Chang, H. Yu, G. Li, Combined influence by humic acid (HA) and powdered activated carbon (PAC) particles on ultrafiltration membrane fouling, J. Memb. Sci. 500 (2016) 99–105. https://doi.org/10.1016/j.memsci.2015.11.036.

[146] C. Combe, E. Molis, P. Lucas, R. Riley, M.M. Clark, The effect of CA membrane properties on adsorptive fouling by humic acid, J. Memb. Sci. 154 (1999) 73–87. https://doi.org/10.1016/S0376-7388(98)00268-3.

[147] T. Knoell, J. Safarik, T. Cormack, R. Riley, S.W. Lin, H. Ridgway, Biofouling potentials of microporous polysulfone membranes containing a sulfonated polyether-ethersulfone/polyethersulfone block copolymer: Correlation of membrane surface properties with bacterial attachment, J. Memb. Sci. 157 (1999) 117–138. https://doi.org/10.1016/S0376-7388(98)00365-2.

[148] X. Zhu, M. Elimelech, Colloidal fouling of reverse osmosis membranes: Measurements and fouling mechanisms, Environ. Sci. Technol. 31 (1997) 3654–3662. https://doi.org/10.1021/es970400v.

[149] Y. Li, S. Shi, H. Cao, Z. Zhao, C. Su, H. Wen, Improvement of the antifouling performance and stability of an anion exchange membrane by surface modi fi cation with graphene oxide ( GO ) and polydopamine ( PDA ), J. Memb. Sci. 566 (2018) 44–53. https://doi.org/10.1016/j.memsci.2018.08.054.

[150] G. Mustafa, K. Wyns, S. Janssens, A. Buekenhoudt, V. Meynen, Evaluation of the fouling resistance of methyl grafted ceramic membranes for inorganic foulants and co-effects of organic foulants, Sep. Purif. Technol. 193 (2018) 29–37. https://doi.org/10.1016/j.seppur.2017.11.015.

[151] R.R. Choudhury, J.M. Gohil, S. Mohanty, S.K. Nayak, Antifouling, fouling release and antimicrobial materials for surface modification of reverse osmosis and nanofiltration membranes, J. Mater. Chem. A. 6 (2018) 313–333. https://doi.org/10.1039/c7ta08627j.

[152] C. Boo, S. Hong, M. Elimelech, Relating Organic Fouling in Membrane Distillation to Intermolecular Adhesion Forces and Interfacial Surface Energies, Environ. Sci. Technol. 52 (2018) 14198–14207. https://doi.org/10.1021/acs.est.8b05768.

[153] E.M. Vrijenhoek, S. Hong, M. Elimelech, Influence of membrane surface properties on initial rate of colloidal fouling of reverse osmosis and nanofiltration membranes, J. Memb. Sci. 188 (2001) 115–128. https://doi.org/10.1016/S0376-7388(01)00376-3.

[154] E.M. V Hoek, S. Bhattacharjee, M. Elimelech, Effect of membrane surface roughness on colloid-membrane DLVO interactions, Langmuir. 19 (2003) 4836–4847. https://doi.org/10.1021/la027083c.

[155] Q. Li, Z. Xu, I. Pinnau, Fouling of reverse osmosis membranes by biopolymers in wastewater secondary effluent: Role of membrane surface properties and initial permeate

flux, J. Memb. Sci. 290 (2007) 173–181. https://doi.org/10.1016/j.memsci.2006.12.027.

[156] D. Rana, T. Matsuura, Surface modifications for antifouling membranes, Chem. Rev. 110 (2010) 2448–2471. https://doi.org/10.1021/cr800208y.

[157] L. Yan, Y.S. Li, C.B. Xiang, S. Xianda, Effect of nano-sized Al2O3-particle addition on PVDF ultrafiltration membrane performance, J. Memb. Sci. 276 (2006) 162–167. https://doi.org/10.1016/j.jsb.2006.03.024.

[158] F. Li, J. Meng, J. Ye, B. Yang, Q. Tian, C. Deng, Surface modification of PES ultrafiltration membrane by polydopamine coating and poly(ethylene glycol) grafting: Morphology, stability, and anti-fouling, Desalination. 344 (2014) 422–430. https://doi.org/10.1016/j.desal.2014.04.011.

[159] R. Zhang, Y. Li, Y. Su, X. Zhao, Y. Liu, X. Fan, T. Ma, Z. Jiang, Engineering amphiphilic nanofiltration membrane surfaces with a multi-defense mechanism for improved antifouling performances, J. Mater. Chem. A. 4 (2016) 7892–7902. https://doi.org/10.1039/C6TA02885C.

[160] D. Hou, K.S.S. Christie, K. Wang, M. Tang, D. Wang, J. Wang, Biomimetic superhydrophobic membrane for membrane distillation with robust wetting and fouling resistance, J. Memb. Sci. 599 (2020) 117708. https://doi.org/10.1016/j.memsci.2019.117708.

[161] X. Lu, Y. Peng, L. Ge, R. Lin, Z. Zhu, S. Liu, Amphiphobic PVDF composite membranes for anti-fouling direct contact membrane distillation, J. Memb. Sci. 505 (2016) 61–69. https://doi.org/10.1016/j.memsci.2015.12.042.

[162] H. Shan, J. Liu, X. Li, Y. Li, F.H. Tezel, B. Li, S. Wang, Nanocoated amphiphobic membrane for flux enhancement and comprehensive anti-fouling performance in direct contact membrane distillation, J. Memb. Sci. 567 (2018) 166–180. https://doi.org/10.1016/j.memsci.2018.09.038.

[163] W. Zhang, Y. Li, J. Liu, B. Li, S. Wang, Fabrication of hierarchical poly (vinylidene fluoride) micro/nano-composite membrane with anti-fouling property for membrane distillation, J. Memb. Sci. 535 (2017) 258–267. https://doi.org/10.1016/j.memsci.2017.04.051.

[164] Z. Wang, D. Hou, S. Lin, Composite Membrane with Underwater-Oleophobic Surface for Anti-Oil-Fouling Membrane Distillation, Environ. Sci. Technol. (2016) acs.est.5b05976. https://doi.org/10.1021/acs.est.5b05976.

[165] G. Zuo, R. Wang, Novel membrane surface modification to enhance anti-oil fouling property for membrane distillation application, J. Memb. Sci. 447 (2013) 26–35. https://doi.org/10.1016/j.memsci.2013.06.053.

[166] K. Wang, D. Hou, J. Wang, Z. Wang, B. Tian, P. Liang, Hydrophilic surface coating on hydrophobic PTFE membrane for robust anti-oil-fouling membrane distillation, Appl. Surf. Sci. 450 (2018) 57–65. https://doi.org/10.1016/j.apsusc.2018.04.180.

[167] D. Hou, Z. Wang, K. Wang, J. Wang, S. Lin, Composite membrane with electrospun multiscale-textured surface for robust oil-fouling resistance in membrane distillation, J.

Memb. Sci. 546 (2018) 179–187. https://doi.org/10.1016/j.memsci.2017.10.017.

[168] S. Meng, Y. Ye, J. Mansouri, V. Chen, Fouling and crystallisation behaviour of superhydrophobic nano-composite PVDF membranes in direct contact membrane distillation, J. Memb. Sci. 463 (2014) 102–112. https://doi.org/10.1016/j.memsci.2014.03.027.

[169] M. Khayet, A. Velázquez, J.I. Mengual, Direct contact membrane distillation of humic acid solutions, J. Memb. Sci. 240 (2004) 123–128. https://doi.org/10.1016/j.memsci.2004.04.018.

[170] A. Bogler, S. Lin, E. Bar-Zeev, Biofouling of membrane distillation, forward osmosis and pressure retarded osmosis: Principles, impacts and future directions, J. Memb. Sci. 542 (2017) 378–398. https://doi.org/10.1016/j.memsci.2017.08.001.

[171] E. Bar-Zeev, U. Passow, S. Romero-Vargas Castrillón, M. Elimelech, Transparent exopolymer particles: From aquatic environments and engineered systems to membrane biofouling, Environ. Sci. Technol. 49 (2015) 691–707. https://doi.org/10.1021/es5041738.

[172] S.H. Flint, P.J. Bremer, J. Brooks, Biofilms in dairy manufacturing plant - description , current concerns and methods of control, Biofouling J. Bioadhesion Biofilm Res. 11:1 (1997) 81–97.

[173] R.L. Fletcher, M.E. Callow, The settlement, attachment and establishment of marine algal spores, Br. Phycol. J. 27 (1992) 303–329. https://doi.org/10.1080/00071619200650281.

[174] D. Howell, B. Behrends, A review of surface roughness in antifouling coatings illustrating the importance of cutoff length, Biofouling. 22 (2006) 401–410. https://doi.org/10.1080/08927010601035738.

[175] S. García, A. Trueba, L.M. Vega, E. Madariaga, Impact of the surface roughness of AISI 316L stainless steel on biofilm adhesion in a seawater-cooled tubular heat exchanger-condenser, Biofouling. 32 (2016) 1185–1193. https://doi.org/10.1080/08927014.2016.1241875.

[176] A.J. Scardino, E. Harvey, R. De Nys, Testing attachment point theory: Diatom attachment on microtextured polyimide biomimics, Biofouling. 22 (2006) 55–60. https://doi.org/10.1080/08927010500506094.

[177] A.J. Scardino, J. Guenther, R. de Nys, Attachment point theory revisited: the fouling response to a microtextured matrix., Biofouling. 24 (2008) 45–53. https://doi.org/10.1080/08927010701784391.

[178] M.L. Carman, T.G. Estes, A.W. Feinberg, J.F. Schumacher, W. Wilkerson, L.H. Wilson, M.E. Callow, J.A. Callow, A.B. Brennan, Engineered antifouling microtopographies - Correlating wettability with cell attachment, Biofouling. 22 (2006) 11–21. https://doi.org/10.1080/08927010500484854.

[179] L. Hoipkemeier-Wilson, J.F. Schumacher, M.L. Carman, A.L. Gibson, A.W. Feinberg, M.E. Callow, J.A. Finlay, J.A. Callow, A.B. Brennan, Antifouling potential of lubricious, micro-engineered, PDMS elastomers against zoospores of the green fouling alga Ulva (Enteromorpha), Biofouling. 20 (2004) 53–63.

https://doi.org/10.1080/08927010410001662689.

[180] D.Z. Liu, S. Jindal, J. Amamcharla, S. Anand, L. Metzger, Short communication: Evaluation of a sol-gel–based stainless steel surface modification to reduce fouling and biofilm formation during pasteurization of milk, J. Dairy Sci. 100 (2017) 2577–2581. https://doi.org/10.3168/jds.2016-12141.

[181] S. Jindal, S. Anand, K. Huang, J. Goddard, L. Metzger, J. Amamcharla, Evaluation of modified stainless steel surfaces targeted to reduce biofilm formation by common milk sporeformers, J. Dairy Sci. 99 (2016) 9502–9513. https://doi.org/10.3168/jds.2016-11395.

[182] W. Stöber, A. Fink, Controlled Growth of Monodisperse Silica Spheres in the Micron Size Range, J. Colloid Interface Sci. 26 (1968) 62–69. https://doi.org/10.1589/jpts.29.112.

[183] A. Papra, N. Gadegaard, N.B. Larsen, Characterization of ultrathin poly(ethylene glycol) monolayers on silicon substrates, Langmuir. 17 (2001) 1457–1460. https://doi.org/10.1021/la000609d.

[184] C. Boo, J. Lee, M. Elimelech, Omniphobic Polyvinylidene Fluoride (PVDF) Membrane for Desalination of Shale Gas Produced Water by Membrane Distillation, Environ. Sci. Technol. 50 (2016) 12275–12282. https://doi.org/10.1021/acs.est.6b03882.

[185] Q. Li, M. Elimelech, Organic fouling and chemical cleaning of nanofiltration membranes: Measurements and mechanisms, Environ. Sci. Technol. 38 (2004) 4683–4693. https://doi.org/10.1021/es0354162.

[186] S. Assemi, J. Nalaskowski, W.P. Johnson, Direct force measurements between carboxylate-modified latex microspheres and glass using atomic force microscopy, Colloids Surfaces A Physicochem. Eng. Asp. 286 (2006) 70–77. https://doi.org/10.1016/j.colsurfa.2006.03.024.

[187] A. Filby, M. Plaschke, H. Geckeis, AFM force spectroscopy study of carboxylated latex colloids interacting with mineral surfaces, Colloids Surfaces A Physicochem. Eng. Asp. 414 (2012) 400–414. https://doi.org/10.1016/j.colsurfa.2012.08.040.

[188] A. V. Nguyen, J. Nalaskowski, J.D. Miller, H.J. Butt, Attraction between hydrophobic surfaces studied by atomic force microscopy, Int. J. Miner. Process. 72 (2003) 215–225. https://doi.org/10.1016/S0301-7516(03)00100-5.

[189] A. Seidel, M. Elimelech, Coupling between chemical and physical interactions in natural organic matter (NOM) fouling of nanofiltration membranes: Implications for fouling control, J. Memb. Sci. 203 (2002) 245–255. https://doi.org/10.1016/S0376-7388(02)00013-3.

[190] A.R. Costa, M.N. de Pinho, M. Elimelech, Mechanisms of colloidal natural organic matter fouling in ultrafiltration, J. Memb. Sci. 281 (2006) 716–725. https://doi.org/10.1016/j.memsci.2006.04.044.

[191] S. Lee, M. Elimelech, Relating organic fouling of reverse osmosis membranes to intermolecular adhesion forces, Environ. Sci. Technol. 40 (2006) 980–987. https://doi.org/10.1021/es051825h.

[192] R.J. Hunter, Foundations of Colloid Science (2nd Edition), Oxford University Press, 2001.

[193] J. Israelachvili, Intermolecular and Surface Forces, 3rd ed., Elsevier Inc, Waltham, MA, 2011.

[194] M. Elimelech, J. Gregory, X. Jia, Particle Deposition and Aggregation: Measurement, Modelling and Simulation, 2013.

[195] J. Drelich, E. Chibowski, Superhydrophilic and superwetting surfaces: Definition and mechanisms of control, Langmuir. 26 (2010) 18621–18623. https://doi.org/10.1021/la1039893.

[196] R.N. Wenzel, Surface Roughness and Contact Angle, J. Phys. Colloid Chem. 53 (1949) 1466–1467. https://doi.org/10.1021/j150474a015.

[197] T. Horseman, C. Su, K.S.S. Christie, S. Lin, Highly effective scaling mitigation in membrane distillation using a superhydrophobic membrane with gas purging, Environ. Sci. Technol. Lett. 6 (2019) 423–429. https://doi.org/10.1021/acs.estlett.9b00354.

[198] vasiliki Karanikola, C. Boo, J. Rolf, M. Elimelech, Engineered Slippery Surface to Mitigate Gypsum Scaling in Membrane Distillation for Treatment of Hypersaline Industrial Wastewaters, Environ. Sci. Technol. 52 (2018) 14362–14370. https://doi.org/10.1021/acs.est.8b04836.

[199] L. Xu, R.G. Karunakaran, J. Guo, S. Yang, Transparent, Superhydrophobic Surfaces from One-Step Spin Coating of Hydrophobic Nanoparticles, (2012). https://doi.org/10.1021/am201750h.

[200] M. Hikita, K. Tanaka, T. Nakamura, T. Kajiyama, A. Takahara, Super-liquid-repellent surfaces prepared by colloidal silica nanoparticles covered with fluoroalkyl groups, Langmuir. 21 (2005) 7299–7302. https://doi.org/10.1021/la050901r.

[201] J. Li, S. Guo, Z. Xu, J. Li, Z. Pan, Z. Du, F. Cheng, Preparation of omniphobic PVDF membranes with silica nanoparticles for treating coking wastewater using direct contact membrane distillation: Electrostatic adsorption vs. chemical bonding, J. Memb. Sci. 574 (2019) 349–357. https://doi.org/10.1016/j.memsci.2018.12.079.

[202] Y. Liao, C.H. Loh, R. Wang, A.G. Fane, Electrospun superhydrophobic membranes with unique structures for membrane distillation, ACS Appl. Mater. Interfaces. 6 (2014) 16035–16048. https://doi.org/10.1021/am503968n.

[203] R.M. Pashley, Hydration forces between mica surfaces in aqueous electrolyte solutions, J. Colloid Interface Sci. 80 (1981) 153–162. https://doi.org/10.1016/0021-9797(81)90171-5.

[204] S. Chen, L. Li, C. Zhao, J. Zheng, Surface hydration: Principles and applications toward low-fouling/nonfouling biomaterials, Polymer (Guildf). 51 (2010) 5283–5293. https://doi.org/10.1016/j.polymer.2010.08.022.

[205] Y. Tsao, D. Evans, H. Wennerstrom, Long-range attractive force between hydrophobic surfaces observed by atomic force microscopy, Science. 262 (1993) 547–550. https://doi.org/10.1126/science.8211182.

[206] E.E. Meyer, K.J. Rosenberg, J. Israelachvili, Recent progress in understanding hydrophobic interactions., Proc. Natl. Acad. Sci. U. S. A. 103 (2006) 15739–15746. https://doi.org/10.1073/pnas.0606422103.

[207] D.M. Warsinger, J. Swaminathan, E. Guillen-Burrieza, H. a. Arafat, J.H. Lienhard V, Scaling and fouling in membrane distillation for desalination applications: A review, Desalination. 356 (2014) 294–313. https://doi.org/10.1016/j.desal.2014.06.031.

[208] H.J. Butt, Measuring electrostatic, van der Waals, and hydration forces in electrolyte solutions with an atomic force microscope., Biophys. J. 60 (1991) 1438–1444. https://doi.org/10.1016/S0006-3495(91)82180-4.

[209] W.A. Ducker, T.J. Senden, R.M. Pashley, Measurement of forces in liquids using a force microscope, Langmuir. 8 (1992) 1831–1836. https://doi.org/10.1021/la00043a024.

[210] S. Veeramasuneni, M.R. Yalamanchili, J.D. Miller, Measurement of interaction forces between silica and α-alumina by atomic force microscopy, J. Colloid Interface Sci. 184 (1996) 594–600. https://doi.org/10.1006/jcis.1996.0656.

[211] A. Faghihnejad, H. Zeng, Interaction mechanism between hydrophobic and hydrophilic surfaces: Using polystyrene and mica as a model system, Langmuir. 29 (2013) 12443–12451. https://doi.org/10.1021/la402244h.

[212] D.J. Babu, M. Mail, W. Barthlott, J.J. Schneider, Superhydrophobic Vertically Aligned Carbon Nanotubes for Biomimetic Air Retention under Water (Salvinia Effect), Adv. Mater. Interfaces. 4 (2017) 1–6. https://doi.org/10.1002/admi.201700273.

[213] J.H. Lee, J.C. Meredith, Non-DLVO silica interaction forces in NMP-water mixtures. II. An asymmetric system, Langmuir. 27 (2011) 10000–10006. https://doi.org/10.1021/la202176u.

[214] A.P. Serro, R. Colaço, B. Saramago, Adhesion forces in liquid media: Effect of surface topography and wettability, J. Colloid Interface Sci. 325 (2008) 573–579. https://doi.org/10.1016/j.jcis.2008.05.032.

[215] H. Seo, M. Yoo, S. Jeon, Influence of nanobubbles on the adsorption of nanoparticles, Langmuir. 23 (2007) 1623–1625. https://doi.org/10.1021/la062763r.

[216] A. Carambassis, L.C. Jonker, P. Attard, M.W. Rutland, Forces measured between hydrophobic surfaces due to a submicroscopic bridging bubble, Phys. Rev. Lett. 80 (1998) 5357–5360. https://doi.org/10.1103/PhysRevLett.80.5357.

[217] A.M. Smith, M. Borkovec, G. Trefalt, Forces between solid surfaces in aqueous electrolyte solutions, Adv. Colloid Interface Sci. 275 (2020) 102078. https://doi.org/10.1016/j.cis.2019.102078.

[218] N. Daems, S. Milis, R. Verbeke, A. Szymczyk, P.P. Pescarmona, I.F.J. Vankelecom, High-performance membranes with full pH-stability, RSC Adv. 8 (2018) 8813–8827. https://doi.org/10.1039/c7ra13663c.

[219] G. Werner, H. Körber, R. Zimmermann, S. Dukhin, H.J. Jacobasch, Extended electrokinetic characterization of flat solid surfaces, J. Colloid Interface Sci. 208 (1998)

329–346. https://doi.org/10.1006/jcis.1998.5787.

[220] T. Xu, R. Fu, L. Yan, A new insight into the adsorption of bovine serum albumin onto porous polyethylene membrane by zeta potential measurements, FTIR analyses, and AFM observations, J. Colloid Interface Sci. 262 (2003) 342–350. https://doi.org/10.1016/S0021-9797(03)00208-X.

[221] H. Al-Shehri, T.S. Horozov, V.N. Paunov, Adsorption of carboxylic modified latex particles at liquid interfaces studied by the gel trapping technique, Soft Matter. 10 (2014) 6433–6441. https://doi.org/10.1039/c4sm01030b.

[222] K.E. Cooksey, B. Wigglesworth-Cooksey, Adhesion of bacteria and diatoms to surfaces in the sea: A review, Aquat. Microb. Ecol. 9 (1995) 87–96. https://doi.org/10.3354/ame009087.

[223] M. Fletcher, G.I. Loeb, Influence of Substratum Characteristics on the Attachment of a Marine Pseudomonad to Solid Surfaces, Appl. Environ. Microbiol. 37 (1979) 67–72. https://doi.org/10.1128/aem.37.1.67-72.1979.

[224] S. Holberg, R. Losada, F.H. Blaikie, H.H.W.B. Hansen, S. Soreau, R.C.A. Onderwater, Hydrophilic silicone coatings as fouling release: Simple synthesis, comparison to commercial, marine coatings and application on fresh water-cooled heat exchangers, Mater. Today Commun. 22 (2020) 100750. https://doi.org/10.1016/j.mtcomm.2019.100750.

[225] A.M.S. El Din, M.E. El-Dahshan, A.M.T. El Din, Bio-film formation on stainless steels part 2. The role of seasonal changes, seawater composition and surface roughness, Desalination. 154 (2003) 267–276. https://doi.org/10.1016/S0011-9164(03)80042-5.

[226] M.I. Baoxia, M. Elimelech, Gypsum scaling and cleaning in forward osmosis: Measurements and mechanisms, Environ. Sci. Technol. 44 (2010) 2022–2028. https://doi.org/10.1021/es903623r.

[227] B. Mi, M. Elimelech, Organic fouling of forward osmosis membranes: Fouling reversibility and cleaning without chemical reagents, J. Memb. Sci. 348 (2010) 337–345. https://doi.org/10.1016/j.memsci.2009.11.021.

[228] C. Shi, D.Y.C. Chan, Q. Liu, H. Zeng, Probing the Hydrophobic Interaction between Air Bubbles and Partially Hydrophobic Surfaces Using Atomic Force Microscopy, (2014).

[229] G. Chen, Y. Lu, W.B. Krantz, R. Wang, A.G. Fane, Optimization of operating conditions for a continuous membrane distillation crystallization process with zero salty water discharge, J. Memb. Sci. 450 (2014) 1–11. https://doi.org/10.1016/j.memsci.2013.08.034.

[230] I. Ruiz Salmón, P. Luis, Membrane crystallization via membrane distillation, Chem. Eng. Process. - Process Intensif. 123 (2018) 258–271. https://doi.org/10.1016/j.cep.2017.11.017.

[231] R. Creusen, J. van Medevoort, M. Roelands, A. van Renesse van Duivenbode, J.H. Hanemaaijer, R. van Leerdam, Integrated membrane distillation-crystallization: Process design and cost estimations for seawater treatment and fluxes of single salt solutions, Desalination. 323 (2013) 8–16. https://doi.org/10.1016/j.desal.2013.02.013.

[232] F. Edwie, T.S. Chung, Development of simultaneous membrane distillation-crystallization (SMDC) technology for treatment of saturated brine, Chem. Eng. Sci. 98 (2013) 160–172. https://doi.org/10.1016/j.ces.2013.05.008.

[233] M.S. El-Bourawi, Z. Ding, R. Ma, M. Khayet, A framework for better understanding membrane distillation separation process, J. Memb. Sci. 285 (2006) 4–29. https://doi.org/10.1016/j.memsci.2006.08.002.

[234] A. Deshmukh, C. Boo, V. Karanikola, S. Lin, A.P. Straub, T. Tong, D.M. Warsinger, M. Elimelech, Membrane Distillation at the Water-Energy Nexus: Limits, Opportunities, and Challenges, Energy Environ. Sci. (2018). https://doi.org/10.1039/C8EE00291F.

[235] A.M. Alklaibi, N. Lior, Membrane-distillation desalination: Status and potential, Desalination. 171 (2005) 111–131. https://doi.org/10.1016/j.desal.2004.03.024.

[236] S. Lin, S. Nejati, C. Boo, Y. Hu, C.O. Osuji, M. Elimelech, Omniphobic Membrane for Robust Membrane Distillation, Environ. Sci. Technol. Lett. 1 (2014) 443–447. https://doi.org/10.1021/ez500267p.

[237] D.M. Warsinger, J. Swaminathan, E. Guillen-burrieza, H.A. Arafat, J.H.L. V, Scaling and fouling in membrane distillation for desalination applications : A review, Desalination. 356 (2015) 294–313. https://doi.org/10.1016/j.desal.2014.06.031.

[238] D.L. Shaffer, L.H. Arias Chavez, M. Ben-Sasson, S. Romero-Vargas Castrillón, N.Y. Yip, M. Elimelech, Desalination and reuse of high-salinity shale gas produced water: drivers, technologies, and future directions., Environ. Sci. Technol. 47 (2013) 9569–83. https://doi.org/10.1021/es401966e.

[239] D.M. Warsinger, A. Servi, S. Van Belleghem, J. Gonzalez, J. Swaminathan, J. Kharraz, H.W. Chung, H.A. Arafat, K.K. Gleason, J.H. Lienhard V, Combining air recharging and membrane superhydrophobicity for fouling prevention in membrane distillation, J. Memb. Sci. 505 (2016) 241–252. https://doi.org/10.1016/j.memsci.2016.01.018.

[240] D.L. Shaffer, M.E. Tousley, M. Elimelech, Influence of polyamide membrane surface chemistry on gypsum scaling behavior, J. Memb. Sci. 525 (2017) 249–256. https://doi.org/10.1016/j.memsci.2016.11.003.

[241] E. Pouget, P. Bomans, J. Goos, P. Frederik, G. de With, N.A.J.M. Sommerdijk, The Initial Stages of Template-Controlled CaCO3 Formation Revealed by Cryo-TEM, Science (80-. ). 323 (2009) 1455–1458. https://doi.org/10.1126/science.1169434.

[242] A. Saha, J. Lee, S.M. Pancera, M.F. Bräeu, A. Kempter, A. Tripathi, A. Bose, New insights into the transformation of calcium sulfate hemihydrate to gypsum using time-resolved cryogenic transmission electron microscopy, Langmuir. 28 (2012) 11182–11187. https://doi.org/10.1021/la3024474.

[243] M. Mayer, W. Augustin, S. Scholl, Adhesion of single crystals on modified surfaces in crystallization fouling, J. Cryst. Growth. 361 (2012) 152–158. https://doi.org/10.1016/j.jcrysgro.2012.09.032.

[244] D. Erdemir, A.Y. Lee, A.S. Myerson, Nucleation of Crystals from Solution : Classical and Two-Step Models, Acc. Chem. Res. 42 (2009). https://doi.org/10.1021/ar800217x.

[245] E. Curcio, E. Fontananova, G. Di Profio, E. Drioli, Influence of the structural properties of poly(vinylidene fluoride) membranes on the heterogeneous nucleation rate of protein crystals, J. Phys. Chem. B. 110 (2006) 12438–12445. https://doi.org/10.1021/jp061531y.

[246] A. Razmjou, E. Arifin, G. Dong, J. Mansouri, V. Chen, Superhydrophobic modification of TiO2 nanocomposite PVDF membranes for applications in membrane distillation, J. Memb. Sci. 415–416 (2012) 850–863. https://doi.org/10.1016/j.memsci.2012.06.004.

[247] M. Zeyu, Y. Hong, M. Liyuan, M. Su, Superhydrophobic membranes with ordered arrays of nanospiked microchannels for water desalination, Langmuir. 25 (2009) 5446–5450. https://doi.org/10.1021/la900494u.

[248] Z. Xiao, Z. Li, H. Guo, Y. Liu, Y. Wang, H. Yin, X. Li, J. Song, L.D. Nghiem, T. He, Scaling mitigation in membrane distillation: From superhydrophobic to slippery, Desalination. 466 (2019) 36–43. https://doi.org/10.1016/j.desal.2019.05.006.

[249] H. Julian, Y. Ye, H. Li, V. Chen, Scaling mitigation in submerged vacuum membrane distillation and crystallization (VMDC) with periodic air-backwash, J. Memb. Sci. 547 (2018) 19–33. https://doi.org/10.1016/j.memsci.2017.10.035.

[250] T. Zou, X. Dong, G. Kang, M. Zhou, M. Li, Y. Cao, Fouling behavior and scaling mitigation strategy of CaSO4in submerged vacuum membrane distillation, Desalination. 425 (2018) 86–93. https://doi.org/10.1016/j.desal.2017.10.015.

[251] T. Tong, A.F. Wallace, S. Zhao, Z. Wang, Mineral scaling in membrane desalination: Mechanisms, mitigation strategies, and feasibility of scaling-resistant membranes, J. Memb. Sci. 579 (2019) 52–69. https://doi.org/10.1016/j.memsci.2019.02.049.

[252] M. Nosonovsky, B. Bhushan, Hierarchical roughness optimization for biomimetic superhydrophobic surfaces, Ultramicroscopy. 107 (2007) 969–979. https://doi.org/10.11964/jfc.20160410378.

[253] Y. Kwon, N. Patankar, J. Choi, J. Lee, Design of surface hierarchy for extreme hydrophobicity, Langmuir. 25 (2009) 6129–6136. https://doi.org/10.1021/la803249t.

[254] M. Gryta, Calcium sulphate scaling in membrane distillation process, Chem. Pap. 63 (2009) 146–151. https://doi.org/10.2478/s11696-008-0095-y.

[255] M. Uchymiak, E. Lyster, J. Glater, Y. Cohen, Kinetics of gypsum crystal growth on a reverse osmosis membrane, J. Memb. Sci. 314 (2008) 163–172. https://doi.org/10.1016/j.memsci.2008.01.041.

[256] W.Y. Shih, A. Rahardianto, R.W. Lee, Y. Cohen, Morphometric characterization of calcium sulfate dihydrate (gypsum) scale on reverse osmosis membranes, J. Memb. Sci. 252 (2005) 253–263. https://doi.org/10.1016/j.memsci.2004.12.023.

[257] A. Rahardianto, W.Y. Shih, R.W. Lee, Y. Cohen, Diagnostic characterization of gypsum scale formation and control in RO membrane desalination of brackish water, J. Memb. Sci. 279 (2006) 655–668. https://doi.org/10.1016/j.memsci.2005.12.059.

[258] C. He, Z. Liu, J. Wu, X. Pan, Z. Fang, J. Li, B.A. Bryan, Future global urban water scarcity and potential solutions, Nat. Commun. 2021 121. 12 (2021) 1–11.

https://doi.org/10.1038/s41467-021-25026-3.

[259] R.I. McDonald, K. Weber, J. Padowski, M. Flörke, C. Schneider, P.A. Green, T. Gleeson, S. Eckman, B. Lehner, D. Balk, T. Boucher, G. Grill, M. Montgomery, Water on an urban planet: Urbanization and the reach of urban water infrastructure, Glob. Environ. Chang. 27 (2014) 96–105. https://doi.org/10.1016/j.gloenvcha.2014.04.022.

[260] R.I. McDonald, P. Green, D. Balk, B.M. Fekete, C. Revenga, M. Todd, M. Montgomery, Urban growth, climate change, and freshwater availability, Proc. Natl Acad. Sci. USA. 108 (2011) 6312–6317. https://doi.org/10.1073/pnas.1011615108.

[261] Muhammad Yaqub, W. Lee, Zero-liquid discharge (ZLD) technology for resource recovery from wastewater: A review, Sci. Total Environ. 681 (2019) 551–563. https://doi.org/10.1016/J.SCITOTENV.2019.05.062.

[262] A. Ali, C.A. Quist-Jensen, E. Drioli, F. Macedonio, Evaluation of integrated microfiltration and membrane distillation/crystallization processes for produced water treatment, Desalination. 434 (2018) 161–168. https://doi.org/10.1016/j.desal.2017.11.035.

[263] R. Xiong, C. Wei, Current status and technology trends of zero liquid discharge at coal chemical industry in China, J. Water Process Eng. 19 (2017) 346–351. https://doi.org/10.1016/j.jwpe.2017.09.005.

[264] C. Boo, I.H. Billinge, X. Chen, K.M. Shah, N.Y. Yip, Zero Liquid Discharge of Ultrahigh-Salinity Brines with Temperature Swing Solvent Extraction, Environ. Sci. Technol. 54 (2020) 9124–9131. https://doi.org/10.1021/acs.est.0c02555.

[265] A.B. Pouyfaucon, L. García-Rodríguez, Solar thermal-powered desalination: A viable solution for a potential market, Desalination. 435 (2018) 60–69. https://doi.org/10.1016/j.desal.2017.12.025.

[266] M. Al-Sahali, H. Ettouney, Developments in thermal desalination processes: Design, energy, and costing aspects, Desalination. 214 (2007) 227–240. https://doi.org/10.1016/j.desal.2006.08.020.

[267] S.K. Patel, P.M. Biesheuvel, M. Elimelech, Energy Consumption of Brackish Water Desalination: Identifying the Sweet Spots for Electrodialysis and Reverse Osmosis, ACS ES&T Eng. 1 (2021) 851–864. https://doi.org/10.1021/ACSESTENGG.0C00192.

[268] S.K. Patel, M. Qin, W.S. Walker, M. Elimelech, Energy Efficiency of Electro-Driven Brackish Water Desalination: Electrodialysis Significantly Outperforms Membrane Capacitive Deionization, Environ. Sci. Technol. 54 (2020) 3663–3677. https://doi.org/10.1021/ACS.EST.9B07482/SUPPL_FILE/ES9B07482_SI_001.PDF.

[269] D.R. Lide, CRC Handbook of Chemistry and Physics, Boca Raton, FL, 2005. https://doi.org/10.1002/jctb.280500215.

[270] B. Sun, M. Zhang, S. Huang, J. Wang, X. Zhang, Limiting concentration during batch electrodialysis process for concentrating high salinity solutions: A theoretical and experimental study, Desalination. 498 (2021) 114793. https://doi.org/10.1016/j.desal.2020.114793.

[271] T. Rottiers, K. Ghyselbrecht, B. Meesschaert, B. Van Der Bruggen, L. Pinoy, Influence of the type of anion membrane on solvent flux and back diffusion in electrodialysis of concentrated NaCl solutions, (2014). https://doi.org/10.1016/j.ces.2014.04.008.

[272] L. Han, S. Galier, H. Roux-de Balmann, Ion hydration number and electro-osmosis during electrodialysis of mixed salt solution, Desalination. 373 (2015) 38–46. https://doi.org/10.1016/j.desal.2015.06.023.

[273] C. Jiang, Q. Wang, Y. Li, Y. Wang, T. Xu, Water electro-transport with hydrated cations in electrodialysis, Desalination. 365 (2015) 204–212. https://doi.org/10.1016/j.desal.2015.03.007.

[274] T. Sata, Studies on anion exchange membranes having permselectivity for specific anions in electrodialysis-effect of hydrophilicity of anion exchange membranes on permselectivity of anions, J. Memb. Sci. 167 (2000) 1–31.

[275] B. Sun, M. Zhang, S. Huang, W. Su, J. Zhou, X. Zhang, Performance evaluation on regeneration of high-salt solutions used in air conditioning systems by electrodialysis, J. Memb. Sci. 582 (2019) 224–235. https://doi.org/10.1016/j.memsci.2019.04.004.

[276] B. Tansel, J. Sager, T. Rector, J. Garland, R.F. Strayer, L. Levine, M. Roberts, M. Hummerick, J. Bauer, Significance of hydrated radius and hydration shells on ionic permeability during nanofiltration in dead end and cross flow modes, Sep. Purif. Technol. 51 (2006) 40–47. https://doi.org/10.1016/J.SEPPUR.2005.12.020.

[277] R. Heyrovská, Ionic Concentrations and Hydration Numbers of "Supporting Electrolytes," Electroanalysis. 18 (2006) 351–361. https://doi.org/10.1002/ELAN.200503416.